Part Performance Measurement, Analysis and Optimization for Binder Jetting Additive Manufacturing

by

Marc Wang

A thesis
presented to the University of Waterloo
in fulfillment of the
thesis requirement for the degree of
Master of Applied Science
in
Mechanical & Mechatronics Engineering

Waterloo, Ontario, Canada, 2020

Author's Declaration

I hereby declare that I am the sole author of this thesis. This is a true copy of the thesis, including any required final revisions, as accepted by my examiners.

I understand that my thesis may be made electronically available to the public.

Abstract

Binder Jetting (BJ) is an additive manufacturing (AM) process where objects are formed layer by layer. The manufacturing of parts is performed by depositing powder layer by layer and binding them together using a binding agent resulting in a green part. This is followed by thermal processing to fuse powder particles together.

Unfortunately, achieving full density through the thermal process is difficult due to the low initial density of the green part. Full density will result in substantial shrinkage. Consequentially, there is an incentive to maximize the density of the green part. Sadly, due to the presence of surface connected pores, measuring the density of green parts is not trivial. This work will propose a measurement methodology for measuring green density and processing computed tomography images obtained from green binder jetting parts. It was discovered that no standard was codified for the density measurement of such parts using either Archimedes or Micro-Tomography. Based on experimentally informed analysis, the use of the methodology ISO 5013 for measuring relative bulk density is recommended. Among the three methodologies evaluated (oil infiltration and wax coating), ISO 5013 was the method with the lowest average estimated measurement error (0.36%). In parallel, computed tomography datasets were analyzed, where multiple global threshold techniques were evaluated to extract bulk density metrics. Through experimentally informed analysis, the threshold method Otsu, Mean and Isodata were the most consistent at segmenting computed tomography image of green samples.

The second section of this thesis tackles heterogeneity issues found in previous work [1]. Wheat et al. attributed the heterogeneity to powder segregation. Unfortunately, due to the fragility of green BJAM parts, only computed tomography could observe the internal powder arrangement. Consequently, particle segmentation and detection software was developed, specifically tailored towards capturing the particle space for BJAM parts. Two approaches were tried: curvature-based watershed segmentation and Mask-RCNN. The micro-tomography images were knowingly degraded to achieve high data acquisition throughput. Unfortunately, this heavily degraded the performance of both Watershed and Mask-RCNN segmentation. Watershed segmentation displayed acceptable segmentation (70.7%) but poor detection performance (26.6%). Alternatively, Mask-RCNN scored similar segmentation performance (71.3%) with watershed but with twice the detection (48.1%). Regrettably, current performance of Mask-RCNN are inadequate for use in detecting particle segregation.

The last section proposes the use of multi-objective Bayesian optimization algorithm for optimizing the process parameters for BJAM. The proposed algorithm managed to

minimize porosity (37.5%), while keeping print time low (87 min). Unfortunately, dimensional fidelity were still low (Δ 2.33 x 1.86 x 1.95 mm). The method has the potential of reducing the number of empirical trials to perform optimization, while still achieving Pareto optimality for AM. Future work will be done in improving th e efficiency of this method and robustness against noise.

Acknowledgements

I would like to thank my supervisor Professor Vlasea for her support and help during these two years. I could not have gotten a better supervisor. In addition, I would like to thank my colleagues Issa Rishmawi, Alex Groen, Roman Boychuk and Henry Ma for their help in my experiments. Without you guys, this thesis would have been a lot harder. Furthermore, I would like to thank my colleagues in the Multi-Scale Additive Manufacturing (MSAM) Lab for hosting me in this lab and making the daily work life interesting.

Dedication

This thesis is dedicated to my parents. Thank you for supporting me throughout my life.

Table of Contents

List of Figures

List of Tables

Chapter 1

Introduction

Additive manufacturing (AM) is a manufacturing process where objects are formed by depositing material layer by layer. This is in opposition to subtracting manufacturing, where material is removed. According to Gibson et al. the different types of process available are as follows [16]:

1. Laser Powder Bed Fusion
2. Material Extrusion
3. Directed Energy Deposition
4. Material Jetting
5. Binder Jetting
6. Sheet Lamination
7. Vat Photopolymerization
8. Direct Write technologies

BJAM builds the object layer by layer by depositing binder selectively on a bed of powder. An example of the process is shown in Figure 1.1. Among the different classes of metal 3D printing process, binder jetting has the lowest operating costs [17]. Wohlers et al. surveyed 127 companies representing 1751 machines [18]. BJAM printers represented 13.5% of the machine installed in those companies. Also, when asked the most likely machine

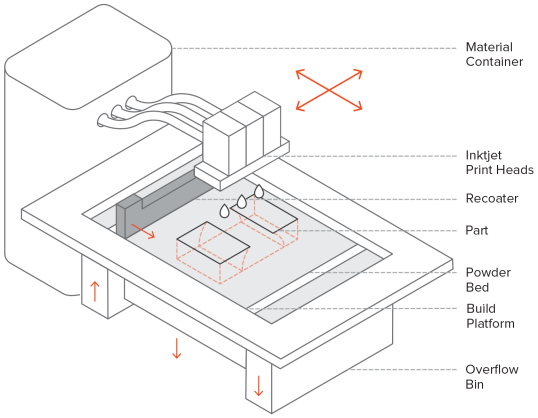

Figure 1.1: Diagram of the binder jetting printing process [4]

they would purchase next. 30% of them responded interest in buying a binder jetting platform (HP Multi Jet Fusion) [18]. Consequently, market share and popularity of BJAM will only be increasing in the future.

For metals or ceramics, BJAM is done in two stages. The first stage is the printing, where the rough 3D geometry is formed. The initial object is called a "green part". Green parts are too weak for industrial use. Consequently, the second stage is sintering, where the object is strengthened and densified via heat treatments. Further post-processing can be applied to enhance part geometric and/or structural properties. Without post-processing, BJAM has several drawbacks such as lower part strength, lower achievable density of the final parts, lower geometric fidelity, and lower surface quality compared to other AM process [19]. Despite these drawbacks, binder jetting has found a niche in applications where the listed flaws are trivial or actively sought after. This is the case for sand casting [20], prototyping, ceramic implants [12] or drug delivery [21]. In ceramic implants and drug delivery, the parts need to have a certain amount of porosity. While in sand casting, having a large build volume at low cost is more important than high density and mechanical strength.

Still, the research community is actively working on resolving the flaws of BJAM. Furthermore, various approaches are investigated such as controlling, optimizing the print process and post-processing.

1.1 Motivation

This thesis will focus on binder jetting additive manufacturing (BJAM). Specifically, on the measurement and analysis of the pores and particle space in green parts with regards to process parameters and part quality outcomes. Currently, metrology for BJAM is sparsely covered in literature. Furthermore, process parameter optimization in BJAM is still an open problem due to the large number of parameters.

As mentioned earlier, BJAM is a multi-step manufacturing process. Unfortunately, the initial density of the green part is typically low [22]. Therefore to achieve full density through sintering, shrinkage will be substantial. Consequentially, maximizing the green density to reduce shrinkage is of interest. Since green parts are loosely packed powder, this makes volume measurement non-trivial which correspondingly complicates density measurement. Additionally, green parts are highly fragile, water soluble and highly porous. No standards exist in literature for measuring density of green parts. Hence, a plethora of methodologies have been used in literature for measuring density of green parts (Table 3.1). Therefore, a standardized methodology needs to be established. The first section of this work aims at proposing a methodology form measuring the density of green parts.

The second part of this thesis will focus on developing tools to better quantify heterogeneity observed by Wheat et al. in BJAM parts [1]. The heterogeneity was linked to particle segregation. The segregation was observed on a layer-by-layer basis. Therefore, only the non-destructive method such as μCT can observe it. Consequentially, software to segment and detect powder segregation is required.

Thirdly, this thesis will demonstrate a methodology used to build an empirical model aimed at optimizing relative density, dimensional accuracy and minimize printing time of green parts. In terms of binder jetting process optimization, academic and industry efforts focus on controlling process parameters empirically [22]. The holy grail for the AM industry is to have an accurate simulation of the printing process, as demonstrated by academic efforts and the manufacturing industry push towards digital workflows [23]. Unfortunately, for BJAM, this is a multi-physics simulation problem and thereby extremely difficult. For this reason, optimization of the process is done through experimentation or experimentally informed models [22]. Furthermore, to the best of the author's knowledge, process optimization work in BJAM is typically done for one quality metric at a time. Also, process parameter optimization is done on a small subset of parameters. Therefore for optimization over the full range of parameters, a Bayesian multi-objective optimization methodology will be showcased.

1.2 Objectives

The research objectives are as follows.

1. Propose a measurement methodology for measuring green part density.
2. Develop a software to detect particle segregation from CT images.
3. Propose a methodology for multi-objective optimization of process parameters.

1.3 Thesis Structure

The objectives of the research and chapters are presented in the following order:

1. A brief overview of the BJAM process and process parameters: The focus is to present a glance into the complex nature of the BJAM process, with the background presented in Chapter 2.
2. Methodologies for measurement of green part density: Various density measurement techniques are reviewed in detail and tested experimentally to determine their suitability for such use case. This work is captured in Chapter 3.
3. Algorithms for particle detection and particle space characterization: Create a fast and low cost tools to detect particle and pore space properties. This work is captured in Chapter 4.
4. Multi-objective Bayesian process optimization of SS316L: An empirical model is fitted for SS316L. The model is tested to determine its applicability towards finding the optimal BJAM process parameters. Multiple quality metrics are optimized simultaneously. This work is captured in Chapter 5.
5. Conclusion and future work : The research contributions in this thesis are summarized. Additionally, possible improvement and future work are listed.

Chapter 2

Background and Literature Review of Binder Jetting

2.1 Principle of Operation

Previously known as Three-dimensional Printing Technique (3DP), binder jetting additive manufacturing (BJAM) was first patented at the Massachusetts Institute of Technology (MIT) [24]. As expressed previously, binder jetting is an AM technique where a liquid known as a binder is deposited over each layer of the powder feedstock material. The binder glues the feedstock material together; this is what holds the geometry in the green part state. The typical feedstock material for BJAM is powder, but the use of slurry have been recorded in literature [25].

Usually, the feedstock material is stored in a feed bed platform. Material is deposited on the build platform via powder spreader in the form of a roller or a blade. The material can also be stored in a hopper, where it is directly deposited (or dosed) over the build bed and subsequently compacted or leveled using a roller or a blade mechanism respectively. The binder deposition system uses the same technology as an inkjet printer. The binder can either be aqueous- or organic- based. What drives binder selection is its chemically compatibility with the deposition system and feedstock material.

In the cases of metals or ceramics, the part, when removed from the machine is too fragile to be useful. The mechanical strength of the object is limited by the adhesive strength of the binder. At this step, the object is said to be in a "green" state. The green part needs to be sintered inside an oven to further solidify it.

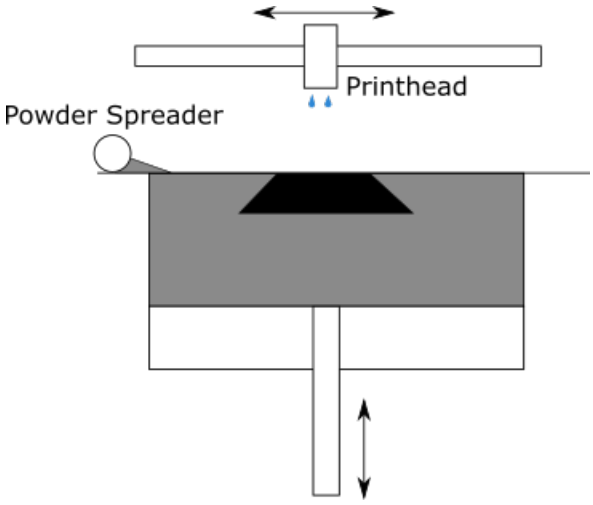

Figure 2.1: Binder Jetting principle of operation

2.2 Advantages and Drawbacks of the Technology

The main advantage of binder jetting is its relative low cost compared to energy-based systems such as Laser Powder Bed Fusion and Directed Energy Deposition [17, 18]. The lack of high temperature requirements during the AM process reduces the complexity, acquisition and operating cost of the printer. Also, energy-based systems create a thermal gradient inside the part which, if not managed properly, can warp or create cracks in the object. For binder jetting, the lack of temperature induced warping and the use of a powder bed eliminates the need for support structures during printing. Furthermore, operation at room temperature makes the process scalable. This can be seen based on the systems available on the market, as they have some of the largest build envelopes compared to other AM machines available for other types of powder bed fusion processes (Table. 2.2). Also, BJAM can accommodate a wide variety of material. The only requirement is the binder ability to glue the powder together.

Unfortunately, a significant drawback of the technology is the difficulty in achieving high density. Typically, green parts have a density of around 50% due to inherent limitations in powder packing [22]. Full densification needs to be achieved through sintering. Densities after sintering , varying between 60% - 95%, have been reported in literature [26, 27, 28, 29, 30]. Densification can be further enhanced through the use of Hot Isostatic Pressing (HIP) with near 100% density being reported [31]. Due to the initial low density of green parts, shrinkage during sintering is substantial. This adds a layer of complexity as this

shrinkage needs to be taken into account when printing parts. Shrinkage can also create cracks and other defects. Small features may also be erased by the heat treatment [32], which limits the overall resolution of the process. Moreover, high surface roughness is also a major drawback of BJAM [33, 19].

2.3 Process Parameters in Binder Jetting

Numerous papers have attempted to model the effect of various process parameters on part quality metrics. Listed in Table 2.1 below are various findings on the main process parameter contributors towards influencing various part quality metrics.

Table 2.1: List of process parameters and their known effects on part qualities in literature. A more comprehensive list can be found in the work by Du et al., Lv et al. for ceramics and Li et al. for metals [11, 13, 12]

Process Parameter	Part Quality Metrics Influenced
Layer Thickness	surface roughness [34], density [35], dimensional accuracy [34]
Feed Powder Ratio	mechanical strength [36]
Powder Spread Speed	density [37], surface roughness [37]
Binder saturation	mechanical strength [36], surface roughness [38], dimensional accuracy [38]
Drying time	dimensional accuracy [34]
Powder size distribution	density [39, 30]

Chen and Zhao using Taguchi method found layer thickness to be the biggest contributor to surface roughness. Increasing layer thickness create a step effect on curved surface which increases surface roughness and by extension worsen dimensional accuracy as well [34]. For dimensional accuracy, the main driver for vertical accuracy is the drying time with short and long drying time leading to high shrinkage [34]. As for width accuracy, the main contributor are evenly split between drying time, heater power and layer thickness. In the work by Rishmawi et al., only the layer thickness and roller rotation was varied. low layer thickness promotes higher density. In addition, the roller helps compaction of the powder. Shrestha and Manogharan, using taguchi optimization as well, determined that increasing saturation and powder feed ratio(powder needed over powder deposited) helps with improving mechanical strength. This is corroborated by Vaezi and Chua where

mechanical strength was improved through increasing saturation while keeping all other parameter constant [38]. On the other hand, increasing saturation worsens dimensional accuracy. This is was observed by Jim, Miyanaji et al. where too much binder relative to powder would result in the binder liquid leaking out of the desired area. In the simulation side, Haeri et al. used discrete element simulation to model the powder spreading process. Increasing powder spread speed increases surface roughness and decreases powder compaction. In addition, according to their model, using a roller instead of a blade to spread powder increases powder compaction. In two work by the same author, using Bimodal powder size distribution helps with powder packing and flowability. Multi-modal size distribution positive effect on packing packing was known for a long time in the field of particulate solid [42, 43]. An in depth review of the various consideration for process optimization in green sample can be found in the paper by Miyanaji et al.. The author mentions the tight coupling between the various process parameters. For example, increasing layer thickness requires an increase in saturation.

All experiments in this thesis are conducted on an M-Flex BJAM system (ExOne, PA, US). The parameters that can be varied on this type of system are general for most BJAM systems, and as such, the findings revealed in this thesis can be generalized beyond the present scope. As an overview, the process parameters of interest are:

- Layer Thickness: Material Deposition thickness (μm)
- Oscillator Rotation: Rotation speed of the Oscillator (rpm)
- Recoat Speed: Powder deposition linear speed (mm/s)
- Roller Speed: Roller linear movement speed (mm/s)
- Roller Rotational Speed: (rpm)
- Drying Speed: Heater linear movement speed (mm/s)
- Drying Power: Heater initial power output (%)
- Saturation: Percentage of binder in powder (%)
- Binder Set Time: Rest time between layers (s)
- Target Temperature: If auto temperature enabled; printers will vary heater to reach target temperature ($^{\circ}C$)

The one parameters that is more proprietary in terms of ExOne system definition is the binder saturation and power. To provide more insights on how to generalize this setting, the binder saturation is calculated as follows:

$$S = \frac{V_{binder}}{V_{pores}} \tag{2.1}$$

In practice, only the binder volume is directly controlled by the machine. Therefore, proper binder volume is computed as :

$$V_{binder} = S * V_{pores} \tag{2.2}$$

Where V_{pores} can be calculated as follows :

$$V_{pores} = (1 - PR) * V_{solid} \tag{2.3}$$

V_{solid} is the volume of the whole object and PR is the packing rate of the powder. Packing rate inside the Exone machine is assumed to be 0.6.

2.4 Area of Application of Technology

Historically as shown in the table 2.2, commercial binder jetting printers were geared towards prototyping and sand cores manufacturing for metal casting. Owing to its low operating cost, high production rate and large build envelope, binder jetting has found a niche in the sand casting industry. Using binder jetting to manufacture sand cores has been shown to reduce lead time and enable higher design complexity for the design of molds [20]. Consequentially, Almaghariz et al. has shown the use of binder jetting is advantageous for low-volume direct metal part production for low geometric complexity object. For parts with highly complex geometries, BJAM is advantageous even for high volume production requirements.

Table 2.2: Representative 3DP printers released by all companies included in [14] and [15], ordered by company inception date or first 3DP machine release and product release date. Current full color range machines are referred to as full CMYK machines

Company name	Product name	Release year	Resolution, material, and/or other spec.	Application

Z Corporation	Z402	1996	Starch-plaster powder, water-based binder	Prototyping
	Z402C	2000	First multicolor printer	Prototyping
	Z810	2001		Prototyping
	Spectrum Z510	2005	18.36 dm^3 build volume	Prototyping
	Spectrum Z310 Plus	2005	Plaster powder	Prototyping
	ZPrinter 450	2007	full cymk, plaster powder	Prototyping
	ZPrinter 350	2009		Prototyping
	ZPrinter 250	2010	Full CMYK	Prototyping
3D system	ProJet CJP 860 Pro	2013	Full CMYK. 44.32 dm^3 build volume	Prototyping
	Projet 160	2013	monochrome, composites, Gypsum. 5.55 dm^3 build volume	Prototyping
	Projet 4500	2013	Polymer. 10.48 dm^3 build volume	Prototyping
Extrude Home AM	ProMetal RTS-300	1999	Metal	Prototyping
ExOne	S-Max	2010	1.26 m^3 build volume	Ceramics
	Innovent	2013	Metals, ceramics and composites, 0.676 dm^3 build volume	Prototyping
	Exerial	2015	Silicate, Zircon, Chromite, 1.848 m^3 build volume	Sand cores
Microjet Technology Co., Ltd.	T10	2010		Prototyping
Generis GmbH	GS1500	2001		Sand cores
VoxelJet	VX800	2005		Sand cores
	VS800 HP	2009		Sand cores
	VXC800	2012		Sand cores
	VX2000	2013	PMMA, Silicate	Sand cores
	VS4000	2016	PMMA, Silicate, 8 m^3 build volume	Sand cores
	VX2000	2017	PMMA, Silicate	Sand cores
addwii	X1	2015	full CMYK using Composites, Gypsum, 200x160x150 build volume	Production
Digital Metal	DM P 2500	2017	print volume of 2500 cm^3	Prototyping
Desktop Metal	DM Studio	2017	Metal deposition technology	Prototyping
	DM Production	2017	Microwave-assistted furnace for sintering	Prototyping, Production
HP	HP Multi Jet Fusion 4200	2016	full CMYK	Prototyping, Production
GE Additive	Project H1	2016	Metal, 31.5 dm^3 build volume	Production

Tongtai Machine & Tool Co.	AMS-1200	2018	0.5184 m^3 build volume	Sand cores

Through the use of ink-jet printhead, binder jetting lends itself well for printing multicolor parts. As shown in the table 2.2, multicolor printers were among the first printers commercialized. The capability of printing multi-color parts makes binder jetting ideal for prototyping purpose. Currently, a large part of the literature is focused on metal [22]. However, for widespread industry adoption in this domain, issues with process variation resulting in porous and geometric fidelity defects still need to be tackled [22]. Due to the high melting temperature of ceramics, binder jetting is a popular choice for ceramics part production as well [11]. In addition, binder jetting has also found some niche application in making drug delivery systems [21] and food products [46]. With the growing popularity of binder etting, application areas of application will continuously expand [18].

For the objective to be tackled in this thesis, a more comprehensive literature review will be offered in each chapter.

Chapter 3

Methodologies for Bulk Density Estimation for Binder Jetting

3.1 Background

In Binder Jetting additive manufacturing (BJAM) of metals, green parts need to be densified in an oven. If the initial density is low, this process will result in substantial shrinkage of the part [22]. Therefore, it is of interest to maximize green density. The low density and the presence of surface connected pores in green binder jetting parts make volume measurement difficult. By extension, this complicates density measurement. To the best of the authors knowledge, the determination of bulk density for green binder jetting parts is not standardized in BJAM literature, nor in industry. For porous solids, experimental methods do not address the measurement of the absolute density value, rather relative density is measured using various methodologies [47], with each method having its own bias. Given the lack of universal porous benchmark artifacts, the bias of each measurement method is seldom quantified. Therefore, for density values listed in BJAM literature to be comparable, a single methodology needs to be agreed upon, as the density measurements are performed as part of manufacturing quality assurance and process optimization. In this work, relative density estimations and computed tomography estimations were deployed and compared. The three relative density methods evaluated in this chapter were identified based on their previous use in porous media and Binder Jetting (Table 3.1), ease of use, and high measurement throughput. The relative density methods evaluated are Archimedes with Isopropanol immersion (ISO 5017), water immersion with oil coating (ASTM B962), and wax coating (ASTM D7263). Gage repeatability and reproducibility

study (Gage R&R Study) will be conducted using a Bayesian inference approach. Lastly, the density will be estimated using computed tomography by deploying various thresholding techniques.

3.2 Archimedes Methods for Density Measurement

The three selected measurement methods all use the Archimedes principle to measure density. The Archimedes principle states that a submerged object will experience a buoyancy force equal to the weight of the fluid or wetting agent that it displaces. Therefore, weight measured under water will have a lower apparent weight than if measured in air. This relationship can be expressed as:

$$m_{\text{Dry}} - m_{\text{Submerged}} = m_{\text{FluidDisplaced}} \tag{3.1}$$

Given a known density for the fluid, one can calculate the volume of the liquid displaced. If there are no trapped air bubbles on the surface of the part or within the object, the volume of the displaced liquid will correspond to the volume of the object. Therefore, the density of the object can be calculated precisely. Unfortunately, the presence of surface connected pores will reduce the measured volume displacement. The resulting estimated value of density will be higher than the actual density of the porous material. Each of the evaluated standards, as discussed below, attempts to solve this issue differently, either through sealing the porous object, or by subtracting the liquid mass present inside the part. Once the density of the object is established, the value of interest in this chapter is the relative density and porosity.

$$\rho_{\text{rel}} = \frac{\rho_{\text{part}}}{\rho_{\text{full}}} * 100 \tag{3.2}$$

$$\text{Porosity} = 1 - \rho_{\text{rel}} \tag{3.3}$$

ρ_{part} is the density of the object measured and ρ_{full} is the density of object if no pores are present. Porosity is the percentage of pores present in the object.

For powder bed fusion additive manufacturing, the ASTM standard F3302[1] recommends the use of the test method ASTM B311[2]. ASTM B311 comes from the field of

[1] ASTM FF3302: Standard for Additive Manufacturing Finished Part Properties Standard Specification for Titanium Alloys via Powder Bed Fusion[48]

[2] ASTM B311: Standard Test Method for Density of Powder Metallurgy (PM) Materials Containing Less Than Two Percent Porosity[49]

Powder Metallurgy. Unfortunately, test method B311 is only appropriate for objects with porosity less than 2%. Typically, Green Binder Jetting parts have porosity that hovers in the 50%. Also, B311 specifies using water as the wetting agent which will dissolve aqueous binders which compromises the integrity of the green part. In the ASTM powder metallurgy standard portfolio, ASTM B962 is the counterpart to ASTM B311 for high porosity object. Therefore, ASTM B962 is the standard used for green parts measurement. The table 3.1 is a non-exhaustive list of binder jetting papers and density measurement method they deploy. It illustrates the range of methods used by researchers to approximate relative density or porosity in BJAM parts.

Table 3.1: Measurement method used in binder jetting literature

Method	Description	Citation in AM
ASTM B962-17	Standard Test Methods for Density of Compacted or Sintered Powder Metallurgy (PM) Products Using Archimedes's Principle	[50, 31, 51, 29, 52, 53, 54]
ASTM C373-18	Standard Test Methods for Determination of Water Absorption and Associated Properties by Vacuum Method for Pressed Ceramic Tiles and Glass Tiles and Boil Method for Extruded Ceramic Tiles and Non-tile Fired Ceramic	[55, 56, 57, 58, 59, 60]
Geometric Density	Caliper density	[61, 62, 59]
Mercury Porosimetry	Pore size and porosity measurement using capillary flow	[63, 64, 65]
Pycnometry	Density measurement using gas displacement	[66]

In literature, the standard ASTM B962 [67] is commonly used to estimate the bulk relative density for green binder jetting parts. ASTM B962 is also as Powder Metallurgy Standard. Materials measured include alumina $(50-65\%)$ [50], porcelain $(89-93\%)$ [52], copper $(55-99\%)$ [31, 29], barium titanate $(22-27\%)$ [53] and Cordierite $(42-92\%)$ [51]. For green samples, ASTM B962 standards rely on infiltrating the porous object with oil to

seal the pores. The repeatability and reproducibility interval are not quantified for green samples. The standard mention quantification of repeatability and reproducibility is to be completed within 5 years. For ferrous and copper-based sintered parts, on the other hand, the repeatability interval is $0.05\,\mathrm{g/cm^3}$ and the reproducibility interval is $0.06\,\mathrm{g/cm^3}$ at a 95% confidence interval [67]. Given SS316L has a density of $8\,\mathrm{g/cm^3}$ [68], the accuracy and repeatability of the standard is $\pm 0.625\%$ and $\pm 0.75\%$ respectively. Since no porous reference material exists, the bias of the measurement is not stated [67]. Since powder metallurgy and binder jetting are two intrinsically linked fields. It is natural that ASTM B962 is widely used in binder jetting. However, this standard might be unsuitable for measuring density of green binder jetting parts. From initial trial, the use of oil for sealing the sample is problematic. ASTM B962 recommends the use of a low-viscosity oil. When the sample is submerged, the oil only protects the sample for a short amount of time. Furthermore, the oil can leak out when handling the samples. The measured relative density of SS316L powder metallurgy is typically in the 80% [69]. Additionally, the typical use of ASTM B962 is for powder metallurgy bearings which are stored in oil [67]. This might explain the choice of oil impregnation.

For ceramic materials in specific, ASTM C373 [70] is also another standard that has previously been employed in binder jetting [55, 56, 57]. In prior research [55, 56], the water was substituted for ethanol since a water-soluble polymer was used as the binding agent in the binder jetting process. Vlasea et al. recorded density varying between $51 - 57\%$ with a variation of $\pm 1\%$ [55]. Sheydaeian et al. recorded the density of $39 \pm 1\%$ as well [56]. Furthermore, Castilho et al. sintered the parts and recorded a density of $38.2 \pm 0.6\%$ to $56.9 \pm 1.39\%$ [57]. The previous authors studied Calcium Polyphosphate. Unfortunately, repeatability and reproducibility is not stated for density measurement. Similar to the ASTM B962 standard, the bias is not measured. ISO 5017 is evaluated in this study instead ASTM C373. ASTM C373 requires water as the immersion liquid as opposed to ISO 5017. This flexibility means ISO 5017 does not carry any statement on the repeatability and reproducibility. Additionally, Pinot evaluated ISO 5017 for measuring porosity of limestone [71]. The author estimated a gage uncertainty (repeatability + reproducibility) of 0.1% for samples with large pores and 0.5% for samples with small pores.

Another alternative for estimating the density of porous structures is to coat the surface with wax such as specified in ASTM D7263 [72]. This standard applies to the measurement of density for soil specimens. Due to the loose cohesion of soil, it can be argued that measuring bulk density of soil and green binder jetting samples present the same challenges. Both soil and green BJAM samples have surface connected pores as well. Furthermore, both have constituents which can be dissolved by water or other immersion fluid, thus reducing the integrity of the respective samples. To this effect, ASTM D7263 [72] suggests

a methodology to protect the sample structural integrity by sealing it with wax. Sealing the sample also removes the effect of surface connected pores. Unfortunately, unlike other ASTM standards, no statement is made on the precision and bias. This standard is not explicitly used in AM but similar methodology has been found in such works [73, 74]. In the work by Kamath et al. [73], they coated SS316L manufactured parts with wax to seal the outer pores. They measured porosity varying from $0.78\% - 2.22\%$ using an Archimedes setup. Additionally, porosity was also measured using a Scanning Electron Beam Microscope (SEM). For the SEM instrument, the samples were sliced into micrograph cross-sections. The authors found that the SEM estimated lower porosity values than Archimedes. This could be attributed to heterogeneity in the sample, and as such, the data captured by micrographs may not be representative of the pore space. Liang et al. measured the porosity of Ti6Al4V lattice structures manufactured using laser powder bed fusion. Porosity varying from 70% to 90% were measured. Furthermore, Spierings et al. examined different density measurements for density measurement (Archimedes, micrograph of a cross-section, X-ray CT) of SS316L selective melting parts [75]. If the part has visible cavities, they recommend coating the sample with a lacquer of known density. Incidentally, the accuracy of $\pm 0.08\%$ and the repeatability of $\pm < 0.1\%$ was calculated. Those values are lower than ASTM B962. Also, Spierings et al. suggests keeping the density of the immersion fluid below 1/5 the density of the measured object to keep errors low [75].

A disadvantage of both ASTM D7263 and ISO 5017 is they both require sample dimensions to have a side length of at least 30 mm or a volume of at least $50\,\mathrm{cm}^3$. This is impractical for additive manufacturing, where both the costs for the feedstock material and printer build envelope needed to achieve such dimension are high. Therefore, the sample dimension measured in this study does not comply with the minimum size requirement of ISO 5017 and ASTM D7263.

A brute-force approach to density estimation is to use so-called geometrical density. This is estimated by simply measuring the volume and weight of the part. An example of this is shown in the works by Jimenez et al., Winkel et al., Suwanprateeb et al. [61, 62, 59]. The so-called geometrical approach of measuring the sample volume via calipers is challenging, as the surface of green binder jetting parts generally has a high surface roughness. High surface roughness can lead to underestimating the object density by over estimating the object dimensions. Also, it is difficult to measure objects with irregular features using a caliper. Therefore, this approach is not evaluated in this work.

Porosimetry is a measurement method where mercury or another liquid is driven inside the part at high pressure. The governing equation of porosimetry is the Washburn equation

[76]:

$$D_P = -\frac{4\gamma \cos\theta}{P_L - P_G} \tag{3.4}$$

D_P = pore diameter
γ = surface tension
θ = contact angle
P_L = pressure of liquid
P_G = pressure of gas

Since the experiment is done in a vacuum, P_G is typically zero. As the pressure (P_L) of the liquid increases, it will penetrate pores of diameter D_p. By measuring the quantity of liquid being driven into the porous material at each pressure increase, it is possible to measure pore size distribution in addition to overall porosity. Porosimetry can be performed by measuring the pressure variation while withdrawing the liquid as well. Another porosity measurement is gas pycnometry. Gas pycnometer is a non-destructive measurement device. The system uses gas displacement to determine the volume a sample against a known volume(V_r). The governing equation is as follows [77]:

$$V_s = V_c + \frac{V_r}{1 + \frac{P_1}{P_2}} \tag{3.5}$$

V_s = Volume sample
V_c = Volume measurement cell
V_r = Volume of reference chamber
P_1 = Pressure sample chamber only
P_2 = Pressure sample chamber with reference chamber

Therefore, using the weight of the sample, it is possible to calculate the density of the object using V_s. In AM, gas pycnometer is mostly used to measure the density of powder [78]. In the paper by Aroom et al. [79], due to the perceived inability of commercial pycnometer to accommodate 3D printed medical devices, they constructed a pycnometer to measure surface connected porosity. The device is likely still in the development phase as they did not make a statement on the accuracy of the machine. Porosimetry only measures open porosity. Pycnometry, on the other hand, only measures closed porosity. Therefore both require other measurements to compute overall porosity. In pycnometry,

it is possible to measure overall porosity by coating the sample in wax as shown in the paper by Chang [77]. Although both porosimetry and gas pycnometry were tried in this study. The measurements were unstable. Therefore, neither porosimetry nor pycnometry were formally evaluated in this chapter.

3.3 Computed Tomography Methods for Density Estimations

For green BJ-AM samples, except ASTM D7263 [72] which protects the sample under a coat of wax, the Archimedes methodologies mentioned previously are all destructive testing. For green parts, the object is unusable after immersion. For non-destructive testing (NDT), the following methods are available for bulk density measurements: μCT and gas pycnometery. The challenges with pycnometry for BJAM have been addressed above. μCT is extremely sought after in the realm of manufacturing for metrology purposes [80, 81], as it can resolve spatial variation of the pore space. Obaton et al. investigated different NDT techniques to characterize porosity (Archimedes, pycnometer, Multi-Frequency Eddy Current and C-Scan Ultrasound). The authors were searching for a faster alternative to μCT. They found Archimedes to be accurate but time consuming. The pycnometer was faster but had higher uncertainty on the measurement. On the other hand, Multi-frequency eddy current method was limited in the size of the sample. Additionally, C-Scan ultrasound was fast and convenient but not suitable for complex geometry parts. μCT works by exposing a material to a radiation source and measure the attenuation of the radiation beam. Lab scale μCT systems typically comes in two configurations: Cone Beam or Parallel Beam (fig 3.1) configurations. For an in-depth review of μCT in AM, the author refers the reader to a comprehensive review by Thompson et al. [83].

Each pixel in an image obtained from a μCT is effectively the X-ray beam Attenuation as captured by a detector. X-ray attenuation is described by the following equation 3.6:

$$I = I_0 e^{-\int \mu(s) ds} \tag{3.6}$$

I_0 is the incident beam and $\mu(s)$ is the local linear attenuation along path s. From Equation 3.6, we can compute the attenuation as per Equation 3.7:

$$\int \mu(s) ds = -ln \frac{I}{I_0} \tag{3.7}$$

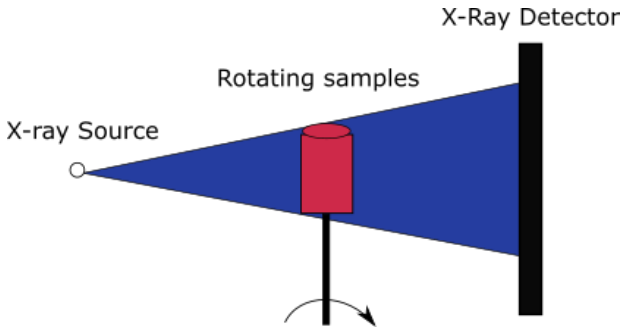

(a) Cone Beam

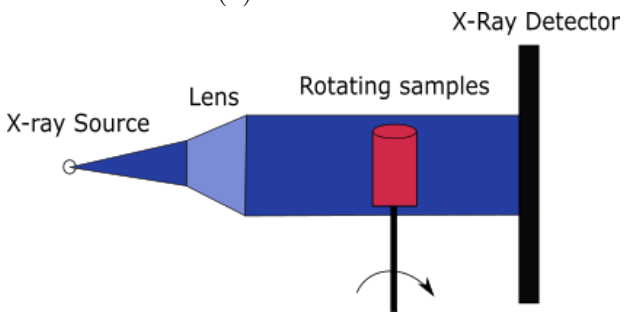

(b) Parallel Beam

Figure 3.1: Typical Computed Tomography (μCT) System Configurations

To capture a single 3D dataset, the scanner typically rotates the object in the field of view and collects a set of 2D image projections. From there, the set of 2D images are combined through the use of Tomographic Reconstruction Algorithms. The data acquisition is described by the Radon transform [84]. The Radon transform roughly states that given an unknown function $f(x, y)$, the radon function is the projection of f onto an X-ray detector as it rotates around the sample (θ). This process is reversible, given an infinite amount of rotational position θ and a detector with infinitely high resolution. Therefore, all CT reconstruction algorithms attempt to work around the constraint of noise, limited resolution and scanning time. The de facto standard for CT reconstruction approach is the Filtered Backward Projection (FBP) algorithm due to its low computation cost [85]. With the increase in computing power, iterative reconstruction methods are becoming more common as they offer better robustness against noise and shorter acquisition time [85].

3.3.1 Computed Tomography Data Acquisition, Segmentation, Calibration, and Thresholding

As stated in the works of Thompson et al. [83], De Chiffre et al. [80] and Leach et al. [86], the main barrier to the widespread adoption of computed tomography is the lack standardization for the acquisition and treatment of CT images. This lack of standards introduces uncertainty on the measurement acquired through computed tomography. To remedy this, several researchers are investigating μCT compared to traditional method for density determination [87, 88, 89, 82]. Although in all cases μCT is slower and more expensive than other methods, it has the advantage of capturing geometric information besides bulk density [86]. In the work by du Plessis et al. [87], the author proposes a standard method for density determination. For Ti6Al4V 10 mm cubes manufactured using Selective Laser Melting, they estimate the error to be $0.02\,\mathrm{g/cm^3}$ using μCT. Unfortunately, the use of proprietary software hampers the replication of their results.

As stated previously, the main advantage of μCT is the possibility to capture of geometrical information. Unfortunately, for the geometric information to be accurate, for green samples with a high geometric complexity, the part needs to be scanned at high resolution to resolve the pores. Furthermore, the multitude choice of threshold, segmentation algorithms and values can bias the CT scan data. The second part of this chapter will investigate the different CT-scan processing method and its effect on the various metrics that can be calculated from CT scan data.

3.3.2 Threshold Techniques

As the μCT scanner measures X-ray attenuation, a transformation needs to be done to map this value to a real density. The X-ray attenuation and density value correspondence can be found tabulated for some materials. If not available, a heuristic method is needed. One technique is to use threshold algorithms. These algorithms will segregate the pixels into different classes based on the pixel intensity value. This is assuming the materials inside the parts have distinct X-ray attenuation values. Since the BJ-AM components typically examined are manufactured using a single material (if the polymer binder content is assumed to be minimal), the algorithm will split the image into two regions, typically using a global value. Additionally, Iassonov et al. [90] analyzed 14 different thresholding techniques which included both global and local threshold algorithms. Among the global threshold, only Otsu and Isodata gave adequate results. The best results were obtained using Markov Random Field [91] and Indicator Krieging [92]. Unfortunately using local threshold algorithms, besides being computationally expensive, requires careful parameter

tuning to achieve good results. Those algorithms were not tried in this study as they are very slow. Additionally, they do not make a large impact (1-2% difference) when it comes to density determination [93]. The evaluated thresholds were selected due to their availability in image processing packages. Their definition are listed below and will be evaluated in the present study.

Isodata Thresholding Approach [94]

Isodata is an iterative thresholding technique where an initial threshold (t) value is chosen that satisfies the following requirement:

$$t_{i+1} = \frac{l(t_i) + h(t_i)}{2} \tag{3.8}$$

Where l is the mean pixel value for all pixels $< t$ and h is the mean pixel value for all pixels $> t$. The algorithm runs until the threshold converges towards a single value.

Li Thresholding Approach[95]

Li is an iterative thresholding technique that attempts at minimizing cross-entropy. Given an initial threshold guess and a tolerance value, a threshold value is computed:

$$t_{i+1} = \frac{l(t_i) - h(t_i)}{log(l(t_i)) - log(h(t_i))} \tag{3.9}$$

Where l and h have the same definition as in the Isodata algorithm. This process is repeated until the threshold converges to a single value within a certain pre-defined tolerance.

Mean Thresholding Approach [96]

This simply use the mean pixel value as the threshold. Using the mean is sensitive to outliers which can skew separation of the void or solid.

Minimum Thresholding Approach [96]

The minimum thresholding approach is an iterative algorithm that smooths the intensity histogram using a uniform filter until two peaks are generated. Then, the threshold is chosen as the minimum point along the histogram between the two local peaks.

Otsu Thresholding Approach [97]

One of the more popular thresholding techniques is the Otsu approach. This algorithm returns a threshold that optimizes intra-class distance.

$$t = max(N_l N_h (\mu_l - \mu_h)^2) \tag{3.10}$$

Where N is the number of pixels in that class.

Triangle Thresholding Approach [98]

This algorithm finds a threshold that maximizes the distance between a maximum and the valley from the pixel intensity histogram.

Yen Thresholding Approach [99]

Using this methodology, the threshold is chosen as to maximize the information entropy of both background and foreground.

$$\text{criterion} = \max(\log(\frac{(P(x \leq t) * (1 - P(x \leq t)))^2}{P(x \leq t)^2 P(x > t)^2})) \tag{3.11}$$

3.3.3 Proposed Approach for Benchmarking Green Part Density

In this present work, the research will focus on evaluating the different standard methodologies (ISO 5017, ASTM B962, ASTM D7263, and μCT Scan) for measuring relative bulk density. Where necessary, the standards were modified to accommodate smaller permissible sample dimensions. Test procedures are performed by two operators. The measurement performance will be evaluated based on the repeatability (Gage R&R Study) and ease of

execution between methods. This study is intended to provide a benchmark bulk density to tailor X-ray computed tomography filtering, segmentation, and feature extraction algorithms deployed in subsequent studies. As such, X-ray computed tomography was also conducted, and different thresholding techniques were evaluated. The outcomes were compared with the relative density measurements.

3.4 Materials and Methods

3.4.1 Material System

For the experimental work, in this study, parts are printed using SS316L. Two powder sources were used in this work, with different powder size distributions. The first powder (316-L5520) is sourced from North American Hoganas (Niagara Falls, NY), with a batch certificate analysis stating that the sieved 50th percentile of the powder size distribution (D50) is roughly 71 μm. The second powder(SS316L) is sourced from Renishaw (Staffordshire, UK). Using an optical particle size analyzer(described later), the D50 of the Renishaw powder was measured to be $36.04 \pm 0.87 \mu m$.

In this study, two powder blends are used, labeled as Unimodal and Bimodal. The Bimodal powder was manufactured by mixing sieved powder from Hoganas and Renishaw. The mixing ratio is 15%wt of powder sieved to $< 45 \mu m$ (Renishaw)(Sieve No. 325 (Cole-Parmer, Vernon Hills, IL) with larger powder sieved to $125 - 150 \mu m$ (Hoganas) (Sieve No. 120 and 100(Cole-Parmer, Vernon Hills, IL). The resulting powder distributions for the Unimodal and Bimodal powder blends were measured using an optical particle size analyzer (Camsizer X2, Restch). The instrument operates using Dynamic Image Analysis (ISO 13322) [100]. Powder is dropped in the measurement field via a vibratory feeder. The measurement field contains a planar light source and two digital cameras. The cameras take pictures of the free-falling powder. Via built-in image processing algorithms, various properties of the particle are extracted such as minimum diameter, equivalent circle diameter, maximum diameter, aspect ratio, roundness, symmetry and convexity. In this work, the equivalent circle diameter is used as the definition of diameter (Equation 3.12). The powder size distributions for the Unimodal and Bimodal blends are shown in Fig 3.2.

$$D = \sqrt{\frac{4A}{\pi}} \tag{3.12}$$

All samples were printed using an aqueous binder (BA005, Exone, Pa, USA). The precise composition is a trade secret. However it is approximately 80% water, $2 - 20\%$

Table 3.2: Print Settings used in experiment

Process Settings	Value
Layer Thickness	150 µm
Roller Rotation	100 rpm
Linear Speed	3 m/s
Saturation	75%
Binder Set Time	5 s
Lamp Output	50%
Bed Temp	50 °C
Recoat Speed	100 mm/s
Oscillator	1950 rpm
Drying Speed	5 mm/s
Bottom Bleed Reduction	High

ethynedial and $2 - 20\%$ 2-butoxyethanol. For the calculation of the relative density, the quantity of binder was assumed to be negligible inside the parts. In the thesis of Rishmawi, using a thermogravimetric analyzer, the binder was roughly only 0.6% of the total mass. The density of SS316L was taken to be 8.00 g/cm^3 [68].

3.4.2 Binder Jetting Additive Manufacturing Process

The M-Flex system (Exone, PA, US) uses a custom single piston reduced build bed (Figure 3.3). All samples are printed on a Exone M-Flex printer. The test artifacts are 15 mm cubes. Unfortunately, this size does not follow the geometric specification in ASTM D7263 and ISO 5017. Both measurement methods require a test specimen of around 4 cm size.

Using each powder type, two batches were made. Each batch contained a set of 16 test artifacts. For each measurement type, if possible, four test artifacts were randomly sampled from each batch. Each test was performed by two operators. The binder jetting additive manufacturing process parameter settings were chosen based on prior knowledge and kept constant (Table 3.2). This combination of settings was shown to work consistently for this material system with both powder blends, Unimdal and Bimodal. Also, the builds were cured in an oven at 180 °C for 12 h to evaporate the water content and cure the binder. The samples were distributed to each operator as shown in the Table 3.3 and 3.4.

For the Computed Tomography threshold study, 18 cylinders (8 x 10 mm) were printed concurrently along with the Archimedes test artifact using Unimodal powder (13 cylinders)

Figure 3.2: Particle-size distribution obtained through the Camsizer

(a) Unimodal

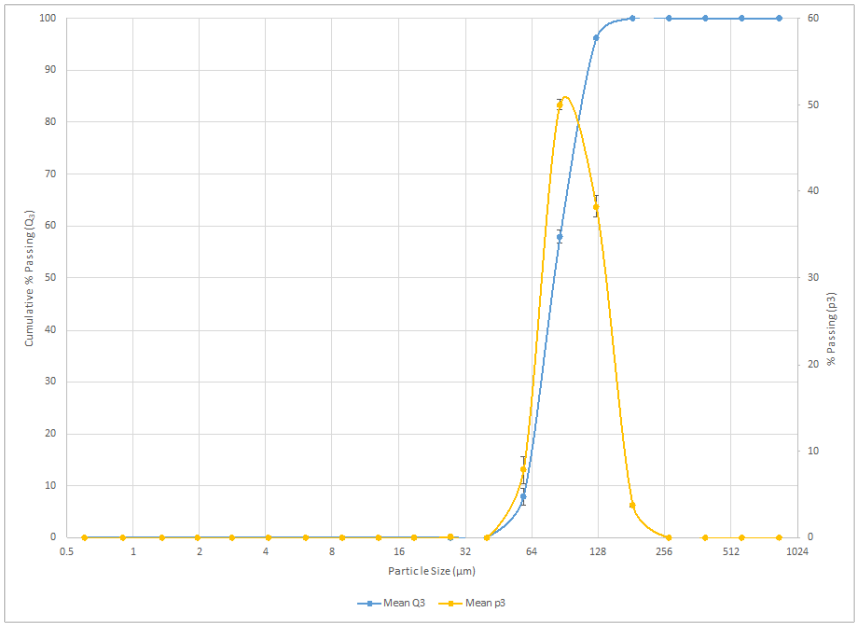

(b) Bimodal

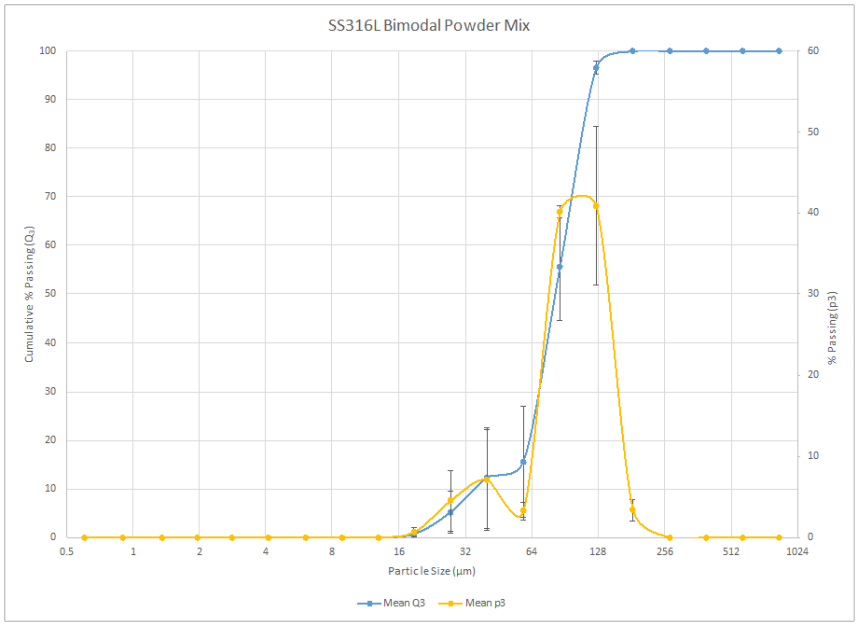

Figure 3.3: Reduced Build Bed used for printing samples

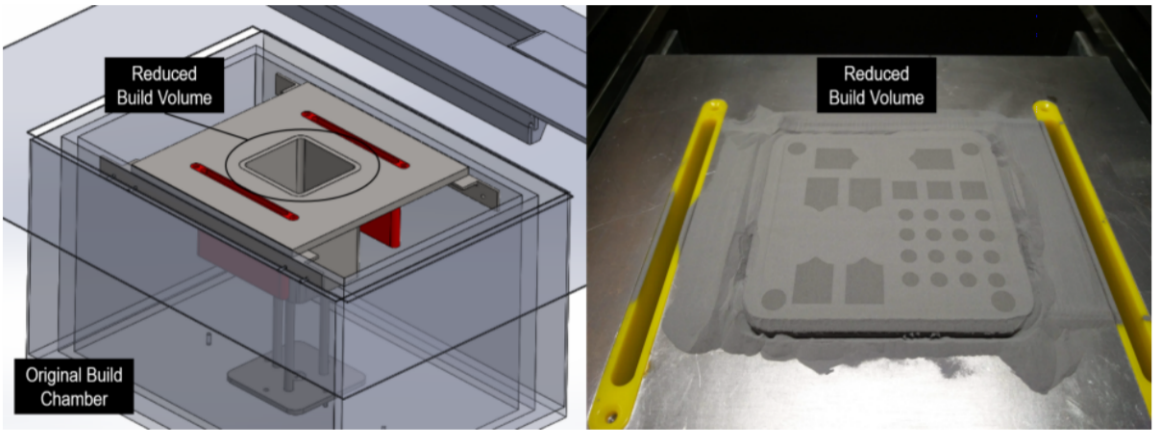

Table 3.3: Samples allocated to Operator 1

Standard	Powder type	Number of Samples
ASTM D7263	Unimodal	8
ASTM D7263	Bimodal	9
ASTM B962	Unimodal	10
ASTM B962	Bimodal	10
ISO 5017	Unimodal	8
ISO 5017	Bimodal	8

and Bimodal powder (5 cylinders).

3.4.3 Density Measurement Procedures

ASTM B962: Standard Test Methods for Density of Compacted or Sintered Powder Metallurgy (PM) Products Using Archimedes's Principle

The ASTM B962 standard is currently the most common standard used in the determination of green part density for binder jetting additive manufacturing. Although meant for powder metallurgy artifacts, it can be argued that powder metallurgy samples both in green and sintered state are analogous to metal binder jetting parts. In the green state, the powder is loosely held together. As per all ASTM standards, a repeatability

Table 3.4: Samples allocated to Operator 2

Standard	Powder type	Number of Samples
ASTM D7263	Unimodal	5
ASTM D7263	Bimodal	4
ASTM B962	Unimodal	7
ASTM B962	Bimodal	8
ISO 5017	Unimodal	7
ISO 5017	Bimodal	8

and reproducibility intervals are given. Unfortunately, those values are not quantified for green samples. Repeatability and reproducibility intervals are meant to give the user a maximum limit on the variability between samples and results between laboratories before questioning the validity of the measurement.

The precise procedure can be found in the standard itself; in summary, the steps are as follows:

1. Measure mass of sample(s) in air(A)
2. Impregnate the sample(s) with oil
3. Measure mass of sample(s) saturated with oil in air (B)
4. Measure mass of sample(s) saturated with oil in water (F)

Using the following equation, the green density can be calculated.

$$\text{Green Density}, D_g = \frac{A\rho_{water}}{B - F} \tag{3.13}$$

ISO 5017: Dense shaped refractory products Determination of bulk density, apparent porosity and true porosity

The methodology described in ISO 5017, is a typical Archimedes procedure, except water can be substituted with any liquid, as long the density of that liquid is known at the operating temperature. This method is similar to ASTM C373, which was used in previous studies. In summary, the steps are as follows:

1. Measure mass of sample(s) in air (m_1)

2. Impregnate sample(s) with fluid
3. Measure mass of wet sample(s) suspended in fluid (m_2)
4. Remove sample from balance and measure mass of soaked piece (m_3)

$$\text{bulk density}, \rho_b = \frac{m_1}{m_3 - m_2} * \rho_{liq} \tag{3.14}$$

$$\text{apparent porosity}, \pi_a = \frac{m_3 - m_1}{m_3 - m_2} * 100 \tag{3.15}$$

$$\text{true porosity}, \pi_t = \frac{\rho_{\text{solid}} - \rho_b}{\rho_{\text{solid}}} * 100 \tag{3.16}$$

ASTM D7263 : Standard Test Methods for Laboratory Determination of Density (Unit Weight) of Soil Specimens

The methodology described in ASTM D7263 is a test method to determine the bulk density of undisturbed soil. Using the water displacement technique, the procedure is as follows:

1. Measure mass of sample(s) (M_t)
2. Apply two coats of wax to the sample(s)
3. Measure mass of Coated sample(s) (M_c)
4. Measure mass of Coated Sample(s) submerged (M_{sub})

$$\text{density}, \rho_b = \frac{M_t}{\frac{(M_c - M_{sub})}{\rho_{water}} - \frac{(M_c - M_t)}{\rho_{wax}}} \tag{3.17}$$

Table 3.5: X-ray Computed Tomography Scan Settings

Powder type	Resolution (μm)	Projections	kV
Unimodal	12	1600	140
Bimodal	5	400	140

CT Acquisition and Thresholding

Previous studies have investigated the influence of CT scan parameters on porosity measurement [102]. They found that increasing the number of projection decreases noise in the image. Furthermore, they recommend using low source powers for porosity measurement. The number of projection was reduced to reduce acquisition time, while trying also keep noise at an acceptable level. Both the scan time of the Unimodal and Bimodal powder parts were kept below 30 min to keep cost down. All CT datasets were acquired on a ZEISS Xradia 520 and reconstructed using ZEISS proprietary software. Table 3.5 summarizes the computed tomography settings.

Each CT-scan image is thresholded using each of the described algorithms and a density value($\hat{Y}_i$) is calculated along with a confidence interval. The confidence interval is computed at 95% confidence with the following equation:

$$\overline{x} \pm t * \frac{s}{\sqrt{n}} \tag{3.18}$$

Where s is the sample variance. n is the number of samples. $t*$ is the critical value from t distribution table. Furthermore, all images are initially denoised using the non-local mean denoising algorithm. The settings are shown in section A.1.

3.4.4 Gage Repeatability and Reproducibility (R&R) Study

According to the Committee for Weights and Measures (CIPM) and the National Institute of Standards and Technology, uncertainty in a measurement can be classified in two categories [103].

1. Type A: those which are evaluated by statistical methods
2. Type B: those which are evaluated by other means

As a rule of thumb, Type A uncertainty can be calculated by finding the standard deviation of the measured quantities in a current measurement process, while Type B uncertainties are calculated from previous knowledge such as

1. Previous Experiment
2. Calibration report
3. Manufacturer specification
4. Assigned value from handbook or standards

The goal of an R&R study is to evaluate the quality of a measurement system and compute uncertainty of type A. The quality is measured by determining how much of the variability within the data can be attributed to the measurement process and how much is from the measured sample. The variability attributed to the measurement process is further divided into two categories: repeatability ($\sigma_{\text{repeatability}}$) and reproducibility ($\sigma_{\text{reproducibility}}$).

Repeatability is variation under fixed condition such as within the machine or operators. Reproducibility is the variation under different conditions. Typically a R&R study is done using Analysis of Variance using either a Random or a Mixed-Effect model [104]. A confidence interval is estimated from the data using either Modified Large Sample method or the Generalized Confidence Interval. As per NIST specification, the confidence interval is listed at 95%. In typical case, this corresponds to twice the sample standard deviation [103]. If the measurement process is meant for quality assurance, a misclassification rate can be calculated as well given a lower bound and upper bound specification.

3.4.5 Regression Using Bayesian Inference

The experiment in this present study has one fixed factor (powder type) and one random factor (operator). The analysis is conducted as a Mixed Model Analysis of Variance (ANOVA). As shown in Table 3.3 and Table 3.4, the treatment combinations do not have the same numbers of replicates. Therefore, the dataset is unbalanced. Also, there are only two levels for the random operator factor. Estimation of the reproducibility will be inaccurate. Consequently, the only the gage error will be estimated ($\sigma_{\text{gage}} = \sigma_{\text{repeatability}} + \sigma_{\text{reproducibility}}$). The analysis was conducted using Bayesian Inference as shown by Weaver et al. [105]. Furthermore, to maintain robustness against data imbalance, this approach lets us estimate a confidence interval on the estimated gage error. As long the model is correctly specified, the procedure is identical regardless of the model type.

The central pillar to Bayesian Inference is the Bayes Theorem:

$$P(\theta|Y) = \frac{P(Y|\theta)P(\theta)}{P(Y)} \tag{3.19}$$

Each factor expressed in the Theorem can be interpreted as follows:

1. Likelihood($P(Y|\theta)$): Given a model having parameters θ and observed data Y, $P(Y|\theta)$ is the probability of Y being generated by θ.
2. Posterior ($P(\theta|Y)$): The Posterior is the probability of θ given the observed data Y,
3. $P(\theta)$ and $P(Y)$ are the probability of θ and Y taking specific values. $P(\theta)$ is called the prior and represent existing knowledge of the model. Therefore, if present knowledge of uncertainty of type B can be included in the prior.
4. $P(Y)$ is sometimes written as $\int P(Y|\theta)P(\theta)d\theta$

The measurement process was modeled as described by equation 3.20 :

$$y_{ijk} = \mu_i + Part_{j(i)} + \epsilon_{k(ij)} \tag{3.20}$$

Each powder type follows a global mean density μ_i. Since the measurement is destructive, therefore the same parts cannot be measured using different methods. Consequently, $Part_{j(i)}$ represent the nesting relationship between the Fixed effect of the powder and the measurement of each part. Finally, $\epsilon_{k(ij)}$ represents the measurement error (σ_{gage}). An operator and a batch random effect were previously included in the model. Including the two effects caused the sampler to diverge. The cause of the divergence was likely due to the low number of replicates for the operator(2). As for the batch effect, the removal did not change the estimated value for σ_{gage}. Therefore, it is likely that the variance due to the batch is very low. The model is set up as follows:

$$\begin{aligned}
\{\mu_i \sim Uniform(20.0, 60.0) : i = \{\text{Unimodal}, \text{Bimodal}\}\} \\
\text{Part}_{j(i)} \sim N(0, \sigma_{\text{part}}) \\
\mu = \mu_i + \text{Part}_{j(i)} \\
y_{ijk} \sim N(\mu, \sigma_{\text{gage}})
\end{aligned}$$

$$\sigma_{\text{part}} \sim \text{HalfCauchy}(25) \tag{3.21}$$

$$\sigma_{\text{gage}} \sim \text{HalfCauchy}(25) \tag{3.22}$$

If no previous knowledge exists of the model. It is recommended to choose a non-informative prior as not to bias the posterior. The prior (Equation 3.21, Equation 3.22) was defined following the recommendation by Gelman and others [106].

The goal of inference is to find a set of θ that maximizes the posterior. Unfortunately, the expression $\int P(Y|\theta)P(\theta)d\theta$ is unsolvable since the shape of the function $P(Y|\theta)P(\theta)$ is unknown. The exception is when the likelihood and $P(\theta)$ are conjugate function of each other ($f * g \rightarrow c \cdot f$). Hence, computing the posterior numerically is the sole solution. Metropolis-Hasting is the simplest Markov-Chain Monte Carlo (MCMC) algorithm. It avoids computing the integral by using the following trick (eq. 3.23):

$$\text{AcceptanceRatio} = \frac{P(\theta|Y)}{\frac{P(Y|\theta_0)P(\theta_0)}{P(Y)}} = \frac{\frac{P(Y|\theta)P(\theta)}{P(Y)}}{\frac{P(Y|\theta_0)P(\theta_0)}{P(Y)}} = \frac{P(Y|\theta)P(\theta)}{P(Y|\theta_0)P(\theta_0)} \tag{3.23}$$

A value of θ_0 is sampled from a known distribution function. The value of θ_0 is saved when the Acceptance Ratio reaches a threshold. It can be shown that θ_0 sampled in this manner is equivalent to sampling directly from the posterior[107]. Once the algorithm accumulates enough θ_0, then the posterior probability can be approximated.

The manner θ_0 is sampled and the criteria for keeping each parameter will depend on the sampler used. For Metropolis-Hasting, accumulating enough samples for accurately approximating the posterior is time consuming. The sampling, also known as the random walk, is not efficient. In other words, each iteration does not always add more information. For efficiency purpose, the pymc3 implementation of the No-U-Turn sampler (NUTS) was used in this study[108]. NUTS is a Hamiltonian random sampler which doesn't have the inefficient random walk of the Metropolis-Sampler. In addition, the parameters are automatically tuned on the fly. Parameter tuning was the major drawback of the original Hamiltonian sampler [109].

The σ_{gage} is defined in terms of highest density interval(hdi). The hdi is the interval at which 95% of the estimated values falls into.

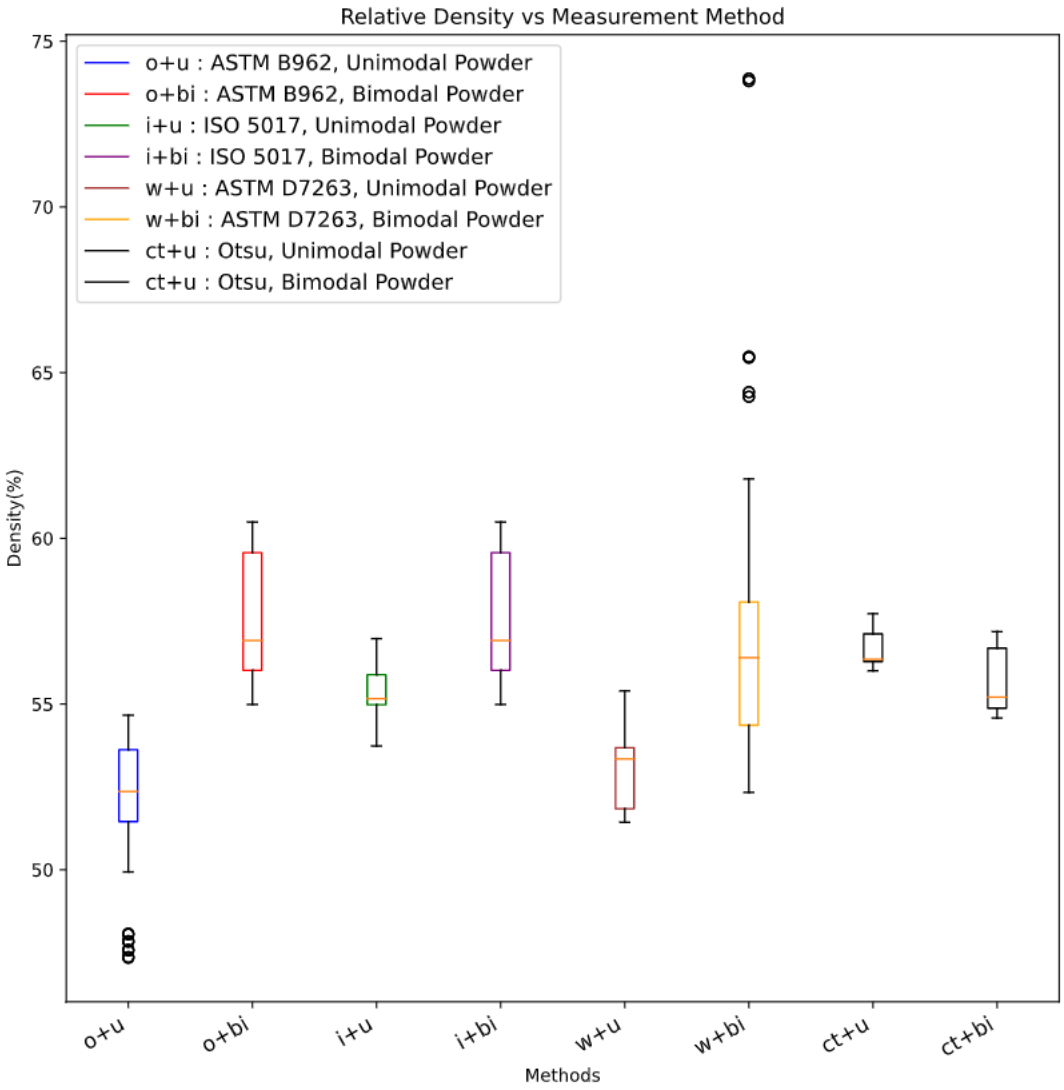

Figure 3.4: Box-plot relative density measurement of all measured samples. CT density using otsu is shown for comparison

Table 3.6: ISO 5013 : Relative density inference results

Parameters	Low	High
Bimodal Parts	56.25	57.61
Unimodal Parts	54.04	55.55
σ_{gage}	0.3392	0.3778

Table 3.7: ASTM B962 : Relative density inference results

Parameters	Low	High
Bimodal Parts	52.85	54.55
Unimodal Parts	50.82	52.62
σ_{gage}	0.4076	0.4746

3.5 Results and Discussion

3.5.1 Archimedes Results

The fitness of the models and the data for each experiment are shown in detail in Appendix A. From Figure 3.4, we can observe that both ASTM D7263 and ASTM B962 techniques registered similar ranges of values. On the other hand, the ISO 5017 method measures density value consistently higher than the rest. In the absence of a widely accepted calibration artifact for porosity determination, no comment can be made on the true density value based on these measurements alone. As such, the efforts will reside in quantifying uncertainty. A regression using the method specified in section 3.4.5. The mean density and gage error is estimated for both parts made using Unimodal and Bimodal powder. The results are shown in Tables 3.6, 3.7 and 3.8.

From the inference results, we see that estimated values for parts made with both Bimodal and Unimodal powder do not overlap. The density of parts manufactured using bimodal powder is higher than parts made using unimodal powder [43].

Table 3.8: ASTM D7263 : Relative density inference results

Parameters	Low	High
Bimodal Parts	55.14	58.06
Unimodal Parts	51.23	54.54
σ_{gage}	1.793	2.204

ISO 5013 is the method with the smallest gage error. This is followed closely behind by ASTM B962 and far behind ASTM D7263. The estimated gage error for ISO 5013 is between 0.34% and 0.38%. Compared to Spierings et al. [75] (0.18%) which uses wax and du Plessis et al. [87] ($\frac{0.02g/cc}{8.00g/cc} * 100 = 0.25\%$) using CT, the uncertainty is comparable. Both Spierings et al. and du Plessis et al. were measuring laser powder bed parts. In addition, the calculated uncertainty is similar to Pinot [71] ($0.1 - 0.5\%$) which also evaluated ISO 5013.

Pinot used the 5M method to systematically analyze the sources errors. The 5M method divides the process into 5 components that lead to errors:

- Man : operator proficiency, training, ...
- Material : Samples heterogeneity, spatial, temporal correlation, ...
- Medium : Room humidity, temperature, ...
- Method : Sampling strategy, bias, ...
- Measurement : Measurement instrument resolution, stability, ...

For ISO 5017 and ASTM B962, a source of error is in the handling of the samples during measurement (Man). Taking the sample out of the solution for weighing needs to be done quickly so that the liquid doesn't leak out. Furthermore, wiping the sample can remove more liquid than it should. Liquid leaking out of the sample will underestimate the quantity of liquid present in the sample. This in turn leads to underestimating the density. Also, for ISO 5017, it was observed the wet sample weight kept decreasing due to isopropanol evaporation (Method, Measurement). For both ISO 5013 and B962, saturation of the sample with oil or isopropanol can be imperfect due to initial presence of water and air trapped inside (Material).

For B962, one cause of variance is the loss of oil through the manipulation and the water intrusion inside the samples (Method). The oil acts as a sealant against water penetrating the surface connected pores. Unfortunately, ASTM B962 specifies the use of a low viscosity oil. This ensures the oil penetrates the part easily. But the oil can leak out easily as well thereby letting water in during the experiment.

For wax, one possible source of error is that coating the sample can trap a non-negligible quantify of air between the wax and the part surface (Material). This phenomenon was observed by le Roux et al. [110] as well when studying soil sample using microtomography.

Table 3.9: Relative density means Unimodal powder

	otsu	isodata	li	mean	yen	triangle	Minimum
Mean rel. Density (%)	56.62	56.95	66.89	52.83	55.29	0.02	96.3
$\pm$ Confidence Int. ($\alpha = 0.05$)	0.31	0.27	0.35	0.14	0.36	0.05	0.21

Wax can also penetrate too deep inside the sample which can cause an underestimation of the wax quantity present in the sample. For the ASTM D7263 standard, this is alleviated by having a large sample which dampens this variance. However, this is not the case for this experiment. Also, if the wax coating is not airtight, water will infiltrate the sample therefore destroying it. Out of 34 samples tested, 8 samples were compromised in this manner.

Another source of error, for all methods, the measurements were not performed in a temperature-controlled room. Unfortunately, temperature variation of $0.5°C$ was observed (Medium). Also, the liquid impregnation in ASTM B962 and ISO 5017 was done by drawing the air out of the chamber while the sample is held in the liquid. This method can leave air trapped inside the sample. An improvement would be to put the sample under vacuum first. Once, the vacuum is achieved, the liquid is introduced inside the chamber submerging the samples. This would ensure the complete replacement of the air by the liquid. ASTM C373 and ISO 5017 suggest using this method for liquid impregnation. This was not done in this study due to the unavailability of a pressure vessel with a liquid inlet. Also, the printhead was discovered to be damaged and jetting uneven quantity of binders (Material). Therefore, the assumption of binder having a negligible effect on density measurement is possibly incorrect.

For future work using ISO 5017, certain steps can be done to minimize the variability further. The measurement can be done in a controlled environment. This is to reduce variability caused by the immersion medium. In addition, the immersion liquid (Isopropanol) can be swapped for another less volatile liquid, as it was noticed that sample were drying relatively fast.

3.5.2 Thresholding Results

From the Table 3.9 and Figure 3.5, we see that the thresholding techniques that is the closest to the Archimedes density value (ISO 5017) are Isodata, Otsu and Mean. Minimum threshold failed to converge for Bimodal scans and Triangle threshold did not provide reasonable results. Possible reasons for the failure of Triangle and Minimum is the histograms

Table 3.10: Relative density means Bimodal powder

	otsu	isodata	li	mean	yen	triangle	Minimum
Mean Density (%)	55.70	56.41	64.87	52.09	70.06	96.68	N/A
$\pm$ Confidence Int. ($\alpha = 0.05$)	1.44	1.35	2.06	0.56	6.00	5.67	N/A

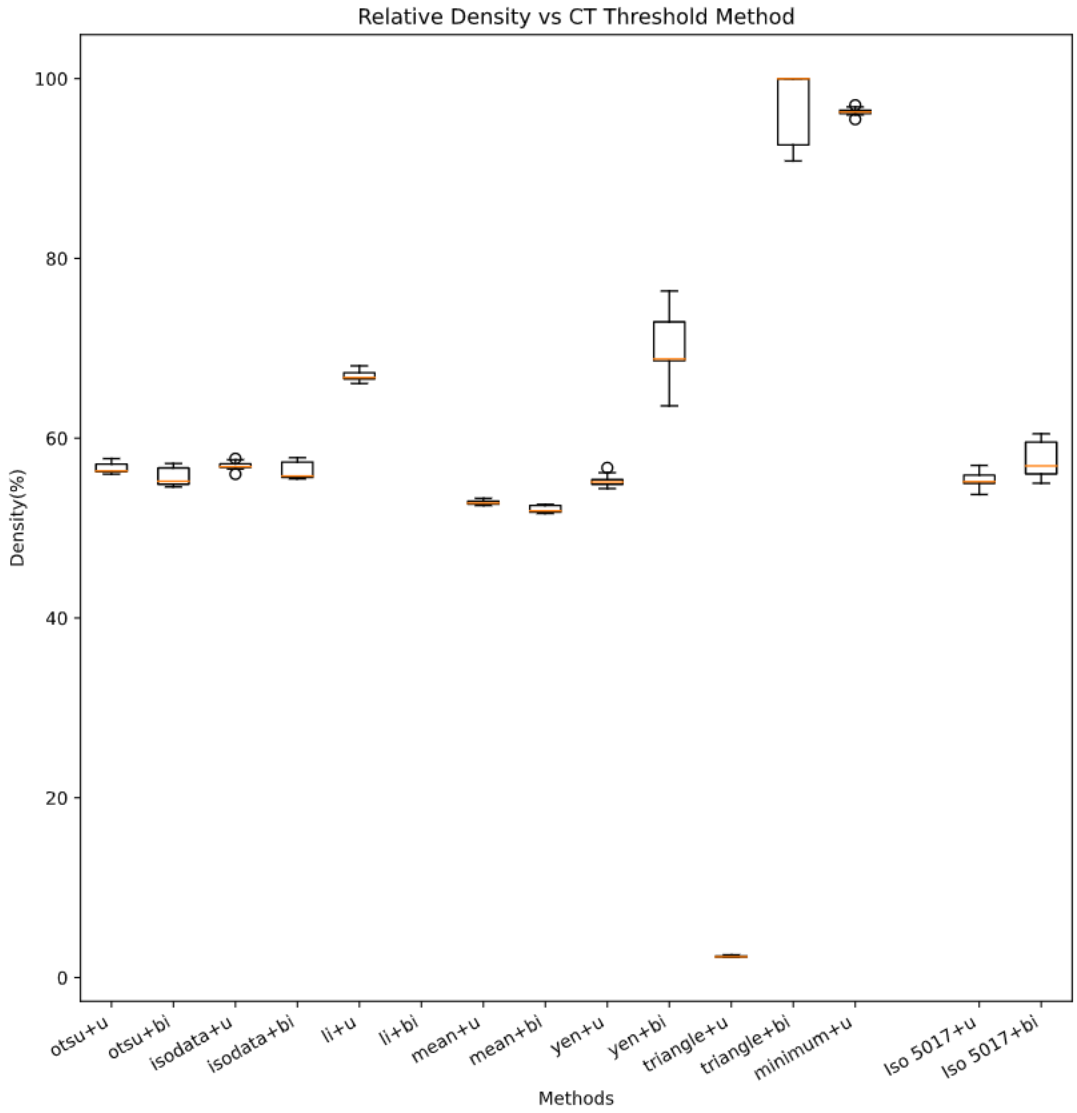

Figure 3.5: μCT Density, ISO 5017 is shown for comparison, u: unimodal, b: bimodal

does not have the typical twin peaks and valley shape (Figure 3.6).

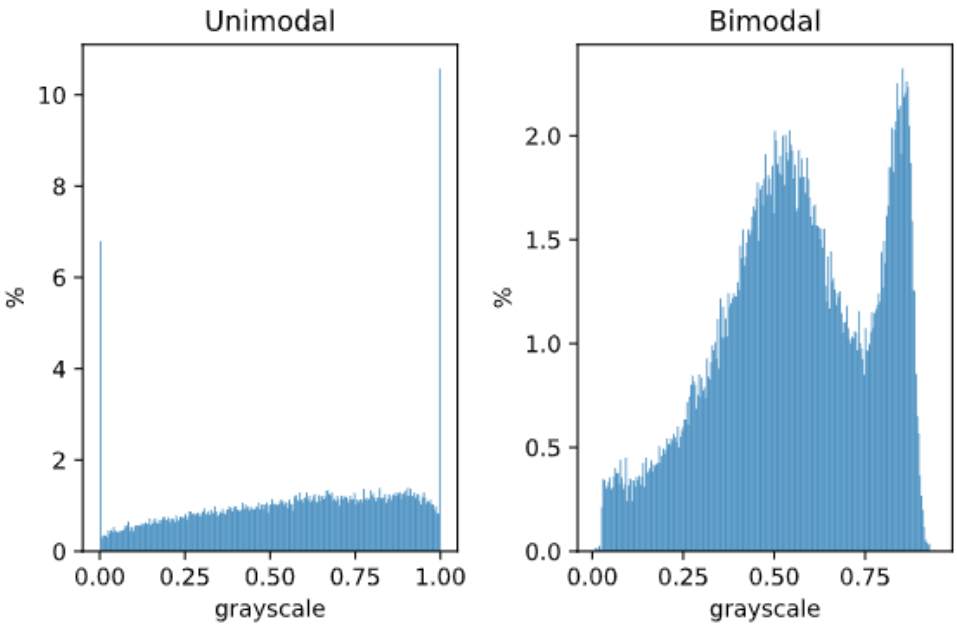

Figure 3.6: Grayscale histogram of CT image

From the Table 3.10, we see that simple thresholding does not work as well for scans of bimodal powder. Upon visual inspection (Figure 3.7b), the small particles are not well resolved due to insufficient resolution. The parts can be scanned at higher resolution but this would unacceptably increase data acquisition cost. One solution is to map the X-ray attenuation value to a continuous density value as shown by Bruns et al. [111]. The other alternative to keep cost of μCT data acquisition low is to use sparse-view reconstruction[112] or use iterative reconstruction method[85]. Alternatively, Zhu et al. used deep learning based sparse reconstruction algorithm for scanning BJAM parts. They reduced their scanning time by 15 for green BJAM parts.

3.6 Summary and Outcomes

In conclusion, ISO 5013 is the preferred method of bulk density determination, as, it has the smallest σ_{gage}. With a mean σ_{gage} of 0.36%, this method is competitive with other measurement methods such as CT. Also, the procedure is simple and clean. A possible

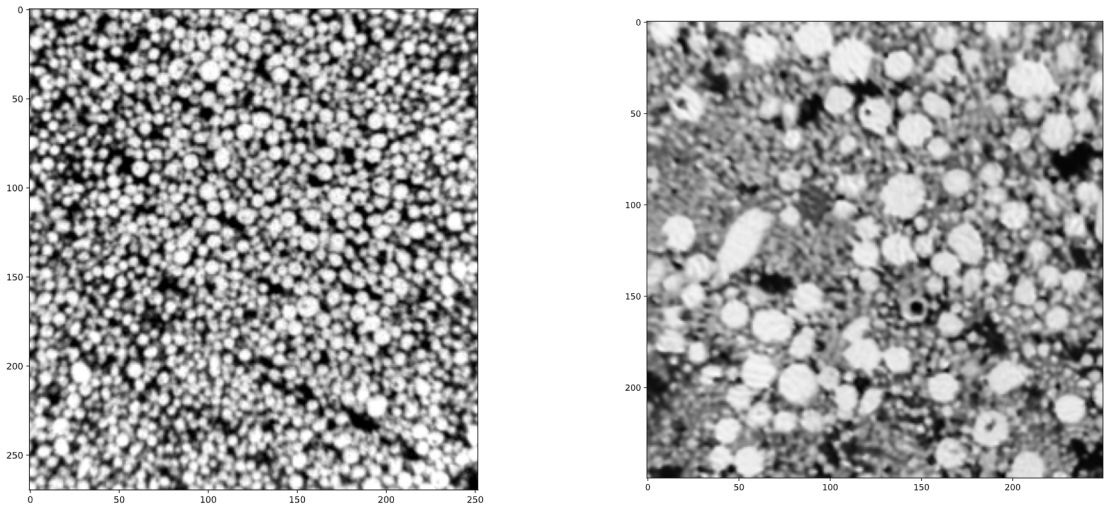

(a) Unimodal part

(b) Bimodal part

Figure 3.7: μCT scan slice

improvement would be to use a less reactive liquid, use a temperature-controlled enclosure and use a different liquid impregnation strategy. Furthermore, the use of a non-wetting fluid such as Mercury can be investigated. Non-wetting fluid has the advantage of not penetrating the surface connected pores unless subjected to pressure. For thresholding, otsu, isodata and mean thresholding all give reasonable results. This finding agrees with the work of Iassonov et al. [90] which also found Otsu and Isodata were the most accurate global threshold method for porous materials. A caveat, for Bimodal powder all three thresholding techniques underestimate the density. These conclusions were leveraged in the analyses deployed in subsequent chapters.

Chapter 4

Particle Detection

4.1 Background

In Binder Jetting Additive Manufacturing (BJAM), parts printed need to be sintered in an oven. When the density of the green object is low. Full densification through sintering will result in substantial shrinkage. As the mass stay the same and density increase, volume must decrease. It was shown by Bai et al. that using Bimodal powder increases the density of the green sample and in some cases the sintered density compared to monosized powder. This is due to the smaller particles filling the interstitial space between the bigger particles. Unfortunately, the Bimodal powder was also observed to sometime segregate into its own layers (fig. 4.1) [1]. After sintering, the particle segregation eventually leads to density variation. Stevens et al. observed density variation throughout the part as well [113]. In both cases the particle segregation and density variation were detected through visual inspection. Although in the work of [1], the cause of the segregation was not determined. If particle segregation were to be linked to process parameters. Consequentially, particle segregation needs to be quantified over many prints. Therefore, an automated and low cost tool to detect and quantify density and particle segregation is needed.

4.2 Particle Segregation

As stated by Wheat et al., Stevens et al. [1, 113], particle segregation and density variation were observed in the samples printed via binder jetting additive manufacturing. To date, there have been few studies which detail the particle and pore space architecture in binder

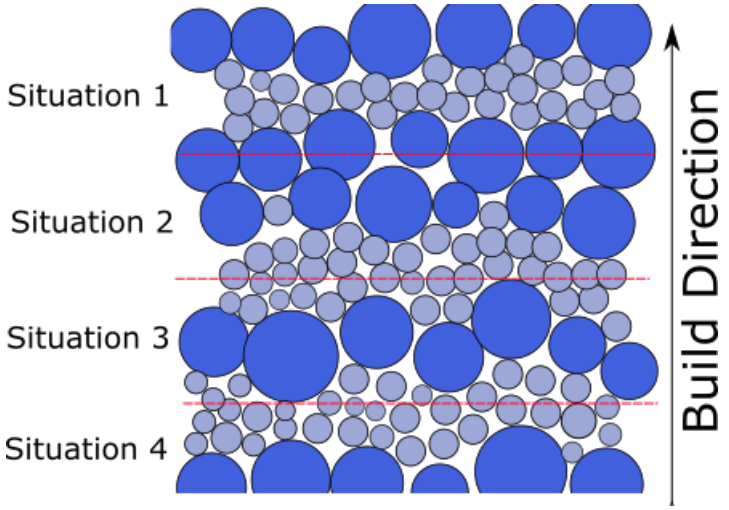

Figure 4.1: Layer by layer particle segregation shown by Wheat et al. [1]

jetting, specifically in extracting the spatially resolved characteristics of the parts. The purpose is to have a deeper understanding of the relationship between process parameters and green part characteristics. Therefore, there's a need to develop tools to observe such detailed characteristics. In this chapter, given the use of powder with a Bimodal size distribution, segregation of particles can happen through many mechanisms. The segregation mechanisms relevant to the binder jetting additive manufacturing process can be classified into 4 classes as detailed below [5], with their effects visualized in Figure 4.2:

1. Trajectory-Depended Segregation: Particles are in flight or have a high-rolling or moving velocity. This is only a problem for large particles (>250 µm) [5].
2. Sieving-Depended Segregation: Small particles moving through the interstitial space of large particles through external forces (vibration or motion).
3. Fluidization-Depended Segregation: Present when the powder bed has fluid like behavior. The large particles sink to the bottom. Occurs with highly aerated fine particles.
4. Agglomeration-Depended Segregation: Forms when fine particles stick together due to electrostatic, van de Walls forces and surface tension.

Superficially, all four of the mechanism appear to be present during the printing process. In the printer used in the lab, the powder is manually loaded inside a hopper which presents

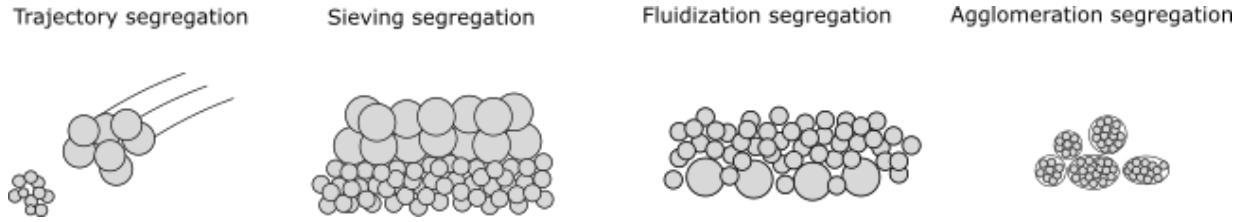

Figure 4.2: Schematic of four proposed primary segregation patterns by Tang and Puri [5]

opportunity for sieving segregation to occur. Also, the printer uses a vibrating mechanism to dispense powder. This can promotes segregation of type 2. Given the small particle diameter, segregation of type 4 are entirely possible to occur during the powder spread cycle. Powder segregation occurs more often in free-flowing powders [5].

4.2.1 Quantifying Segregation

To evaluate the effects of print parameters on particle segregation, an unbiased metric for quantifying segregation is necessary. In literature, a plethora of mixing indexes have been proposed. One early review work listed 30 different particle segregation metrics [114]. The listed metrics fall into two classes, they are either derived based on data acquired from digital images or derived via direct sampling of the powder material system. The majority of the segregation quantifiers measure the deviation between the concentration of one component or object cluster of one area versus another. One possible metric for estimating particle segregation via using digital images is the segregation intensity; this metric has been deployed in literature outside of the additive manufacturing space and summarized below [115, 116]:

$$I_s = \sqrt{\frac{\sum_{i=1}^{N}(C_b - C_{avg})^2)}{N-1}} \tag{4.1}$$

$$C_b = \frac{A_b}{A} \tag{4.2}$$

I_s is the segregation intensity; N is the total number of measurement regions; A_b is the total pixels belonging to large particles inside a measurement region; A is the total pixel area; C_{avg} is average large particles concentration. I_s is bounded between 0 and 0.5. 0 denotes a fully mixed system and 0.5 a fully segregated system. In Keller et al.

[117] measured concentration at different locations, while varying the measurement volume. In another work, particles were counted inside digital images [118]. Since the image encompassed multiple print layers, a fast fourier transform (FFT) was used to measure the cyclical nature of the variation in density. Previous authors have used FFT to capture spatial variation in concentration of types of clusters of particles within a region in space [119, 120]. In Shin and Fan [119], they further found that the maximum power spectrum (i.e., the square of the FFT) varies inversely with the frequency of the variation.

The second class of quantifiers was derived with manual sampling in mind. Similarly, they measure the degree of variation among different spatial domains within the powder system. Instead of using digital images, these methods rely on direct measurement of the powder size concentration. In literature, numerous metrics have been devised. In particulate research, the most widely used index is the Lacey index (M_1) and its derivative [121, 122]. For further sensitivity, the log version is called the Ashton and Valentin mixing index (M_2) [123]. Even with the presence of more advanced index, researchers still use the Lacey index for its simplicity [124, 93, 125]. The following nomenclature is used for all segregation metrics.

N_R : Number of measurement locations
N : Number of measurements
p_{ij} : concentration of material at location i and replicate j
$\overline{p}$: average concentration of material
n : number of particles
p : Feedstock concentration in a Binary Mixture

$$S_R^2 = \frac{p(1-p)}{n} \tag{4.3}$$

$$\overline{p} = \frac{\sum_i^{N_R} \sum_j^{N} p_{ij}}{NN_R} \tag{4.4}$$

$$S^2 = \frac{1}{NN_R - 1} \sum_i^{N_R} \sum_j^{N} (p_{i,j} - \overline{p})^2 \tag{4.5}$$

$$M_1 = \frac{S_0^2 - S^2}{S_0^2 - S_R^2} \tag{4.6}$$

$$M_2 = (\frac{\log S_0^2 - \log S^2}{\log S_0^2 - \log S_R^2})^{(1/2)} \tag{4.7}$$

Wen et al. examined 8 different metrics to quantify particle segregation [124]. The metrics were evaluated based on complexity and parameter dependency. They deemed the nearest neighbor method [126] to be easiest to implement with the least number of parameters dependency, although close behind was the Lacey Index owing to its grid size dependency. In another paper by McGlinchey [127], the author compared 9 segregation metrics. They found that among all the metrics compared only the F-value by Rollins et al. followed a distinct trend [128]. Since the index computation is derived from ANOVA, Rollins et al. argues that the test is still robust even when the assumption of normality is severely violated [128]. The index defined by Rollins et al. is described in the Equations below:

$$MSTr = \frac{\sum_{j=1}^{N_R}(\overline{p}_j - \overline{p})^2}{N_R - 1} \tag{4.8}$$

$$MSE = \frac{\sum_{j=1}^{N_R}\sum_{i=1}^{N}(p_{ij} - \overline{p}_j)^2}{N_R N - N_R} \tag{4.9}$$

$MSTr$ is the mean square error due to segregation. The null hypothesis(H_0) is that variance due to segregation is not significant. If the Null hypothesis is true then:

$$F = \frac{MSTr}{MSE} \sim F_{N_R-1, NN_R-N_R} \tag{4.10}$$

As shown by Wheat et al.[1], the segregation in binder jetting occurs on a layer by layer basis. Since layers in AM are set in the micron range, physical sampling is impossible. One method to view the inner structure of the part is through cold mounting and sectioning. Unfortunately, this was not successful due to the fragility of the samples. Therefore, μCT was the only option for observing particle segregation.

4.2.2 Panoptic Segmentation

To observe and quantify particle segregation using the metrics listed in section 4.2. The μCT image must be divided into background and particles (semantic segmentation). Furthermore, each particle must be accurately demarcated (instance segmentation). In the COCO dataset [6], panoptic segmentation quality is the following:

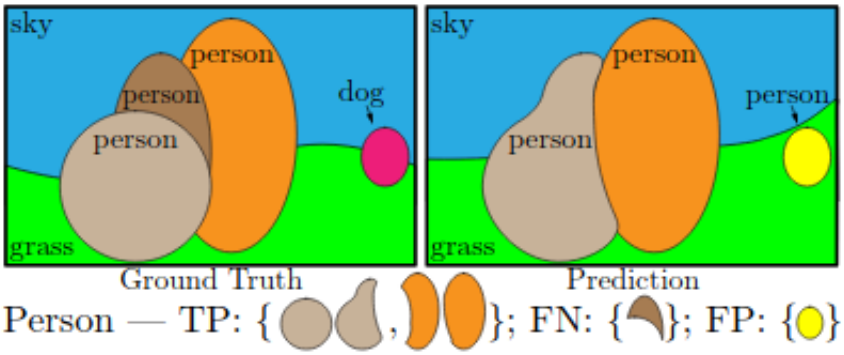

Figure 4.3: Panoptic segmentation toy example [6]

$$PQ = \frac{\sum_{(p,g)\epsilon TP} IoU(p,g)}{|TP| + \frac{1}{2}|FP| + \frac{1}{2}|FN|} \tag{4.11}$$

Given a prediction p and a ground truth g (toy example shown in figure 4.3), a True Positive (TP) is a pair of labels from prediction and ground truth that have an intersection over union (IOU) value higher than 0.5. A False Positive is an incorrect prediction. A False Negative is an undetected object. The Panoptic segmentation quality is further divided into two components : the Segmentation Quality (SQ) and the Recognition Quality (RQ).

$$PQ = \underbrace{\frac{\sum_{(p,g)\epsilon TP} IoU(p,g)}{|TP|}}_{SQ} \times \underbrace{\frac{|TP|}{|TP| + \frac{1}{2}|FP| + \frac{1}{2}|FN|}}_{RQ} \tag{4.12}$$

SQ can be interpreted as the average IOU for each True Positive (TP), while, on the other hand, RQ is the $F1$ score (eq. 4.13). The $F1$ score is the harmonic mean between the precision (How much of the Prediction is correct) and the recall (how much of the ground truth is detected).

$$F_1 = \frac{2}{Precision^{-1} + Recall^{-1}} = \frac{2}{(\frac{|TP|}{|TP|+|FP|})^{-1} + (\frac{|TP|}{|TP|+|FN|})^{-1}} = RQ \tag{4.13}$$

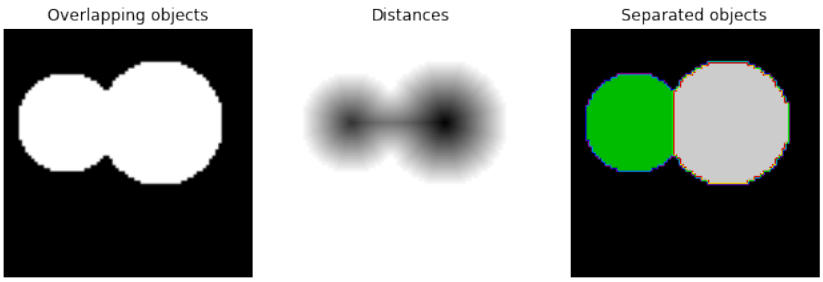

Figure 4.4: Watershed segmentation example

4.2.3 Particle Detection

To calculate the particle segregation metrics listed in section 4.2.1, a reliable method for segmenting particles spatially is needed. The traditional approach is to sample manually the powder either using a probe or through careful scooping. Afterward, the particle size distribution is measured through sieve analysis or by using a particle size analyzer. In our case, since the segregation happens on a layer by layer basis, μCT is used. When using μCT, the image needs to be segmented to identify the void and solid constituents of the image. Furthermore, each particle needs to be delineated into a distinct object. This is Panoptic Segmentation (section 4.2.2). For circular particles, the typical approach is to use watershed segmentation [129, 130]. Watershed segmentation works by applying a distance transform over a binary image. Pixels that are the furthest from the edges have the highest values. For circular shapes, the pixel with the highest value corresponds to the center. The peaks are used as the seed for the watershed transform. The challenge is that the addition of non-circular shapes, noise and object overlaps impedes such peak finding. Approaches to peak finding are to either use manual or automatic thresholding [130], deploy local maxima finding algorithms [129, 131] or use curvature algorithms [132]. These peaks are uniquely labeled and are used as a starting point for the "flooding" of the image. Flooding is defined as growing the area around the peaks until all the pixels are labeled. The flood stops at the edges of the shape or when it encounters another flood. As shown in Figure 4.4, the watershed technique can separate the overlapping circles.

Unfortunately, depending on the quality of μCT datasets, such method may not yield satisfactory results. Such was the case for our experiment at hand, as the powder used was not always circular. Non-spherical powders is a common occurrence in BJAM. This resulted in the algorithm oversegmenting large and irregular shaped particles. The solution is to post-process the segmentation by merging back the over-segmented instance. This adds complexity to the algorithm and increases running time.

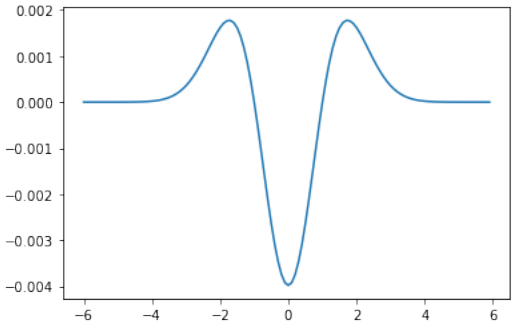

Figure 4.5: Laplacian of a Gaussian in 1D

An alternative is to use a blob detection algorithm. This technique was used by Voss et al. to pick particles in electron microscopy image. Blob detection algorithms can come in numerous forms [133]. The common approach is to deploy the Laplacian of a Gaussian (LoG) or its derivatives as a kernel in processing the image. The detector works by convolving the image with the kernel. The kernel is populated by the LoG as illustrated in the Figure 4.5. Convolving the kernel with the image ideally acts as an edge detector. When the kernel encounters a transition corresponding to an edge of a particle, it results into a strong positive response on the low pixel value side and a strong negative response on the high pixel value side. This is illustrated in figure 4.6. Therefore, the LoG function can be used as an edge detector. By varying the variance of the Gaussian, for closed polygon shapes or blobs, it is possible to collapse the negative peaks together. By recording the width of the Gaussian when this happens, it is possible to determine the size of the blob. Unfortunately, the poor μCT resolution can blur the boundaries between particles. Therefore, agglomeration of small particles can be detected as a single large particle. This issue is particularly prevalent in the datasets explored in this chapter, specifically when deploying Bimodal powders in the binder jetting process.

As a third alternative to particle detection, the last technique explored in this work is the use of feature recognition. In the last decade, Deep Learning has revolutionized image processing. Although still a black box for many, researchers are slowing unveiling the mystery behind them. Research in understanding the reason behind Deep Learning effectiveness is still ongoing. We refer the reader to the following articles by Lin et al. and Olah et al. for further reference [134, 135]. It is suspected that Neural Networks are effective because they model extremely well the hierarchy of nature. Each layer of the neural network takes on a purpose such as filtering noise or detecting features.

In this present work, the focus will be to deploy the Mask R-CNN network architecture

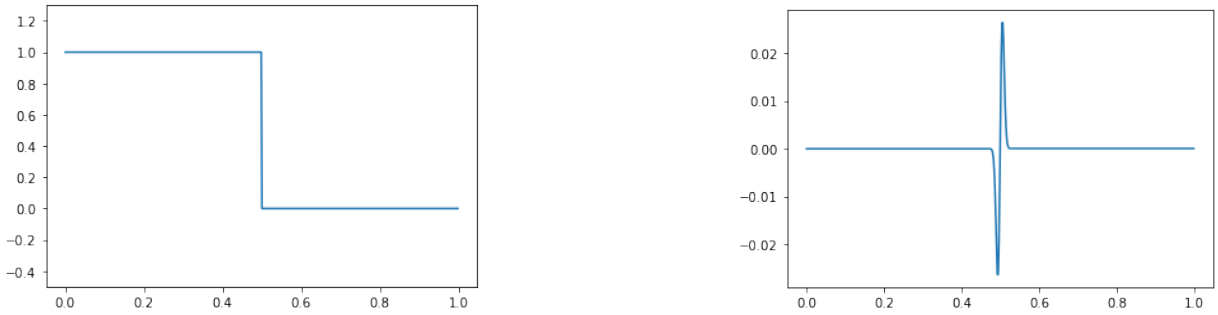

(a) Step signal

(b) Signal after LoG filtering

Figure 4.6: LoG signal response

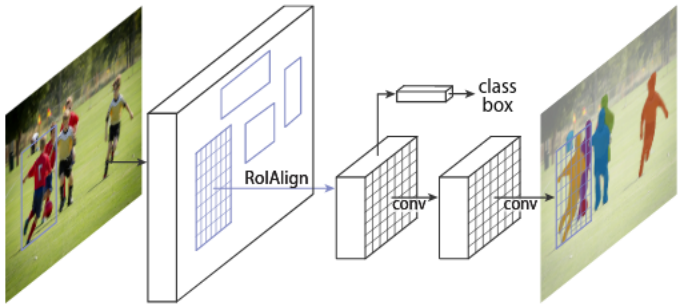

Figure 4.7: Mask R-CNN framework for instance segmentation [7]

for testing its efficacy in particle detection for a difficult Bimodal powder particle space captured via μCT with modest resolution [7]. Mask R-CNN combines both an object detection and an object segmentation network into one. The network is composed of three components: the backbone, the head and the mask prediction branch. The backbone is the component that does feature extraction. In the implementation used in the chapter, the backbone is a Feature Pyramid Network using Resnet 101 architecture [136]. Feature Pyramid Network(FPN) is a feature extractor with length scale built into it. From Figure 4.9, information takes a vertical and downward path in the network. As the image is being passed at each level, the larger features are extracted at each step. On the way down, lower-resolution features are combined with increasingly higher resolution feature maps. At each step, the resulting feature map is sent to a Region Proposal Network(RPN) who tries to detect and place the object at each length scale. The RPN is a sliding window object detector. At each sliding box location, the RPN tries to predict if an object is present and with which anchor is it associated with. An anchor is a box that represents the region where the object is contained within at a specific scale. Anchors can vary in size and aspect ratio. Therefore, to contain all cases, a single sliding window can have multiple anchors associated with it; an illustration of this is captured in Figure 4.8. The FPN is trained such that anchors with 0.7 overlaps with a ground truth label are assigned a true positive (TP) label. Anchors with fewer than 0.3 overlaps with the ground truth are assigned a true negative (TN) label.

Before being fed to the head, the region of interest (ROI) for each feature maps are resized and aligned through an action called ROIAlign. This is to ensure size consistency and avoid quantization errors caused by the downsampling in the FPN. Quantization occurs happens because the pixels of the feature maps, the ROI and the image do not align. Afterward, bounding box detection and classification is performed on each ROI. In parallel, the ROI is fed to a segmentation neural network that also independently tries to classify the object. During the inference, the bounding box are culled using a Non-max suppression algorithm. The segmentation is only done on the leftover bounding box. The implementation of Mask-RCNN used in this study is used for Instance Segmentation. Therefore, each pixel is not uniquely labeled (i.e., a pixel can belong to multiple objects). Consequently, in this study, if a pixel belongs to many objects (particles in this case), the pixel will be assigned to the object with the highest score. Also, the implementation used only supports 2D image analysis. More recent implementation of Mask-RCNN are capable of doing proper Panoptic Segmentation and operating on 3D data [137]. Consequently, object (particle) detection can be deployed directly in 3D, with the associated challenges in terms of data annotation and computation time.

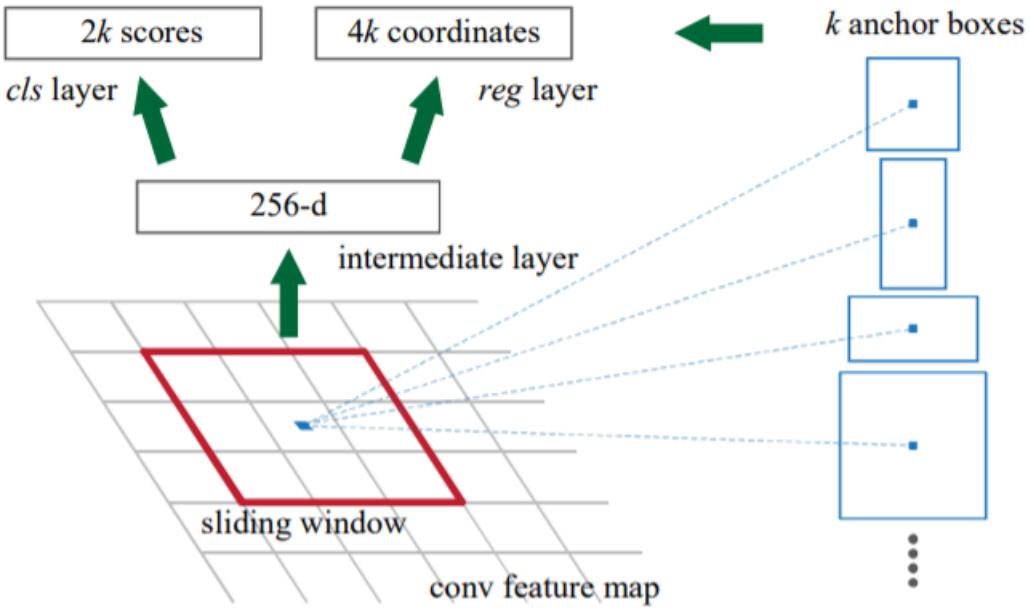

Figure 4.8: Feature Pyramid Network (FPN) anchors [8]

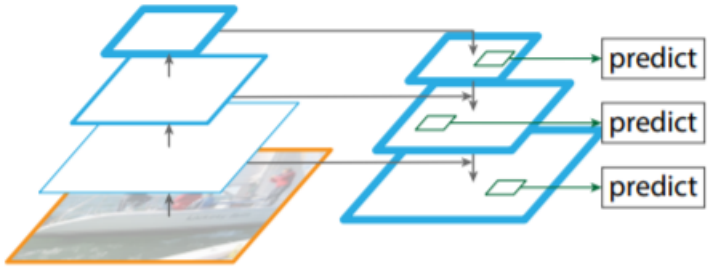

Figure 4.9: Feature Pyramid Network (FPN) with input image at the bottom [9]

4.3 Materials and Methods

4.3.1 Experimental Plan

Cylinders were printed using the Exone M-Flex using the same Bimodal feedstock and print settings as in Section 3.4. The cylinder was scanned in a Zeiss Xradia μCT Scanner, with the data acquisition and reconstruction described in Section 3.4.3. For the training dataset, fifteen 2D images were randomly sampled from the Bimodal parts μCT scans acquired as described in Chapter 3. For the test dataset, nine 2D images were used. The images are square with sizes of 768 pixels and 640 pixels. The images were manually labeled using the platform Supervisely [138]. An example of a labeled image is shown in the appendix B.

4.3.2 Particle Segmentation via Watershed Segmentation Technique

Curvature based segmentation defined by Atta-Fosu et al. was used in this study [132]. As stated previously, the particles used in this study were not circular and often had internal pores. This meant that traditional peak finding is not appropriate. Peaks in non-circular or particles with holes are not single points. Besides, with limited resolution, the delimitation between particles are not always clear. This creates even challenge for peak finding as a contact point between particles will create a saddle point. Given a proper threshold on the distance transform, erroneous peaks can be filtered out. Unfortunately, for this methodology, the choice threshold can be fairly arbitrary and difficult to choose. This is why a curvature-based watershed was chosen. For 3D case, the curvature is defined as follows:

$$k_M = \frac{f_{uu}(1+f_v^2+f_w^2)+f_{vv}(1+f_u^2+f_w^2)+f_{ww}(1+f_u^2+f_v^2)-2(f_uf_vf_{uv}+f_uf_wf_{uw}+f_vf_wf_{vw})}{\sqrt{1+f_u^2+f_v^2+f_w^2}} \tag{4.14}$$

Where f is a discrete grayscale image. With $i \in \{u, v, w\}$, f_i and f_{ii} are its first and second derivative respectively in the u, v or w coordinate direction. Additionally, the image is first denoised by a Gaussian filter, then thresholded using the Otsu thresholding technique. The peak finding is done on the mean curvature of the image. A peak (Ct) is a pixel where the curvature is greater than 0. To separate the peaks and remove noise,

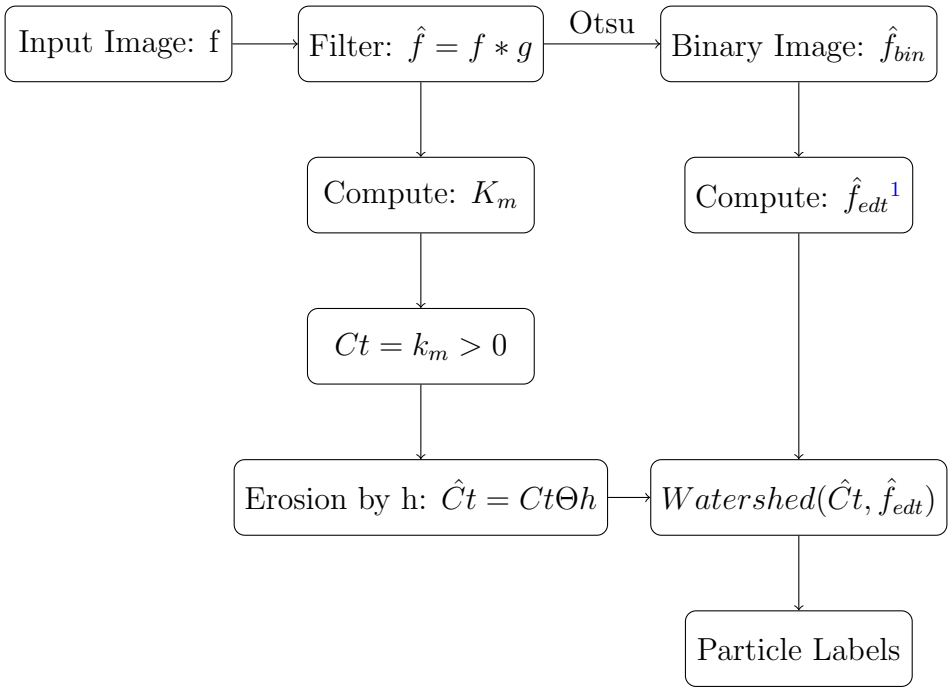

Figure 4.10: Watershed segmentation workflow

a binary erosion is performed on Ct before being fed to the watershed algorithm. The complete workflow is shown in Figure 4.10.

With the training dataset, tuning the filter and erosion size is done using the library Optuna [139]. In order to accelerate the tuning process, during optimization the Panoptic segmentation metric is substituted with the Adapted Rand Error [140]. Rand adapted error is an F-score between the Precision and Recall. But the difference with the panoptic quality is the definition of the Precision and Recall. Precision is the probability of two pixels belong to the same object given they belong to the same object in the prediction. Recall is the probability two pixels belong to the object given they belong to the same object in the ground truth. This metric is optimistic since it does not perform the filtering step done in SQ component of Panoptic segmentation.

4.3.3 Particle Segmentation via Mask-RCNN Technique

The training of a Neural Networks, large quantities of training data are required. Consequently, in order to bolster the quantity of data available during training phase, the following data augmentations are applied on the annotated images (fig. B.2):

1. Affine Rotation : 90, 180, 270
2. Horizontal and Vertical Flipping
3. Speckle Noise
4. Gaussian Blur
5. Downsampling
6. Contrast Adjustment

The neural network was trained for 50 epochs while leveraging transfer learning using weights trained on the COCO dataset [141].

4.4 Results and Discussion

4.4.1 Particle Segmentation Performance Evaluation via Panoptic Segmentation Results

Table 4.1 and 4.2 presents the performance of both curvature based watershed and Mask-RCNN. Additionally, a sample image with the ground truth, watershed segmentation and Mask-RCNN prediction is shown in the figure 4.11. Performance is divided into three categories: Panoptic Quality (PQ), Segmentation Quality (SQ) and Recognition Quality (RQ). SQ denotes the quality of the pixel classification. RQ is the performance of the algorithm in detecting each particle instance. PQ is the product of both RQ and SQ. Furthermore, performance is accessed for each object type (Particle and Background).

Table 4.1: Mask RCNN Segmentation Results

	PQ	SQ	RQ
All	50.8	69.3	74.0
Particle	34.3	71.3	48.1
Background	67.3	67.3	100

Table 4.2: Curvature watershed segmentation results

	PQ	SQ	RQ
All	41.1	67.0	63.3
Particle	18.8	70.7	26.6
Background	63.4	63.4	100

Since there's only one background, the RQ for it is 100%. From the results, we notice the area where Mask-RCNN shines over watershed segmentation is recognition quality (RQ). From the previous section, it was determined that Otsu segmentation is sufficient to obtain bulk density metrics. Therefore, it is no surprise that watershed is more than adequate at segregating void and solid phase. The main weakness of watershed segmentation is its sensitivity to noise. Noise will create spurious peaks which leads to over-segmentation. Unfortunately, the more aggressive the denoising algorithm, the more the edges are blended. The solution would be to gather higher quality data. Unfortunately, this increased the cost of data acquisition. Therefore, it is up to the researcher to balance the trade off. Since the Mask-RCNN needs labeled data, one may argue that the increased cost of data acquisition

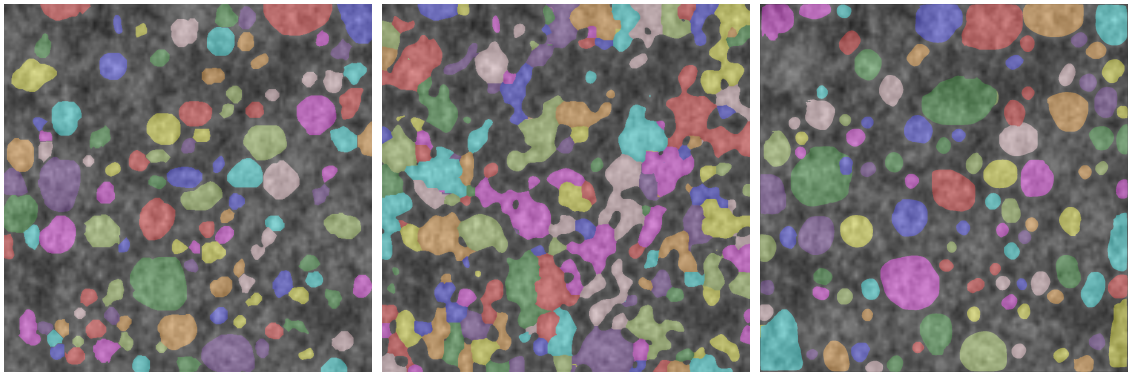

(a) Ground Truth (b) Watershed Prediction (c) Mask RCNN Prediction

Figure 4.11: Sample prediction and ground truth

is shifted towards the cost of labeling. Regrettably, Mask-RCNN is still not robust enough for extracting the metric listed in Section 4.2.1. Also, the current implementation of Mask-RCNN only supports 2D images. Future work will be done using more modern Mask-RCNN. Furthermore, the performance of the either Mask-RCNN and Watershed is still not quantified for 3D data. Further research is needed to investigate the most optimum method to acquiring labeled 3D image. Even labeling 2D image is a time-consuming process.

4.5 Summary and Outcomes

In conclusion, Mask-RCNN is a promising avenue to particle detection for noisy low-resolution CT Scan, with a higher performance than a Watershed Technique. It achieved similar segmentation performance (71.3%) with watershed segmentation but with twice the detection performance (48.1%). The end goal is measuring particle segregation. More work is needed in order to extend Mask-RCNN to 3D images and acquiring labeled data for the 3D case.

Chapter 5

Bayesian Multi-Objective Process Optimization of SS316L

5.1 Background

In a typical manufacturing setting, a manufactured product needs to achieve multiple quality metrics. Most work in literature only focuses on optimizing one quality metrics. Furthermore, the range and number of varied process parameters are restricted. This section proposes the use of Bayesian multi-objective process optimization. The methodology proposed in this chapter handles the full range of process parameter available in Binder Jetting additive manufacturing (BJAM).

The traditional way of performing process optimization is to perform a factorial experiment. The factorial experiment has been shown to be more efficient and converge faster to the optimal settings compared to manual one at a time experiment [142]. A full factorial design of experiments (DOE) is set up such that only one factor is varied at a time between the high- and low-level settings. In combination with an Analysis of Variance (ANOVA), this DOE can separate out the parameter interaction effects from the main effects. Unfortunately, for a large number of factors, the number of experiments needed increases exponentially. An alternative is to use a folded or fractional DOE instead. In the folded DOE method, only a subset of parameters combination are used. The main disadvantage of folded DOE is that the interaction effects are confounded. Consequently, interaction effects will be hidden inside the effect of lower order interaction or even the main effect. Folded DOE comes in many flavors; the main difference between them is the complexity of the confounding and which factors are confounded. The fractional DOE approach was

used in BJAM previously by Chen and Zhao, Shrestha and Manogharan, Jimenez et al. [34, 36, 61].

In process optimization, another approach is to use Taguchi optimization. This was done for BJAM by Chen and Zhao, Shrestha and Manogharan [34, 36]. Taguchi method optimizes process parameters through minimizing a loss function. The loss function is the Signal/Noise (SN) ratio (Eq. 5.1).

$$SN = -10\log(\frac{\overline{y}^2}{\sigma^2}) \tag{5.1}$$

The loss functions are chosen as to maximize, to minimize, or to keep within range the quality metric of interest. Although widely used in the industry, the Taguchi method has received heavy criticism in the statistical community [143]. One criticism is the use of orthogonal DOE ignores interaction effects. Hunter shows that the presence of a single two-factor interaction can create a mirage response in other parameters [144]. Also, the use of the loss function as Eq. 5.1 is misleading [143] because it can be minimized by either maximizing $\overline{y}$ or minimizing σ. This is problematic, since minimizing variance is among the primary goals of the Taguchi method. Furthermore, the method is inefficient because it does not take advantage of sequential experimentation. Taguchi optimization relies on a single large one-shot experiment, therefore any failure or invalid assumption can jeopardize the whole process. For highly uncertain experiments, it is better to start with small batches incrementally.

An alternative method for process optimization is the response surface method (RSM) [145]. In RSM, a model is fitted on the data. The goal of the model is mapping the relationship between the inputs and output(s), determine the relevance of each input parameters and assist in the search for a global optimum. Typically, the model is in the form of a polynomial. With the assumption of a polynomial model, it is possible to find an optimal DOE that minimizes the number of samples and the variance in the model. Furthermore, the data can be collected incrementally. Once the model is fitted, the search for the optimal parameters is done using a gradient descent optimization algorithm.

A form of the RSM method was used by Jimenez et al. [61]. The authors fitted a Gaussian Process Regression (GPR) to model porosity for alumina powder in BJAM. A Gaussian Process (GP) is a non-parametric model. Nonparametric implies a potentially infinite number of parameters. The Gaussian Process, when using the squared exponential kernel, is equivalent to fitting a linear model with an infinite number of basis functions [146]. The use of a GPR as a response surface comes from Design and Analysis of Computer Experiment (DACE) [147]. The goal of DACE is to model the response of a computer model. Typically, the computer model of interest is extremely computationally

intensive. Consequently, DACE attempts to characterize and optimize the model with the least amount of runs. The GPR is used as a surrogate for the expensive computer model. Since computer programs are deterministic in DACE, randomization and blocking are not useful. Maximum space exploration is the goal, therefore the DOE is typically generated through random sampling such as Latin hypercube sampling (LHS) or quasi Monte Carlo (QMC) sampling [147]. The following work by Aboutaleb et al., Mondal et al., Tapia et al. uses this workflow to optimize the parameters of Selective Laser Melting Additive Manufacturing. A feature of a GPR is the variance is quantified at each point. Hence, optimization algorithm takes advantage of this by either sampling area with high variance (exploration) or local minimum areas with low variance (acquisition). This method is known as Bayesian Optimization (BO). BO is typically used in Machine Learning (ML) for optimizing performance of machine learning models[151].

With the rise of the Industry 4.0, the method is starting to be used in AM such as the papers listed previously [148, 149, 61, 150]. Furthermore, Bayesian Optimization is also used in Design for Additive Manufacturing (DfAM) as well [152, 153]. Additionally, Sharpe et al. use BO to optimize Lattice Structure design [153]. While Xiong et al. propose BO for exploring and optimize the design of AM parts[152]. The listed process parameters papers only optimize one quality metrics at a time [148, 149, 61, 150]. Therefore, a multi-objective optimization methodology is presented in this chapter. To the best of the author's knowledge explicit multi-objective optimization has not been tried in literature for Binder Jetting. For additive manufacturing, only the following work by Aboutaleb et al. has attempted this so far [154].

5.2 Experimental method

Materials and Method

In this study, parts are printed using SS316L powder with a Bimodal size distribution. The first powder (316-L5520) is sourced from North American Hoganas (Niagara Falls, NY), with a batch certificate analysis stating that the sieved 50th percentile of the powder size distribution (D50) is roughly 71 μm. The second powder (SS316L) is sourced from Renishaw (Staffordshire, UK) with a D50 of $36.04 \pm 0.87 \mu m$. the two powders were mixed at a ratio of 15% Renishaw powder with 75% Hoganas powder. More detail about the material system and powder can be found in section 3.4. As opposed to chapter 3, the powder were not sieved.

All parts were printed using the Exone M-Flex system (Exone, PA, US) using a custom

single piston reduced build bed. Additionally, a proprietary binder (BA005, Exone, Pa, USA) was used. The binder is approximately 80% water, $2-20\%$ ethynedial and $2-20\%$ 2-butoxyethanol. Furthermore, eight samples were printed per batch. Each sample is a cube with dimensions 20x15x10 mm. Afterward, the samples were cured in an oven at 180 °C for 12 h. Also, the produced parts were measured for porosity using ISO 5013 [155] and dimension deviation (Eq. 5.2). The ISO 5017 measurement method is described in section 3.4.3. Additionally, print duration was recorded.

$$\Delta d = |d_{\text{real}} - d_{\text{nominal}}| \tag{5.2}$$

Given that print duration is correlated with printing cost, it was added in the optimization as a surrogate for monetary cost. Moreover, the input parameters were normalized between 0 and 1. Additionally, the output values were standardized. This was done to help the fitting of the GPR.

Latin Hypercube Sampling

Latin Hypercube Sampling (LHS) is a space filling random sampling technique. The goal is to randomly populate a search space without redundant entries. In the absences of previous knowledge, the existence of a global optimum is assumed to be equally likely everywhere. Furthermore, if only a small subset of the input parameters have an effect on the model, then random sampling is more efficient than a grid search for optimization [10]. This is because in a grid search, parameter variation involving non-active parameters while keeping others constant do not add more information. This is shown in the figure 5.1.

Unfortunately, in a pure random sampling scheme, not every iteration is efficient due to repeated sampling of the same parameters. Additionally, maximum space filling is not guaranteed either [156]. Two solutions to this are the Latin Hypercube Sampling (LHS) and the quasi Monte Carlo sampling [147]. First developed by McKay et al., LHS divides the cumulative distribution function into strata from which a uniform random number is drawn from each stratum. This ensures diversity in the number sampled but also a wide coverage of the search space and avoids repeated sampling of the same values. In literature, this technique is often cited as more efficient than pure random sampling [156]. Alternatively, Quasi Monte Carlo (QMC) generates random number using low-discrepancy number sequences such as the Sobol, Halton or Niedierreter sequence [10]. In the work by Bergstra and Bengio and Singhee and Rutenbar, they found Sobol QMC to be more efficient at finding the optimal parameters than LHS [10, 158]. Unfortunately when

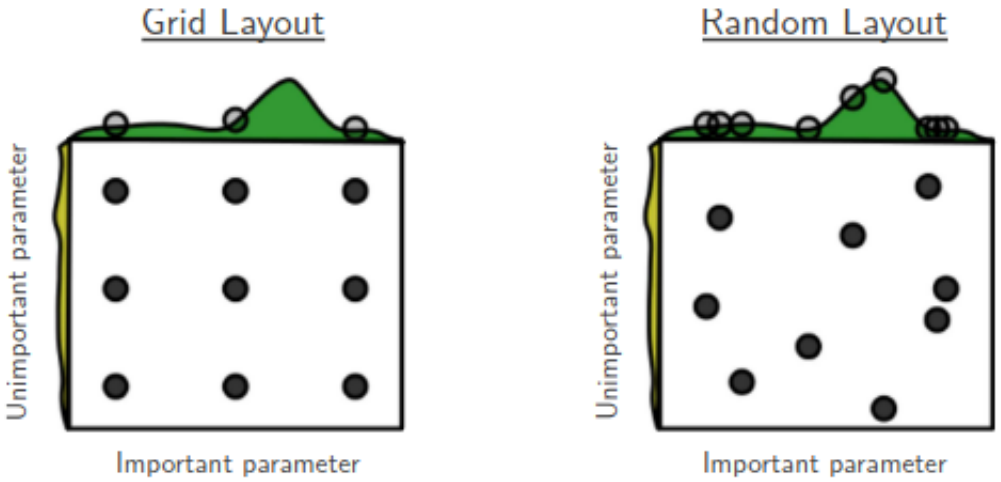

Figure 5.1: Given an unknown function $f(x, y) = g(x) + h(y) \approx g(x)$, $g(x)$ and $h(y)$ shown in green and yellow respectively. Using 9 trials, a grid search does not effectively sample the search space x. [10]

searching a wide area, in Binder Jetting, not every combination of parameters will lead to a successful print. It is possible many experimental trials will result in print failure. Therefore, a Latin Hypercube with enforced correlation is used in this study instead [159]. The chosen correlations are based on experience using the machine. This ensures invalid combination of parameters set are not sampled as often. The LHS can be modified as to add other constraints such as sampling only center point or maximizing geometric distance or minimizing correlation [156]. In the works by Deutsch and Deutsch, the correlated LHS is described as a Latin Hypercube Sampling with Multidimensional Uniformity (LHSMDU). The LHSMDU is implemented and integrated into the library pyDOE2 [160]. The pseudo-

code is as follows:

Input : N: number of factor, L: number of samples, Σ: Covariance Matrix
Output: H: Latin Hypercube Design
$\mathsf{M} \leftarrow 5$;
$\mathsf{R} \leftarrow \texttt{SampleUniformDist}(\mathsf{N} \times \mathsf{ML})$;
$\mathsf{AvgDist} \leftarrow \emptyset$;
while $i < \mathsf{ML} - \mathsf{N}$ **do**
  foreach $r \in \mathsf{R}$ **do**
    $D \leftarrow \texttt{ComputeEuclideanDistance}(r, \mathsf{R} \setminus r)$;
    $\mathsf{AvgDist} \leftarrow \mathsf{AvgDist} \cup \texttt{Mean}(\texttt{Sort}(D)[0:2])$;
    $i \leftarrow i + 1$;
  end
  $\mathsf{AvgDist} \leftarrow \mathsf{AvgDist} \setminus \texttt{Min}(\mathsf{AvgDist})$;
  $\mathsf{R} \leftarrow \mathsf{R} \setminus \texttt{ArgMin}(\mathsf{AvgDist})$;
  $i \leftarrow i - 1$;
end
$P \leftarrow \texttt{GaussianProbDensity}(R)$;
$K \leftarrow \texttt{CholeskyDecomposition}(\Sigma)$;
$\mathsf{H} \leftarrow \texttt{GaussianCumProbDensity}(KP)$;

Algorithm 1: LHSMDU

The covariance matrix used in this chapter is shown in the Table C.1. Using LHSMDU, a 10 samples DOE is generated for the experiment in this chapter.

5.2.1 Surrogate Modeling

The goal of surrogate modeling is to replace an expensive model with a cheaper alternative. The surrogate model of choice is to use a Gaussian Process (GP, also known as Kriging). The main feature of the Gaussian Process Regression is its flexibility and quantification of uncertainty. For optimization the following workflow is used:

Gaussian Process Regression

To understand a Gaussian Process Regression, the first concept to explain is the Multivariate Normal Distribution. In this chapter, the term Gaussian and Normal are used interchangeably as they refer to the same distribution. A random variable X follows a Normal distribution if the probability distribution can be fully described by its means (μ) and

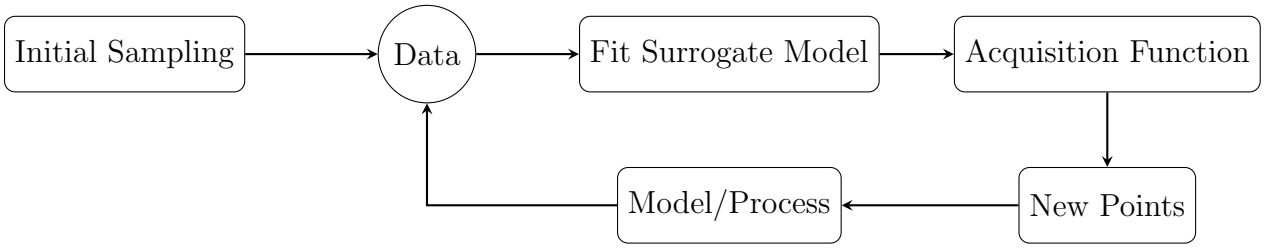

Figure 5.2: Surrogate Modelling Optimization Workflow

covariance ($\text{cov}(X, X) = \Sigma$). The probability density function of a Normal distribution is defined in eq. 5.3.

$$P(X) = \frac{1}{(2\pi)^{d/2}\Sigma^{1/2}} \exp(-\frac{1}{2}(X-\mu)^T\Sigma^{-1}(X-\mu)) \tag{5.3}$$

$$X = \begin{bmatrix} X_1 \\ X_2 \\ . \\ . \\ X_d \end{bmatrix} \tag{5.4}$$

For a multivariate normal distribution, X and μ are vectors of d length. Σ is the covariance matrix of size $d \times d$ where the diagonal entries are the variance σ_i of the $i-th$ random variable of X. The off-diagonal entries σ_{ij} with $i \neq j$ represents the correlation between the $i-th$ and $j-th$ random variables of X. The Multivariate Normal distribution has the following property. Given two jointly distributed random variable X and Y, it is possible to analytically compute the individual (Marginalization) and conditional (Conditioning) probability of X and Y.

$$\begin{bmatrix} X \\ Y \end{bmatrix} \sim N\left(\begin{bmatrix} \mu_x \\ \mu_y \end{bmatrix}, \begin{bmatrix} K_{xx} & k_{xy} \\ k_{yx} & k_{yy} \end{bmatrix}\right) \tag{5.5}$$

Marginalization

$$P(Y) = \int P(Y|X)P(X)dx = \frac{1}{\sqrt{2\pi}(K_{yy})^{1/2}} \exp(-\frac{1}{2}(y-\mu_y)^T K_{yy}^{-1}(y-\mu_y)) \tag{5.6}$$

$$P(X) = \int P(X|Y)P(Y)dy = \frac{1}{\sqrt{2\pi}(K_{xx})^{1/2}} \exp(-\frac{1}{2}(x-\mu_x)^T K_{xx}^{-1}(x-\mu_x)) \tag{5.7}$$

The main consequence of marginalization is given a joint probability. Finding the probability of each component is as simple as taking the entries inside the matrix in eq. 5.5. The opposite is true as well, given two independent Gaussian probability distributions, it is possible to determine their joint probability. Conditioning can be interpreted as taking a slice of the multivariate distribution in one direction. For eq. 5.8, this means computing the probability of X at different value of Y.

Conditioning

$$X|Y \sim N(\mu_x + K_{xy}K_{yy}^{-1}(Y - \mu_y), K_{xx} - K_{xy}K_{yy}^{-1}K_{yx}) \tag{5.8}$$

$$Y|X \sim N(\mu_y + K_{yx}K_{xx}^{-1}(X - \mu_X), K_{yy} - K_{yx}K_{xx}^{-1}K_{xy}) \tag{5.9}$$

A Gaussian Process describes a wide variety of functions by assuming each output of the function $f(x)$ is a multivariate random variable. $f(x)$ is generated by a normal distribution with a mean $m(x)$ and covariance $k(x, x')$ (Eq. 5.10). The function m and k takes input the location x. The main assumption of the Gaussian process is each output are spatially dependent. Therefore, observing $f(x_{i-1})$ will give information about $f(x_i)$. The function k is often known as the kernel. k models the spatial dependence of each point x. The choice of m and k functions defines the richness of function being defined. The mean function can be set to 0, constant value or a Linear Function. Possible choice for the covariance can be Squared Exponential, Periodic or Linear. A more exhaustive list of possible mean and covariance functions can be found in the thesis of Duvenaud [161]. Furthermore, the different kernels can be combined together as well [161]. In this study, following the example of Tapia et al., Sharpe et al., Mondal et al., Duvenaud [150, 153, 149, 161], a single Matern 52 ($\nu = 5/2$) covariance function is used (Eq. 5.11). The Matern kernel is a general case of the Squared Exponential kernel[146]. The Matern kernel becomes the Squared Exponential kernel when $\nu = \infty$.

$$f(x) \sim N(m(x), k(x, x')) \tag{5.10}$$

$$k(x, x') = \sigma^2(1 + \frac{\sqrt{5}(x - x')}{l} + \frac{5(x - x')^2}{3l^2}) \exp(-\frac{\sqrt{5}(x - x')}{l}) \tag{5.11}$$

Here, l is a hyper-parameter which controls the area effect of each data point. Moreover, σ is the variance observed for each entry x, and k is a stationary kernel if it only depends on the distance between x and x'. For a straight line, Fig. 5.3 shows the possible function that can be sampled from Eq. 5.10.

For longer function and different kernel, the following function can be obtained from the GP (Fig. 5.4).

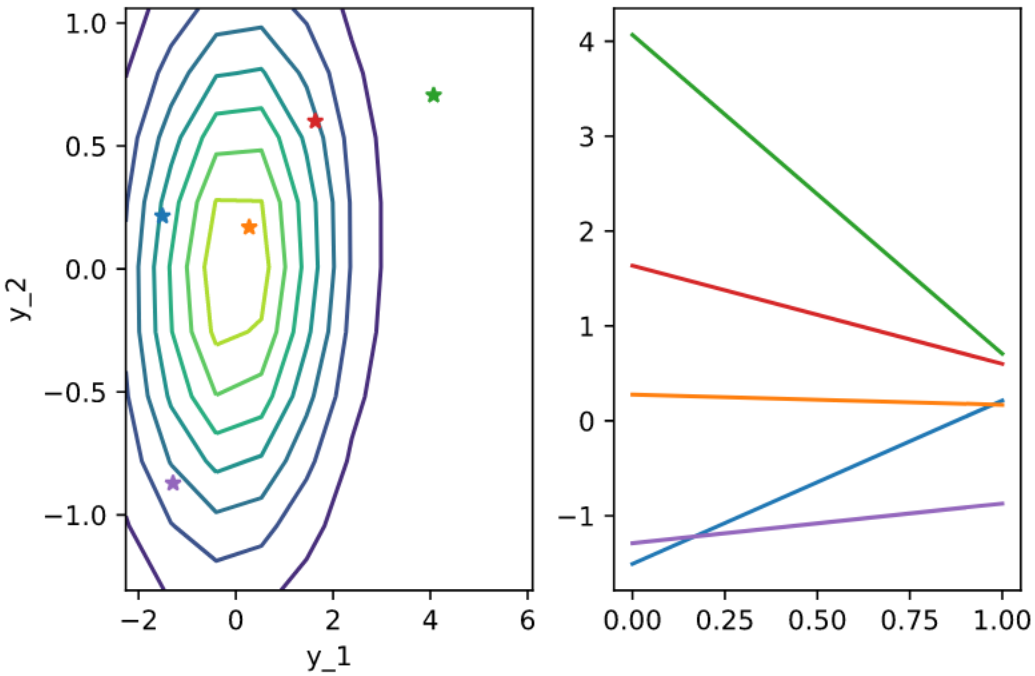

Figure 5.3: Possible sampled Function for two samples

As shown, in Figure 5.4, a GP can generate an infinite set of possible functions. Out of these generated functions, only a few of them can represent the data. Using the outcome Y, each possible function needs to be weighted until only a few remain. This can be done through conditioning. Given a training set of N training X and Y, from the Bayesian theorem, the regression task is to fit a model that maximizes the Posterior probability ($P(X|Y)$) as described below.

$$\text{Posterior} = \frac{\text{likelihood} \times \text{prior}}{\text{marginal likelihood}} \tag{5.12}$$

$$P(X|Y) = \frac{P(Y|X)P(X)}{P(Y)} \tag{5.13}$$

In real-world scenario, observation of Y is never perfect. Therefore, a noise parameter is added to the model. For simplicity, the noise can be assumed to be normally distributed

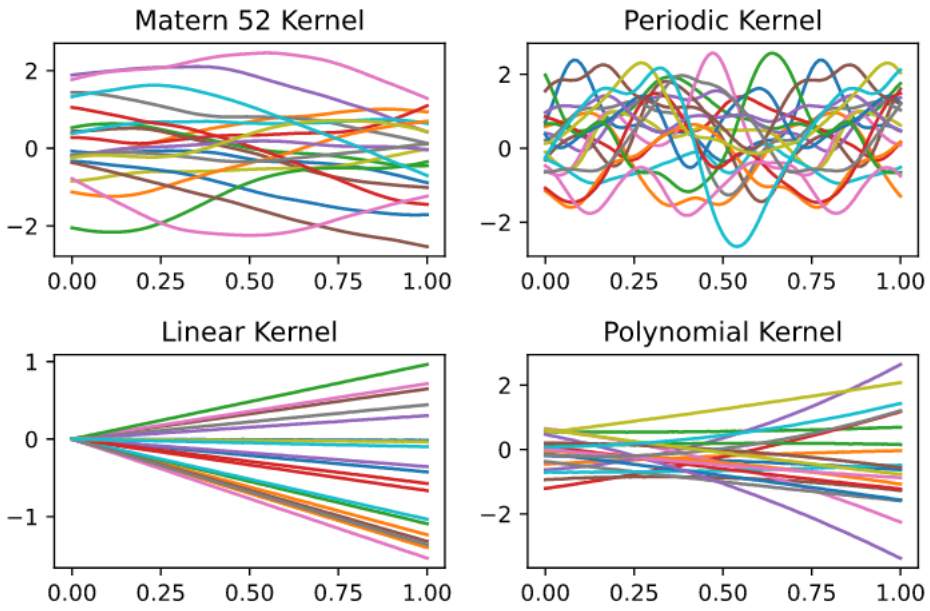

Figure 5.4: Different function realization using different kernels and a zero mean

with zero mean and variance σ_ϵ.

$$Y = f(x) + \epsilon \tag{5.14}$$

$$\epsilon \sim N(0, \sigma_\epsilon) \tag{5.15}$$

Using the marginalization property of the Gaussian, the joint probability of the model $f(x)$ and output Y can be written as:

$$\begin{bmatrix} f(X) \\ Y \end{bmatrix} \sim N(0, \begin{bmatrix} k(X,X) & k(f(X),Y) \\ k(f(X),Y) & k(X,X) + \sigma_\epsilon I \end{bmatrix} \tag{5.16}$$

For mathematical simplicity, both $f(X)$ and Y are assumed to be centered around zero. Using the conditioning property of the Gaussian, it is possible to compute the posterior directly.

$$\begin{aligned} f(X)|Y \sim N(k(f(X),Y)^T \cdot (k(X,X) + \sigma_\epsilon)^{-1} \cdot Y, \\ k(X,X) - k(f(X),Y) \cdot (k(X,X) + \sigma_\epsilon^2)^{-1} \cdot k(Y, f(X))) \end{aligned} \tag{5.17}$$

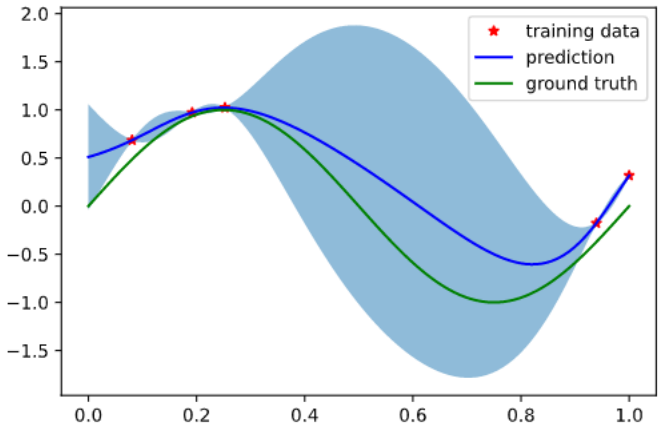

Figure 5.5: GP Posterior

By extension, for predicting Y^* at unknown location X^* given training data X and Y, it is possible to compute the posterior analytically as well.

$$\begin{aligned} Y^*|Y, X, X^* \sim N(k(X^*, X)^T(k(X, X) + \sigma_\epsilon^2 I)^{-1}Y, \\ k(X^*, X^*) - k(X^*, X)^T(k(X, X) + \sigma_\epsilon^2 I)^{-1}k(X^*, X)) \end{aligned} \tag{5.18}$$

The consequence of being able to compute uncertainty at unknown location is shown in the Figure 5.5. The uncertainty of the model is displayed in the light blue area. Uncertainty increases as the distance to the training data increases. Explained in the next section, Bayesian optimization takes advantage of this property.

5.2.2 Multi-Objective Optimization

The goal of an optimization problem is to minimize or maximize a metric generated by an arbitrary function F. For single objective optimization, given a data point X and response $Y = \{y_1, ..., y_n\}$, A Gaussian process model is fitted $\hat{f}$ with output $\hat{Y}$. The acquisition function aims at rewarding both finding the optimum, but also exploring the design space. This work uses the Expected Improvement function[162]. The next sampling point $x_{n+1} \in X$ is determined as follows:

$$x_{n+1} = \underset{x}{\text{argmax}}(E[I(x)]) \tag{5.19}$$

$E[I(x)]$ is the expectation improvement function (EI).

$$E[I(x)] = E[\max(\hat{f}_{\texttt{Min}} - \hat{Y}, 0)] \tag{5.20}$$

Here, $f_{\texttt{Min}}$ is the best output from the surrogate model so far. In this study, the EI function is computed using a Monte Carlo approach. Therefore, the outputs $\hat{Y}$ are sampled randomly from the model. For the Gaussian process regression, it is possible to compute the EI analytically as well [162]. For noisy data, the best point $f_{\texttt{Min}}$ is not always known. Correspondingly, the expectation improvement function is modified as follows [163]:

$$E[I(x)] = E[\max(\texttt{Min}(\hat{f}(x_{n+1})) - \texttt{Min}(\hat{f}(x)), 0)] \tag{5.21}$$

The main difference is now both the output of the surrogate model and the best output are sampled from the posterior of the surrogate model (M).

$$(\hat{f}(x_{n+1}), \hat{f}(x)) \sim M(x_{n+1}, x) \tag{5.22}$$

For multi-objective optimization, the main challenge is determining the global optimum for all metrics of interest. In multi-objective optimization, the path to the global optimum of each objective can conflict with each other. Therefore performing the optimization, involves dealing with the various trade-offs and finding a set of Pareto efficient data points. A data point is considered Pareto efficient if no change can be made to improve the performance of all metrics. Pareto points are not unique. Therefore, a set of Pareto Efficient point is called the Pareto Front. One method to perform multi-objective optimization is to turn the problem into a single objective problem. The objective metrics are summed together using weights. The weights, if chosen, symbolize the users opinion on the importance of each metric. On the other hand, if choosing the weights is impossible, the alternative is to use the ParEGO algorithm [164]. ParEGO scalarizes the objectives using an Augmented Chebyshev Function:

$$Y_{\text{cost}} = \max(w_j * Y_j) + \alpha * \sum_{j=1}^{J} w_j * Y_j \tag{5.23}$$

The term $\max(w_j * Y_j)$ penalizes outliers and the linear term penalizes situation where not every metric improves (Weak Pareto optimality). w_j are randomly sampled weights satisfying the following property $\sum_{j=1} w_j = 1$. α is set to 0.05 . Furthermore, the outputs Y_j are normalized between 0 and 1. ParEGO was shown to be relatively resistant to noise [165].

5.2.3 Model Selection and Feature Selection

Feature Selection and Sensitivity Analysis(SA) are two interrelated fields that differ only in their goals. The goal of sensitivity analysis is to measure the response of the system with regards to its input to understand the system [166]. While, the goal of feature selection is to assert the response of the system with the purpose of removing spurious variables in the input [167]. In sensitivity analysis, the sensitivity is quantified through the use of an index. While in feature selection, the sensitivity is quantified in terms of performance. In practice, sensitivity analysis can also be used for parameter selection [147, 168]. But the interpretation of the sensitivity index needs to be done with special care.

Removing parameters helps alleviate the issue known as the "curse of dimensionality". The curse dimensionality is the problem when the dimension of the problem grows, the quantity of data needed to represent the problem grows exponentially [169].

Feature Selection comes in three flavors: Filter, Wrapper and Embedded method [167]. Filters measure correlation between the input and the output from the data. Examples of correlation metrics are the Pearson correlation, clustering algorithms like k-nearest neighbor search. Wrapper method fits the data sequentially on a subset of the input dimension. Each fitted models are compared to each other while maximizing performance and reducing the number of features. Examples of Wrapper methods are the Sequential Forward Selection (SFS) and Sequential Backward Selection (SBS). In SFS, features are added sequentially to improve performance while in SBS the opposite happens. The wrapper method is performed multiple time using cross validation. Cross validation is a sampling procedure where the data is randomly split into a test and train set k times. Cross validation ensures the train and test datasets are independent of each other. This is to prevent overfitting and measure generalizations potential [170]. In the Embedded method, the feature selection is part of training process through its inclusion in the loss function. Examples of embedded method is the Ridge regression where the loss function penalizes errors but also the number of model parameters [167].

In sensitivity analysis, the methods rely on having an accurate model and modifying the inputs to the model. Sensitivity analysis comes in two flavors, the Elementary Effects Method and the Variance-based methods [166]. The elementary effect(EE) method increase each input dimension one at a time to measure the response. A typical EE method is the Morris Method. While in the Variance based method, the method uses variance decomposition to measure the sensitivity of each input. The main variance based method is the Sobol indices (eq. 5.24) [166]. Sobol indices are the preferred method of measuring Sensitivity if the model is computationally light [166]. Sobol indices are a general case of

ANOVA where the variance is decomposed and assigned to each parameter.

$$S_i = \frac{V_i}{V(Y)} \tag{5.24}$$

Here, S_i is the Sobol indices of parameter i. The numerator of Eq. 5.24 is the variance due to factor i and the denominator is the total variance of the output. The interaction Sobol index ($S_{i,\dots,j}$) can be computed as well. The total Sobol index is the sum of the first-order index and all its interaction indices. A more in-depth explanation and derivation of the Sobol index can be found in section C.2. The main assumption in sensitivity analysis is each input dimension are independent. Correlated input can bias the results of sensitivity analysis [166].

In this section, the feature selection and sensitivity analysis come with a few caveats. For proper space filling using Latin Hypercube, Jones et al. suggests using $11d - 1$ sample locations with d being the amount of input parameters [162]. Unfortunately, due to time and physical constraints, only 10 batches were done in this study. Furthermore, the initial Latin Hypercube used in this work has implicit correlation built into it. This creates bias in the estimation of the sensitivity index [166]. For a pair of correlated parameters, the sensitivity for one parameter is overestimated while the other one is underestimated. Also, the current sensitivity analysis was conducted using the mean response of the model. Model uncertainty is not propagated to the index. Therefore, the sensitivity indices might be biased. Gratiet et al. shows a few method to account for model errors in the sensitivity [171]. Consequently, the result given by this section should be taken with a grain of salt.

In this study, the Sobol indices will be used to measure the responsiveness of the model. Also, an exhaustive parameter selection search optimizing Mean Squared Error is done. In exhaustive parameter search, all combinations of parameters are tried.

5.3 Results and Discussion

Unfortunately, not all trials in this experiment were successful. Batch 8 failed due to insufficient powder coverage therefore porosity was not quantified. However, the dimensions for batch 8 was measured. The Latin Hypercube DOE used in this experiment is shown in the Table 5.1. Additionally, two optimization runs were performed using the settings in the table 5.2. The results of all runs are displayed in the figure 5.6, 5.7 and 5.8.

Furthermore, the symbol $*$ and $\triangledown$ denote batches 11 and 12 respectively in the figure 5.6, 5.7 and 5.8. The results are shown in table form as well in the Appendix C. The

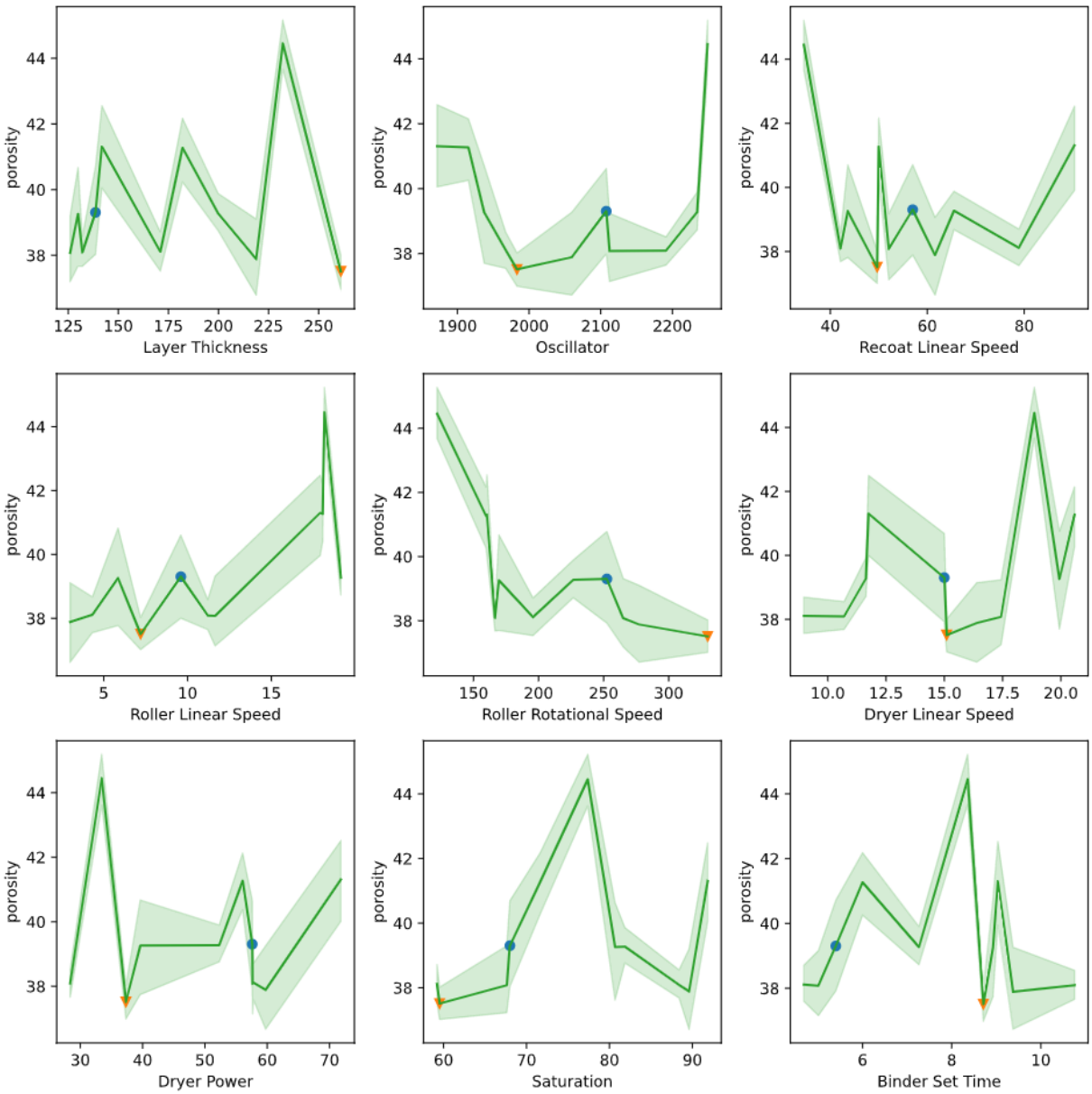

Figure 5.6: Porosity Response to Input. $*$: batch 11, $\triangledown$: batch 12

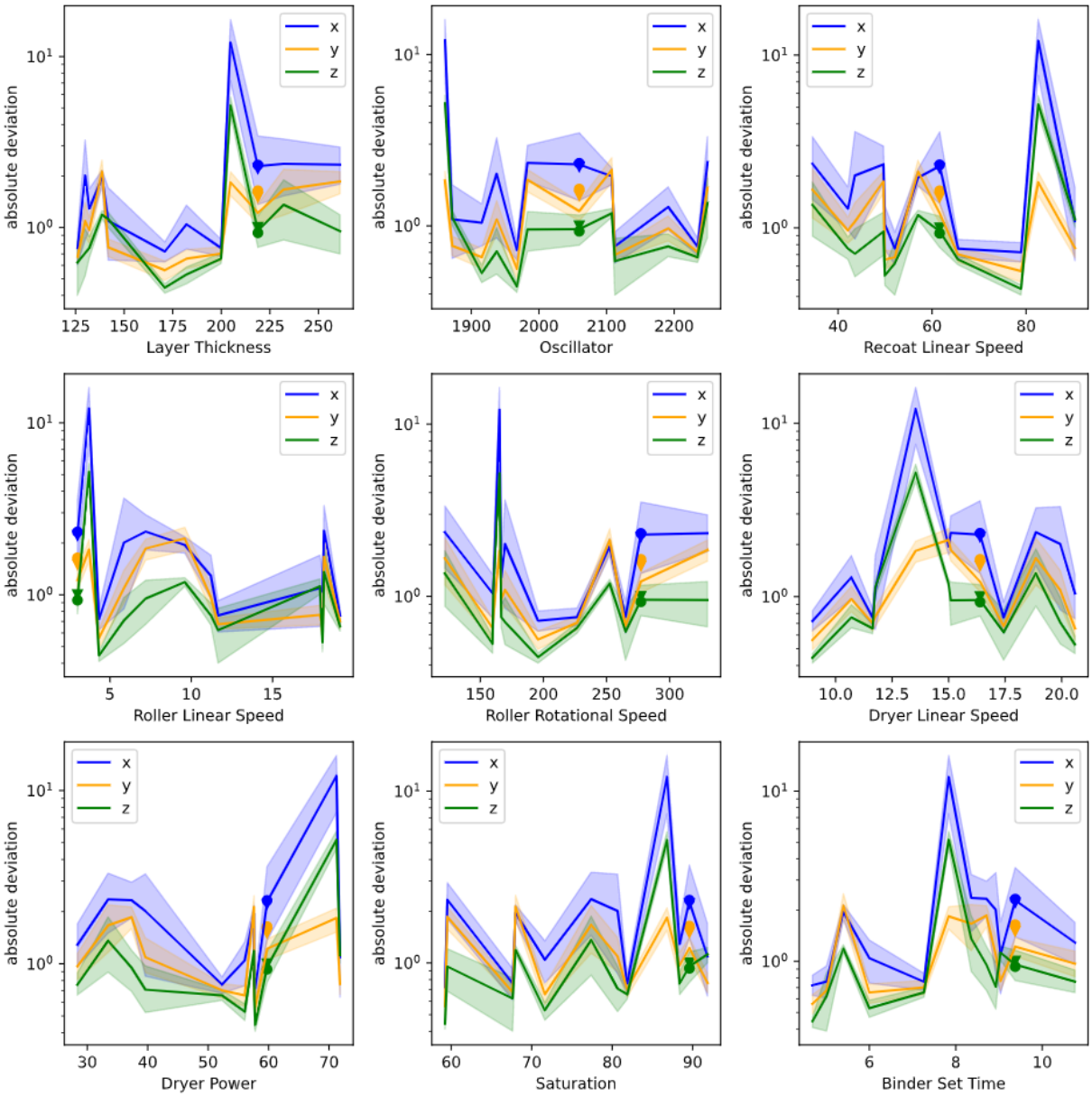

Figure 5.7: Dimension Deviation Response to Input. $*$: batch 11, $\triangledown$: batch 12

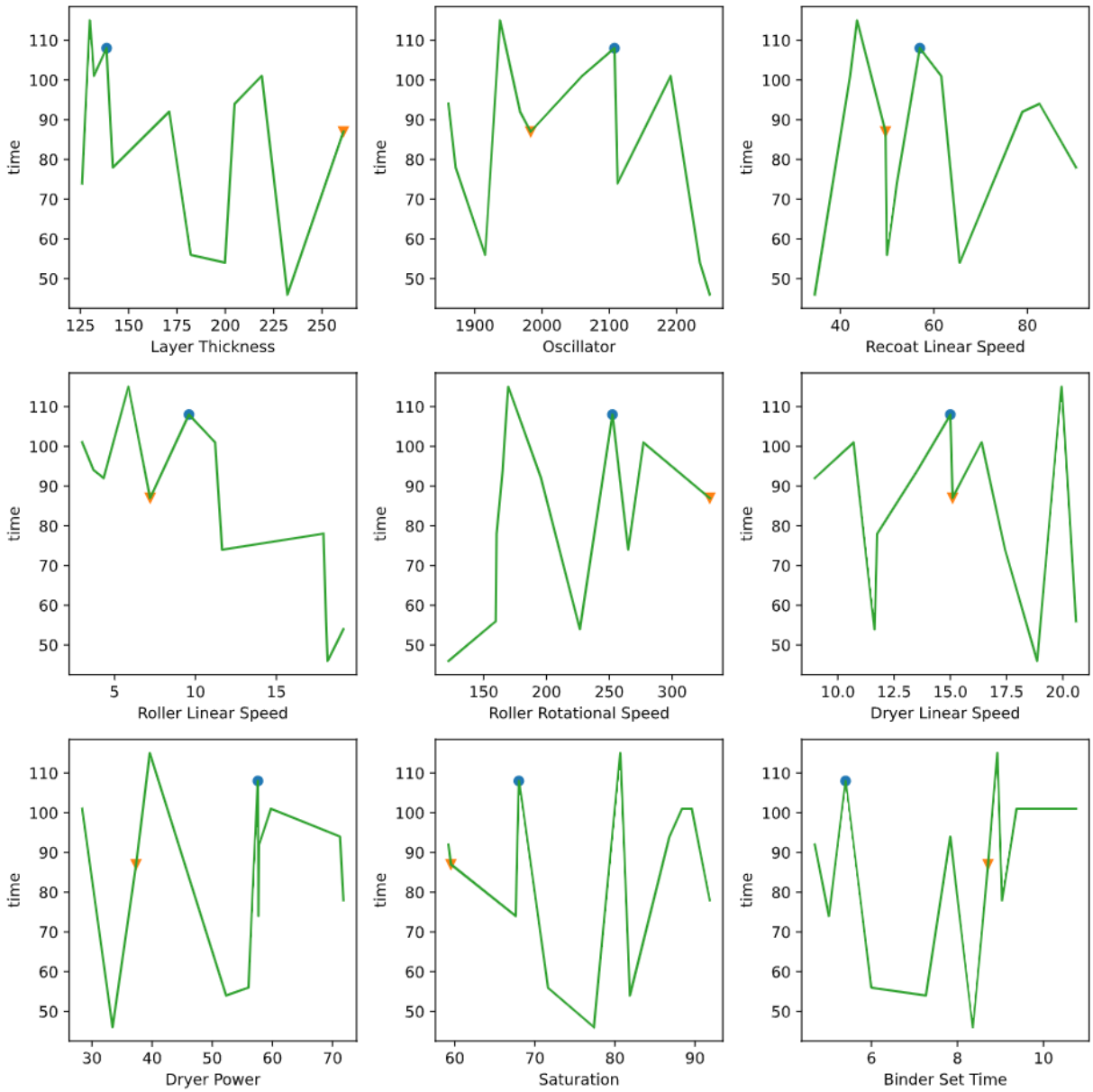

Figure 5.8: Print Duration Response to Input. $*$: batch 11, $\triangledown$: batch 12

Table 5.1: LHS DOE

batch	layer thickness	oscillator	recoat speed	roller speed	roller rpm	drying speed	drying powder	saturation	binder set time
1	171.0	1967.3	78.9	4.3	195.7	9.0	57.8	59.2	4.7
2	218.8	2059.6	61.6	3.0	277.3	16.4	59.7	89.6	9.4
3	129.9	1937.5	43.6	5.9	169.6	19.9	39.6	80.7	8.9
4	141.8	1871.7	90.4	17.9	160.3	11.8	71.8	91.8	9.0
5	126.0	2112.3	52.1	11.6	265.1	17.4	57.7	67.6	5.0
6	182.1	1915.4	50.0	18.1	159.7	20.6	56.1	71.6	6.0
7	232.1	2249.2	34.5	18.2	122.0	18.9	33.4	77.4	8.4
8	204.8	1861.0	82.6	3.7	165.2	13.5	71.2	86.8	7.8
9	132.0	2191.1	42.1	11.2	166.6	10.7	28.4	88.4	10.8
10	199.8	2232.5	65.6	19.1	226.7	11.6	52.3	81.9	7.3

Table 5.2: Two optimization run

batch	layer thickness	oscillator	recoat speed	roller speed	roller rpm	drying speed	drying powder	saturation	binder set time
11	138.6	2107.7	57.0	9.6	252.5	15.0	57.6	68.0	5.4
12	261.09	1983.21	49.66	7.2	329.96	15.1	37.32	59.52	8.71

optimization was successful in minimizing porosity, but dimensional deviation and print time were not minimized. In fig. 5.9, 5.10 and 5.11, a leave one out cross validation (LOOCV) was performed. The predicted versus real value is plotted. For a perfect model, the data should follow a straight line. For porosity and dimension, the Gaussian process represents the data relatively well except for edge cases. On the other hand, for time, the Gaussian process fails to generalize for batches with print time below 70 and 100 minutes. Although, the current performance is not impressive. The algorithm will propose a new trial point with each new data point incorporated into the model. Therefore, more experiments are likely needed to find the true optimum. Five future trials proposed by the algorithm are shown in the Table C.5 and C.6.

The mean squared error for the LOOCV is shown in Table 5.3. Although the average MSE is relatively low, the standard deviation of the error is high. This indicates the model generalizes poorly. As mentioned previously, the model for the dimension and porosity fails at predicting edge cases. These edge cases can either be outliers or are caused by noise. If they are outliers, they can be either filtered out or their impact can be lessened through the use of Robust Regression such as the Student-T process [172] or Random Forest model [173]. If the edge case is caused by noise. Fitting can be improved by modeling the noise separately such as in the Response Surface Method [145].

For SA, the Satelli's sampling scheme [2], implemented in SAlib [174], was used to compute the Sobol indices. Results are shown in the Table 5.4 (describing porosity outcomes), Table 5.5 (describing geometric fidelity in x-direction outcome), Table 5.6 (describing geometric fidelity in y-direction outcomes), Table 5.7 (describing geometric fidelity in

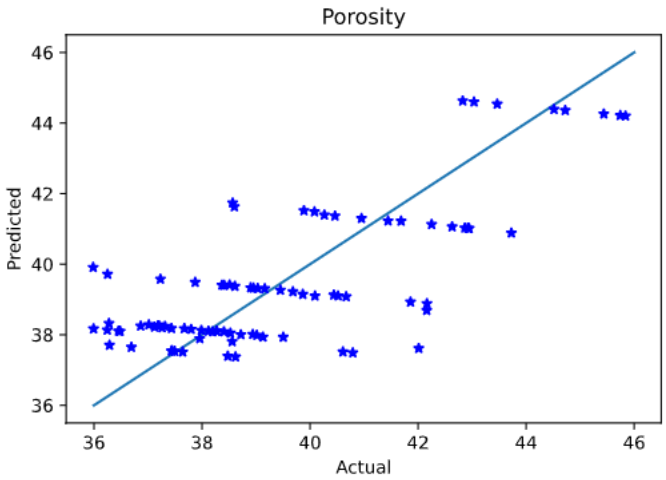

Figure 5.9: Porosity Fit

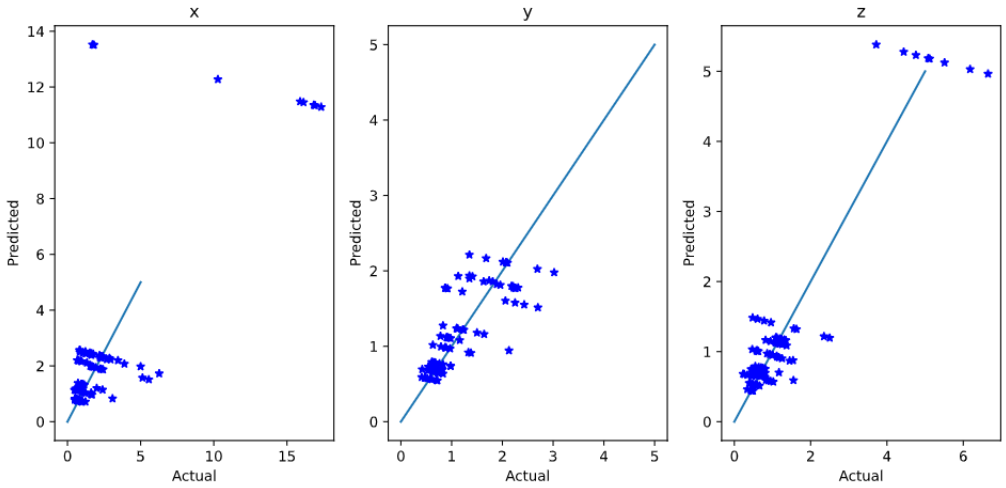

Figure 5.10: Dimension Fit

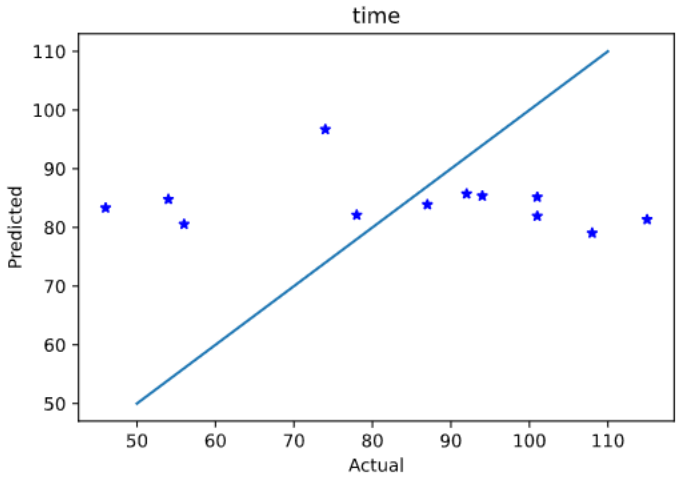

Figure 5.11: Time Fit

Table 5.3: leave one out cross validation : MSE

model	mean	std
porosity	0.43	0.62
dimension x	0.41	1.54
dimension y	0.38	0.71
dimension z	0.12	0.29
time	1.02	0.94

Table 5.4: GPR Sobol Indices Porosity

Parameters	Total	Total Conf.	First Order	First Order Conf.
layer thickness	0.15	0.01	0.0003	0.010
Oscillator	0.09	0.01	0.004	0.007
recoat speed	0.17	0.02	0.006	0.012
roller speed	0.44	0.03	0.267	0.019
roller rotation	0.46	0.04	0.210	0.021
drying speed	0.19	0.02	0.030	0.010
drying power	0.10	0.01	0.002	0.007
saturation	0.07	0.01	0.001	0.006
binder set time	0.07	0.01	0.003	0.006

Table 5.5: GPR Sobol Indices Dimension X

Parameters	Total	Total Conf.	First Order	First Order Conf.
layer thickness	0.11	0.01	0.035	0.007
Oscillator	0.12	0.02	0.031	0.008
recoat speed	0.25	0.03	0.079	0.018
roller speed	0.56	0.05	0.187	0.022
roller rotation	0.23	0.03	0.030	0.012
drying speed	0.06	0.01	-0.002	0.006
drying power	0.26	0.03	0.058	0.013
saturation	0.27	0.04	0.033	0.010
binder set time	0.11	0.02	0.007	0.008

z-direction outcome), and Table 5.8(describing time outcomes). For all metrics, the first order sensitivity indices are very low and the confidence interval high. This is probably due to the low sample number compared to dimension and the low predictive power of the model. Therefore, the first order and interaction indices are not used. For ranking, the total sensitivity index is used instead. A parameter is noncontributing if the total sensitivity is $<< 1$ [175]. Unfortunately, none of the total sensitivities are close to zero. For porosity, the dominating factors are the roller linear speed and roller rotation. This mirrors the finding of Rishmawi et al., Haeri et al. where the roller was found to help compaction. But on the other hand, layer thickness did not register a strong sensitivity.

For the dimensional accuracy in the x direction, the dominant index is the roller linear speed. This is understandable as the x direction is in the roller movement direction. In

Table 5.6: GPR Sobol Indices Dimension Y

Parameters	Total	Total Conf.	First Order	First Order Conf.
layer thickness	0.08	0.01	0.009	0.008
Oscillator	0.07	0.01	0.000	0.007
recoat speed	0.09	0.01	0.000	0.009
roller speed	0.25	0.02	0.072	0.012
roller rotation	0.07	0.01	0.001	0.007
drying speed	0.82	0.04	0.433	0.026
drying power	0.09	0.01	-0.006	0.007
saturation	0.10	0.01	0.006	0.008
binder set time	0.12	0.01	0.004	0.012

Table 5.7: GPR Sobol Indices Dimension Z

Parameters	Total	Total Conf.	First Order	First Order Conf.
layer thickness	0.10	0.01	0.022	0.008
Oscillator	0.12	0.02	0.024	0.008
recoat speed	0.31	0.04	0.118	0.022
roller speed	0.43	0.05	0.107	0.019
roller rotation	0.27	0.04	0.039	0.013
drying speed	0.08	0.01	0.003	0.006
drying power	0.30	0.03	0.083	0.015
saturation	0.29	0.05	0.040	0.013
binder set time	0.11	0.02	0.005	0.006

the Y direction, the dominant Sobol index is the drying speed. This partially follows the conclusion of Chen and Zhao. In the Z direction, drying speed was also found to have a dominant effect on dimensional accuracy [34]. Unfortunately, this was not the case in our model. The sensitivity indices are roughly equally split among recoat linear speed, roller speed, roller rotation, drying power and saturation. This could be interpreted as the result of a high coupling between those parameters.

For time, the dominant index for time is the roller linear speed. This is surprising since one would expect layer thickness to also play an important role as well.

From the feature selection result, the best parameter subset for porosity is roller rotation. This is contrasted with the Sobol indices where roller linear speed and roller rotational speed have a high impact on porosity. As for time, the best parameter subset

Table 5.8: GPR Sobol Indices time

Parameters	Total	Total Conf.	First Order	First Order Conf.
layer thickness	0.08	0.00	0.031	0.007
Oscillator	0.05	0.00	0.003	0.005
recoat speed	0.06	0.00	0.003	0.006
roller speed	0.91	0.03	0.670	0.021
roller rotation	0.06	0.00	0.000	0.006
drying speed	0.05	0.00	0.005	0.007
drying power	0.04	0.00	0.003	0.005
saturation	0.04	0.00	-0.003	0.005
binder set time	0.06	0.00	0.000	0.007

Table 5.9: Feature Selection

Model	Best Subset	MSE
porosity	roller rotation	0.52
dimension	N/A	N/A
time	Oscillator, Roller Speed, Saturation	0.30

was the combination of the oscillator, roller speed and saturation. This is different from the Sobol indices where only roller speed had high sensitivity. Unfortunately, the parameter selection failed for the dimension model due to numerical issues.

5.4 Summary and Outcomes

In summary, Bayesian Optimization for SS316L was performed in this chapter. Given the large number of parameters present in AM, Bayesian Optimization is an attractive option for optimizing process parameters. From previous literature, with the spread of ML knowledge, it is indeed becoming more popular. Also, a multi-objective optimization was performed. Porosity was optimized to 37.5%. Printing time was kept low at 87 min. Unfortunately, print dimensional errors were still relatively high. Although not every metric was optimized, the algorithm enables the user to search continuously for the global optimum. Therefore, with further experimentation, a Pareto efficient set of parameters will be eventually found. Additionally, further work can be done to improve the fitness of the model through the mitigation of noise and outliers. Besides, in the RSM method, the variance of the process can be used as an optimization target as well. This

was not done in this work. Future work will include the variance inside the cost function. Also, the use of a correlated sampling scheme was a stopgap solution to the real problem which is the non-continuous nature of the process space. Since certain combinations of parameters will result in failed print, this creates a discontinuity in the response curve. One possible solution is the use of constrained acquisition function [176]. Another solution is to use hierarchical modeling where the top-level model defines the validity of the print [177]. Although Bayesian Optimization can handle a moderate number of parameters [176], reducing the dimensionality of the problem will accelerate the search for the optimal parameters set. Therefore, further work can be done in clustering the parameters or assert their significance to the process. Furthermore, clustering the parameters into independent parameter set is needed for performing a proper sensitivity analysis. Although sensitivity analysis can be done using dependent input [178, 179]. The procedure is much more complicated. Additionally, the interpretation of the Sobol index is no longer straight forward. Furthermore, if sensitivity analysis is the main goal. For some model such as the polynomial chaos expansion, the sensitivity index can be computed directly from the model [171] at no extra cost.

Chapter 6

Conclusion and Future Work

In this work, an alternative measurement method for Green Binder Jetting density was proposed. Furthermore, a methodology for detecting particle segregation is presented, as a work in progress. Lastly, a process optimization based on Bayesian Optimization was deployed.

In Chapter 3, the ISO 5013 [155] emerged as the preferred for density measurement. Compared to the more commonly used ASTM B962 [67], the procedure is simpler and potentially less prone to error. For future work, more experiments needs to be done to measure the Reproducibility and Repeatability of the method, for the method to be accepted as a standard for green part density measurement. It is recommended that a proper inter-laboratory study needs to be conducted following the procedures of ASTM standard E691 [180]. Although technically equivalent, the estimation of the measurement error was conducted using Bayesian inference as shown in Weaver et al. [105]. The inference was done in this manner as to not mislead readers. In Bayesian inference, the assumption taken during the estimation of the error are explicitly shown in the model. Furthermore, the results are stated using a confidence interval. Given the experiment was conducted within a single lab and with only 2 operators, the error estimate ($\sigma_{gage} : [0.34, 0.38]\%$) is therefore an optimistic one. What's more, during the analysis of the sample, it was noticed the manufactured samples displayed a high level of heterogeneity. This issue will need to be resolved for future work. Moreover, in this chapter, various threshold technique was tried and compared in μCT image analysis. The thresholding techniques that gave the closest value to Archimedes with the smallest variance were Otsu, Isodata and Mean. This finding agrees with Iassonov et al. [90].

In Chapter 4, tools for detecting particle segregation inside Binder Jetting green parts

were developed. Unfortunately, the developed algorithms were not accurate enough for the requirement task, but can still be used a starting point for future work. The goal of the software is to segment and spatially resolve powder particles from micro-computed tomography images. Spatially placing particles will enable the use of statistical metrics for quantifying segregation. Two approaches were used. One is based on watershed segmentation and the other is based on using the Mask-RCNN neural network. To achieve high data acquisition throughput, the images were knowingly acquired in a noisy state. This proved to be an issue as even manual segmentation proved to be difficult. The performance of the watershed algorithm was heavily degraded. Although, not up to the required performance level, the Mask-RCNN proved to be remarkably resilient. Future work will go in improving the performance of Mask-RCNN but also in acquiring micro-tomography data more cheaply. If machine learning techniques are to be used, further work is needed to accelerate the acquisition of ground truth data for training the algorithm.

In Chapter 5, a multi-objective Bayesian Optimization method was used to minimize porosity, dimensional deviation and print duration. The last trial managed to obtain the lowest porosity of 37.51% of the porosity while keeping the print-time low. Unfortunately, the dimensional accuracy was among the lowest. This shows the challenge of multi-objective optimization where multiple metrics can conflict with each other. Therefore, the optimization involves making trade-offs. For the Bayesian optimization, a Gaussian process regression (GPR) is fitted. A sensitivity analysis and a feature selection was conducted to quantify the importance of each input parameters. Although, the sensitivity results and feature selection partially follows previous work. The results should be interpreted with caution. Since the chapter made explicit use of a correlated design of experiments and the number of sampled point is low, the results of the sensitivity analysis and feature selection can be biased. The choice of correlated sampling was driven by the desire to avoid sampling invalid combination of parameters. Therefore, future work can be done in investigating constrained Bayesian optimization [176] or hierarchical modeling. Moreover, the use of the GPR assumes the data is relatively smooth, stationary and the noise is evenly distributed. When those assumptions are no longer true, more exotic model can be used such as Heteroskedatic GPR [181] (spatially dependent noise), Student-t process [182] (large number of outliers) or Deep Gaussian Process [183] (non-stationary response).

References

[1] E. Wheat, M. Vlasea, J. Hinebaugh, and C. Metcalfe, "Sinter structure analysis of titanium structures fabricated via binder jetting additive manufacturing," *Materials & Design*, vol. 156, pp. 167–183, 2018.

[2] I. M. Sobol, "Global sensitivity indices for nonlinear mathematical models and their monte carlo estimates," *Mathematics and computers in simulation*, vol. 55, no. 1-3, pp. 271–280, 2001.

[3] J. L. Hart and P. A. Gremaud, "Robustness of the sobol'indices to marginal distribution uncertainty," *SIAM/ASA Journal on Uncertainty Quantification*, vol. 7, no. 4, pp. 1224–1244, 2019.

[4] A. B. Varotsis, "Introduction to binder jetting 3d printing." [Online]. Available: https://www.3dhubs.com/knowledge-base/introduction-binder-jetting-3d-printing/

[5] P. Tang and V. M. Puri, "Methods for minimizing segregation: A review," *Particulate Science and Technology*, vol. 22, no. 4, pp. 321–337, 2004. [Online]. Available: https://doi.org/10.1080/02726350490501420

[6] A. Kirillov, K. He, R. Girshick, C. Rother, and P. Dollár, "Panoptic segmentation," in *Proceedings of the IEEE conference on computer vision and pattern recognition*, 2019, pp. 9404–9413.

[7] K. He, G. Gkioxari, P. Dollár, and R. Girshick, "Mask r-cnn," in *Proceedings of the IEEE international conference on computer vision*, 2017, pp. 2961–2969.

[8] S. Ren, K. He, R. Girshick, and J. Sun, "Faster r-cnn: Towards real-time object detection with region proposal networks," in *Advances in neural information processing systems*, 2015, pp. 91–99.

[9] T.-Y. Lin, P. Dollár, R. Girshick, K. He, B. Hariharan, and S. Belongie, "Feature pyramid networks for object detection," in *Proceedings of the IEEE conference on computer vision and pattern recognition*, 2017, pp. 2117–2125.

[10] J. Bergstra and Y. Bengio, "Random search for hyper-parameter optimization," *The Journal of Machine Learning Research*, vol. 13, no. 1, pp. 281–305, 2012.

[11] W. Du, X. Ren, C. Ma, and Z. Pei, "Binder jetting additive manufacturing of ceramics: A literature review," in *ASME 2017 International Mechanical Engineering Congress and Exposition*. American Society of Mechanical Engineers Digital Collection, 2017.

[12] X. Lv, F. Ye, L. Cheng, S. Fan, and Y. Liu, "Binder jetting of ceramics: Powders, binders, printing parameters, equipment, and post-treatment," *Ceramics International*, vol. 45, no. 10, pp. 12 609–12 624, 2019.

[13] M. Li, W. Du, A. Elwany, Z. Pei, and C. Ma, "Binder Jetting Additive Manufacturing of Metals: A Literature Review," in *MSEC2019*, Volume 1: Additive Manufacturing; Manufacturing Equipment and Systems; Bio and Sustainable Manufacturing, Jun. 2019, v001T01A033. [Online]. Available: https://doi.org/10.1115/MSEC2019-2994

[14] I. Campbell, O. Diegel, J. Kowen, and T. Wohlers, *Wohlers report 2018: 3D printing and additive manufacturing state of the industry: annual worldwide progress report*. Wohlers Associates, 2018.

[15] "Senvol database." [Online]. Available: http://senvol.com/

[16] I. Gibson, D. W. Rosen, B. Stucker *et al.*, *Additive manufacturing technologies*. Springer, 2014, vol. 17.

[17] I. Gibson, D. Rosen, and B. Stucker, *Binder Jetting*. New York, NY: Springer New York, 2015, pp. 205–218. [Online]. Available: https://doi.org/10.1007/978-1-4939-2113-3_8

[18] T. Wohlers, R. I. Campbell, R. Huff, O. Diegel, and J. Kowen, *Wohlers report 2019: 3D printing and additive manufacturing state of the industry*. Wohlers Associates, 2019.

[19] B. Utela, D. Storti, R. Anderson, and M. Ganter, "A review of process development steps for new material systems in three dimensional printing (3dp)," *Journal of Manufacturing Processes*, vol. 10, no. 2, pp. 96–104, 2008.

[20] M. Upadhyay, T. Sivarupan, and M. El Mansori, "3D printing for rapid sand castingA review," *Journal of Manufacturing Processes*, vol. 29, pp. 211–220, Oct. 2017. [Online]. Available: http://www.sciencedirect.com/science/article/pii/S1526612517301810

[21] J. Goole and K. Amighi, "3d printing in pharmaceutics: A new tool for designing customized drug delivery systems," *International journal of pharmaceutics*, vol. 499, no. 1-2, pp. 376–394, 2016.

[22] M. Ziaee and N. B. Crane, "Binder jetting: A review of process, materials, and methods," *Additive Manufacturing*, vol. 28, pp. 781–801, 2019.

[23] F. Tao, H. Zhang, A. Liu, and A. Y. Nee, "Digital twin in industry: State-of-the-art," *IEEE Transactions on Industrial Informatics*, vol. 15, no. 4, pp. 2405–2415, 2018.

[24] E. M. Sachs, J. S. Haggerty, M. J. Cima, and P. A. Williams, "Three-dimensional printing techniques," Apr. 20 1993, uS Patent 5,204,055.

[25] M. Cima, M. Oliveira, H. Wang, E. Sachs, and R. Holman, "Slurry-based 3dp and fine ceramic components," in *Proceedings of Solid Freeform Fabrication Symposium, Austin, TX*, 2001, pp. 216–223.

[26] A. Mostafaei, E. L. Stevens, E. T. Hughes, S. D. Biery, C. Hilla, and M. Chmielus, "Powder bed binder jet printed alloy 625: Densification, microstructure and mechanical properties," *Materials & Design*, vol. 108, pp. 126–135, 2016.

[27] A. Mostafaei, J. Toman, E. L. Stevens, E. T. Hughes, Y. L. Krimer, and M. Chmielus, "Microstructural evolution and mechanical properties of differently heat-treated binder jet printed samples from gas-and water-atomized alloy 625 powders," *Acta Materialia*, vol. 124, pp. 280–289, 2017.

[28] J. Gonzalez, J. Mireles, Y. Lin, and R. B. Wicker, "Characterization of ceramic components fabricated using binder jetting additive manufacturing technology," *Ceramics International*, vol. 42, no. 9, pp. 10 559–10 564, 2016.

[29] Y. Bai and C. B. Williams, "An exploration of binder jetting of copper," *Rapid Prototyping Journal*, vol. 21, no. 2, pp. 177–185, 2015.

[30] Y. Bai, G. Wagner, and C. B. Williams, "Effect of bimodal powder mixture on powder packing density and sintered density in binder jetting of metals," in *2015 Annual International Solid Freeform Fabrication Symposium*, vol. 62, 2015, pp. 758–771.

[31] A. Kumar, Y. Bai, A. Eklund, and C. B. Williams, "Effects of hot isostatic pressing on copper parts fabricated via binder jetting," *Procedia Manufacturing*, vol. 10, pp. 935 – 944, 2017, 45th SME North American Manufacturing Research Conference, NAMRC 45, LA, USA. [Online]. Available: http://www.sciencedirect.com/science/article/pii/S2351978917302664

[32] A. Curodeau, E. Sachs, and S. Caldarise, "Design and fabrication of cast orthopedic implants with freeform surface textures from 3-d printed ceramic shell," *Journal of Biomedical Materials Research: An Official Journal of The Society for Biomaterials, The Japanese Society for Biomaterials, and The Australian Society for Biomaterials and the Korean Society for Biomaterials*, vol. 53, no. 5, pp. 525–535, 2000.

[33] A. Lauder, M. Cima, E. Sachs, and T. Fan, "Three dimensional printing: surface finish and microstructure of rapid prototyped components," *MRS Online Proceedings Library Archive*, vol. 249, 1991.

[34] H. Chen and Y. F. Zhao, "Process parameters optimization for improving surface quality and manufacturing accuracy of binder jetting additive manufacturing process," *Rapid Prototyping Journal*, vol. 22, no. 3, pp. 527–538, 2016. [Online]. Available: https://doi.org/10.1108/RPJ-11-2014-0149

[35] I. Rishmawi, M. Salarian, and M. Vlasea, "Tailoring green and sintered density of pure iron parts using binder jetting additive manufacturing," *Additive Manufacturing*, vol. 24, pp. 508–520, 2018.

[36] S. Shrestha and G. Manogharan, "Optimization of binder jetting using taguchi method," *Jom*, vol. 69, no. 3, pp. 491–497, 2017.

[37] S. Haeri, Y. Wang, O. Ghita, and J. Sun, "Discrete element simulation and experimental study of powder spreading process in additive manufacturing," *Powder Technology*, vol. 306, pp. 45–54, 2017.

[38] M. Vaezi and C. K. Chua, "Effects of layer thickness and binder saturation level parameters on 3d printing process," *The International Journal of Advanced Manufacturing Technology*, vol. 53, no. 1-4, pp. 275–284, 2011.

[39] Y. Bai, G. Wagner, and C. B. Williams, "Effect of particle size distribution on powder packing and sintering in binder jetting additive manufacturing of metals," *Journal of Manufacturing Science and Engineering*, vol. 139, no. 8, p. 081019, 2017.

[40] B. Jim, "Binder stability and powder/binder interaction in three dimensional printing," Ph.D. dissertation, PhD Thesis, Mech. Eng. MIT 1/95.

[41] H. Miyanaji, S. Zhang, and L. Yang, "A new physics-based model for equilibrium saturation determination in binder jetting additive manufacturing process," *International Journal of Machine Tools and Manufacture*, vol. 124, pp. 1 – 11, 2018. [Online]. Available: http://www.sciencedirect.com/science/article/pii/S0890695517301335

[42] W. A. Gray, "Packing of solid particles," 1968.

[43] S. Torquato, *Random heterogeneous materials: microstructure and macroscopic properties*. Springer Science & Business Media, 2013, vol. 16.

[44] H. Miyanaji, M. Orth, J. M. Akbar, and L. Yang, "Process development for green part printing using binder jetting additive manufacturing," *Frontiers of Mechanical Engineering*, vol. 13, no. 4, pp. 504–512, 2018.

[45] E. S. Almaghariz, B. P. Conner, L. Lenner, R. Gullapalli, G. P. Manogharan, B. Lamoncha, and M. Fang, "Quantifying the Role of Part Design Complexity in Using 3D Sand Printing for Molds and Cores," *International Journal of Metalcasting*, vol. 10, no. 3, pp. 240–252, Jul. 2016. [Online]. Available: https://doi.org/10.1007/s40962-016-0027-5

[46] S. Holland, T. Foster, W. MacNaughtan, and C. Tuck, "Design and characterisation of food grade powders and inks for microstructure control using 3d printing," *Journal of food Engineering*, vol. 220, pp. 12–19, 2018.

[47] J. Rouquerol, D. Avnir, C. Fairbridge, D. Everett, J. Haynes, N. Pernicone, J. Ramsay, K. Sing, and K. Unger, "Recommendations for the characterization of porous solids (technical report)," *Pure and Applied Chemistry*, vol. 66, no. 8, pp. 1739–1758, 1994.

[48] A. International, "Standard for additive manufacturing finished part properties standard specification for titanium alloys via powder bed fusion," 2018.

[49] ——, "Standard test method for density of powder metallurgy (pm) materials containing less than two percent porosity," 2017.

[50] P. Kunchala and K. Kappagantula, "3d printing high density ceramics using binder jetting with nanoparticle densifiers," *Materials Design*, vol. 155, pp. 443

– 450, 2018. [Online]. Available: http://www.sciencedirect.com/science/article/pii/S0264127518304751

[51] D. A. Snelling, C. B. Williams, C. T. Suchicital, and A. P. Druschitz, "Binder jetting advanced ceramics for metal-ceramic composite structures," *The International Journal of Advanced Manufacturing Technology*, vol. 92, no. 1-4, pp. 531–545, 2017.

[52] S. Zhang, H. Miyanaji, L. Yang, A. Ali, and J. Dilip, "An experimental study of ceramic dental porcelain materials using a 3d print (3dp) process," in *Proceeding of Solid Freeform Fabrication (SFF) Symposium*, 2014, pp. 991–1011.

[53] S. M. Gaytan, M. Cadena, M. Aldaz, E. Herderick, F. Medina, and R. Wicker, "Analysis of ferroelectric ceramic fabricated by binder jetting technology," in *Proceedings of Solid Freeform Fabrication Symposium*, 2013, pp. 859–868.

[54] Y. Zhu, Z. Wu, W. D. Hartley, J. M. Sietins, C. B. Williams, and H. Z. Yu, "Unraveling pore evolution in post-processing of binder jetting materials: X-ray computed tomography, computer vision, and machine learning," *Additive Manufacturing*, vol. 34, p. 101183, Aug. 2020. [Online]. Available: http://www.sciencedirect.com/science/article/pii/S2214860420305558

[55] M. Vlasea, E. Toyserkani, and R. Pilliar, "Effect of gray scale binder levels on additive manufacturing of porous scaffolds with heterogeneous properties," *International Journal of Applied Ceramic Technology*, vol. 12, no. 1, pp. 62–70, 2015.

[56] E. Sheydaeian, M. Vlasea, A. Woo, R. Pilliar, E. Hu, and E. Toyserkani, "Effect of glycerol concentrations on the mechanical properties of additive manufactured porous calcium polyphosphate structures for bone substitute applications," *Journal of Biomedical Materials Research Part B: Applied Biomaterials*, vol. 105, no. 4, pp. 828–835, 2017.

[57] M. Castilho, B. Gouveia, I. Pires, J. Rodrigues, and M. Pereira, "The role of shell/core saturation level on the accuracy and mechanical characteristics of porous calcium phosphate models produced by 3dprinting," *Rapid Prototyping Journal*, 2015.

[58] R. Chumnanklang, T. Panyathanmaporn, K. Sitthiseripratip, and J. Suwanprateeb, "3D printing of hydroxyapatite: Effect of binder concentration in pre-coated particle on part strength," *Materials Science and Engineering: C*, vol. 27, no. 4, pp. 914–921, May 2007. [Online]. Available: http://www.sciencedirect.com/science/article/pii/S092849310600378X

[59] J. Suwanprateeb, R. Sanngam, and T. Panyathanmaporn, "Influence of raw powder preparation routes on properties of hydroxyapatite fabricated by 3D printing technique," *Materials Science and Engineering: C*, vol. 30, no. 4, pp. 610–617, May 2010. [Online]. Available: http://www.sciencedirect.com/science/article/pii/S0928493110000329

[60] F. Fei, L. He, B. Zhou, Z. Xu, and X. Song, "Hydrothermal-Assisted Transient Binder Jetting of Ceramics for Achieving High Green Density," *JOM*, vol. 72, no. 3, pp. 1307–1313, Mar. 2020. [Online]. Available: https://doi.org/10.1007/s11837-019-03962-2

[61] E. M. Jimenez, D. Ding, L. Su, A. R. Joshi, A. Singh, B. Reeja-Jayan, and J. Beuth, "Parametric analysis to quantify process input influence on the printed densities of binder jetted alumina ceramics," *Additive Manufacturing*, vol. 30, p. 100864, 2019. [Online]. Available: http://www.sciencedirect.com/science/article/pii/S2214860419307821

[62] A. Winkel, R. Meszaros, S. Reinsch, R. Mller, N. Travitzky, T. Fey, P. Greil, and L. Wondraczek, "Sintering of 3D-Printed Glass/HAp Composites," *Journal of the American Ceramic Society*, vol. 95, no. 11, pp. 3387–3393, Nov. 2012, publisher: John Wiley & Sons, Ltd. [Online]. Available: https://doi.org/10.1111/j.1551-2916.2012.05368.x

[63] U. Gbureck, T. Hlzel, U. Klammert, K. Wrzler, F. Mller, and J. Barralet, "Resorbable Dicalcium Phosphate Bone Substitutes Prepared by 3D Powder Printing," *Advanced Functional Materials*, vol. 17, no. 18, pp. 3940–3945, Dec. 2007, publisher: John Wiley & Sons, Ltd. [Online]. Available: https://doi.org/10.1002/adfm.200700019

[64] J. Moon, J. E. Grau, V. Knezevic, M. J. Cima, and E. M. Sachs, "Ink-Jet Printing of Binders for Ceramic Components," *Journal of the American Ceramic Society*, vol. 85, no. 4, pp. 755–762, Apr. 2002, publisher: John Wiley & Sons, Ltd. [Online]. Available: https://doi.org/10.1111/j.1151-2916.2002.tb00168.x

[65] Y. Wang, K. Wang, X. Li, Q. Wei, W. Chai, S. Wang, Y. Che, T. Lu, and B. Zhang, "3D fabrication and characterization of phosphoric acid scaffold with a HA/-TCP weight ratio of 60:40 for bone tissue engineering applications," *PLOS ONE*, vol. 12, no. 4, p. e0174870, Apr. 2017, publisher: Public Library of Science. [Online]. Available: https://doi.org/10.1371/journal.pone.0174870

[66] Z. Fu, L. Schlier, N. Travitzky, and P. Greil, "Three-dimensional printing of SiSiC lattice truss structures," *Materials Science and Engineering: A*, vol. 560, pp. 851–856, Jan. 2013. [Online]. Available: http://www.sciencedirect.com/science/article/pii/S0921509312014372

[67] A. International, "Standard test methods for density of compacted or sintered powder metallurgy (pm) products using archimedes principle," 2013.

[68] M. Martella, "MatWeb. (Reference And Tools)," *Sensors Magazine*, vol. 19, no. 12, p. 25, Dec. 2002, section: 25. [Online]. Available: https://link.gale.com/apps/doc/A95103090/AONE?u=uniwater&sid=AONE&xid=86514ff8

[69] M. Standard, "Materials standards for pm structural parts," *Metal Powder Industries Federation, Princeton, NJ*, 2007.

[70] A. International, "Astm c373-18-standard test methods for determination of water absorption and associated properties by vacuum method for pressed ceramic tiles and glass tiles and boil method for extruded ceramic tiles and non-tile fired ceramic whiteware products," 2018.

[71] P. Pinot, "Détermination de la porosité de roches calcaires: méthode et incertitude de mesure determining the porosity of limestone: experimental method and uncertainty," *REVUE FRANAISE DE MTROLOGIE*, vol. 37, 2015.

[72] A. International, "Standard test methods for laboratory determination of density (unit weight) of soil specimens." 2009.

[73] C. Kamath, B. El-Dasher, G. F. Gallegos, W. E. King, and A. Sisto, "Density of additively-manufactured, 316l ss parts using laser powder-bed fusion at powers up to 400 w," *The International Journal of Advanced Manufacturing Technology*, vol. 74, no. 1-4, pp. 65–78, 2014.

[74] H. Liang, D. Xie, Y. Mao, J. Shi, C. Wang, L. Shen, and Z. Tian, "The size effect on forming quality of ti–6al–4v solid struts fabricated via laser powder bed fusion," *Metals*, vol. 9, no. 4, p. 416, 2019.

[75] A. B. Spierings, M. Schneider, and R. Eggenberger, "Comparison of density measurement techniques for additive manufactured metallic parts," *Rapid Prototyping Journal*, 2011.

[76] H. Giesche, "Mercury porosimetry: a general (practical) overview," *Particle & particle systems characterization*, vol. 23, no. 1, pp. 9–19, 2006.

[77] C. Chang, "Measuring density and porosity of grain kernels using a gas pycnometer," *Cereal Chem*, vol. 65, no. 1, pp. 13–15, 1988.

[78] J. A. Slotwinski, E. J. Garboczi, P. E. Stutzman, C. F. Ferraris, S. S. Watson, and M. A. Peltz, "Characterization of metal powders used for additive manufacturing," *Journal of research of the National Institute of Standards and Technology*, vol. 119, p. 460, 2014.

[79] K. Aroom, L. Warburton, W. Bentley, and L. Schultheis, "Measuring surface-connected porosity of complete 3d printed structures using a custom pycnometer," *Transactions on Additive Manufacturing Meets Medicine*, vol. 1, no. 1, 2019.

[80] L. De Chiffre, S. Carmignato, J.-P. Kruth, R. Schmitt, and A. Weckenmann, "Industrial applications of computed tomography," *CIRP annals*, vol. 63, no. 2, pp. 655–677, 2014.

[81] B. Gapinski, P. Janicki, L. Marciniak-Podsadna, and M. Jakubowicz, "Application of the computed tomography to control parts made on additive manufacturing process," *Procedia Engineering*, vol. 149, pp. 105 – 121, 2016, international Conference on Manufacturing Engineering and Materials, ICMEM 2016, 6-10 June 2016, Nov Smokovec, Slovakia. [Online]. Available: http://www.sciencedirect.com/science/article/pii/S1877705816311535

[82] A. Obaton, M. Lê, V. Prezza, D. Marlot, P. Delvart, A. Huskic, S. Senck, E. Mahé, and C. Cayron, "Investigation of new volumetric non-destructive techniques to characterise additive manufacturing parts," *Welding in the World*, vol. 62, no. 5, pp. 1049–1057, 2018.

[83] A. Thompson, I. Maskery, and R. K. Leach, "X-ray computed tomography for additive manufacturing: a review," *Measurement Science and Technology*, vol. 27, no. 7, p. 072001, 2016.

[84] F. Natterer, *The mathematics of computerized tomography*. SIAM, 2001.

[85] W. Stiller, "Basics of iterative reconstruction methods in computed tomography: A vendor-independent overview," *European Journal of Radiology*, vol. 109, pp. 147 – 154, 2018. [Online]. Available: http://www.sciencedirect.com/science/article/pii/S0720048X18303747

[86] R. Leach, D. Bourell, S. Carmignato, A. Donmez, N. Senin, and W. Dewulf, "Geometrical metrology for metal additive manufacturing," *CIRP Annals*, vol. 68, no. 2, pp. 677 – 700, 2019. [Online]. Available: http://www.sciencedirect.com/science/article/pii/S0007850619301611

[87] A. du Plessis, P. Sperling, A. Beerlink, L. Tshabalala, S. Hoosain, N. Mathe, and S. G. le Roux, "Standard method for microCT-based additive manufacturing quality control 2: Density measurement," vol. 5, pp. 1117–1123. [Online]. Available: http://www.sciencedirect.com/science/article/pii/S2215016118301481

[88] L. Kong, M. Ostadhassan, C. Li, and N. Tamimi, "Pore characterization of 3d-printed gypsum rocks: a comprehensive approach," vol. 53, no. 7, pp. 5063–5078. [Online]. Available: https://doi.org/10.1007/s10853-017-1953-1

[89] J. A. Slotwinski, E. J. Garboczi, and K. M. Hebenstreit, "Porosity measurements and analysis for metal additive manufacturing process control," *Journal of research of the National Institute of Standards and Technology*, vol. 119, p. 494, 2014.

[90] P. Iassonov, T. Gebrenegus, and M. Tuller, "Segmentation of x-ray computed tomography images of porous materials: A crucial step for characterization and quantitative analysis of pore structures," *Water Resources Research*, vol. 45, no. 9, 2009. [Online]. Available: https://agupubs.onlinelibrary.wiley.com/doi/abs/10.1029/2009WR008087

[91] M. Berthod, Z. Kato, S. Yu, and J. Zerubia, "Bayesian image classification using markov random fields," *Image and Vision Computing*, vol. 14, no. 4, pp. 285 – 295, 1996. [Online]. Available: http://www.sciencedirect.com/science/article/pii/0262885695010726

[92] Wonho Oh and B. Lindquist, "Image thresholding by indicator kriging," *IEEE Transactions on Pattern Analysis and Machine Intelligence*, vol. 21, no. 7, pp. 590–602, 1999.

[93] Y. Q. Feng, B. H. Xu, S. J. Zhang, A. B. Yu, and P. Zulli, "Discrete particle simulation of gas fluidization of particle mixtures," *AIChE Journal*, vol. 50, no. 8, pp. 1713–1728, 2004. [Online]. Available: https://aiche.onlinelibrary.wiley.com/doi/abs/10.1002/aic.10169

[94] T. Ridler, S. Calvard *et al.*, "Picture thresholding using an iterative selection method," *IEEE transactions on Systems, Man and Cybernetics*, vol. 8, no. 8, pp. 630–632, 1978.

[95] C. Li and P. K.-S. Tam, "An iterative algorithm for minimum cross entropy thresholding," *Pattern recognition letters*, vol. 19, no. 8, pp. 771–776, 1998.

[96] C. A. Glasbey, "An analysis of histogram-based thresholding algorithms," *CVGIP: Graphical models and image processing*, vol. 55, no. 6, pp. 532–537, 1993.

[97] N. Otsu, "A threshold selection method from gray-level histograms," *IEEE transactions on systems, man, and cybernetics*, vol. 9, no. 1, pp. 62–66, 1979.

[98] G. W. Zack, W. E. Rogers, and S. Latt, "Automatic measurement of sister chromatid exchange frequency." *Journal of Histochemistry & Cytochemistry*, vol. 25, no. 7, pp. 741–753, 1977.

[99] J.-C. Yen, F.-J. Chang, and S. Chang, "A new criterion for automatic multilevel thresholding," *IEEE Transactions on Image Processing*, vol. 4, no. 3, pp. 370–378, 1995.

[100] I. Standard, "13322-2 2006 particle size analysis-image analysis methods–part 2," *Dynamic Image Analysis Methods*.

[101] I. Rishmawi, "Binder jetting and heat treatment of ferrous alloys," Master's thesis, University of Waterloo, 2019.

[102] M. Pavan, T. Craeghs, J.-P. Kruth, and W. Dewulf, "Investigating the influence of x-ray ct parameters on porosity measurement of laser sintered pa12 parts using a design-of-experiment approach," *Polymer Testing*, vol. 66, pp. 203 – 212, 2018. [Online]. Available: http://www.sciencedirect.com/science/article/pii/S0142941817316057

[103] B. N. Taylor and C. E. Kuyatt, "Guidelines for evaluating and expressing the uncertainty of nist measurement results," 1994.

[104] R. K. Burdick, C. M. Borror, and D. C. Montgomery, *Design and analysis of gauge R&R studies: making decisions with confidence intervals in random and mixed ANOVA models*. SIAM, 2005.

[105] B. P. Weaver, M. S. Hamada, S. B. Vardeman, and A. G. Wilson, "A Bayesian Approach to the Analysis of Gauge R&R Data," *Quality Engineering*, vol. 24, no. 4, pp. 486–500, Oct. 2012, publisher: Taylor & Francis. [Online]. Available: https://doi.org/10.1080/08982112.2012.702381

[106] A. Gelman and others, "Prior distributions for variance parameters in hierarchical models (comment on article by Browne and Draper)," *Bayesian analysis*, vol. 1, no. 3, pp. 515–534, 2006, publisher: International Society for Bayesian Analysis.

[107] S. Chib and E. Greenberg, "Understanding the metropolis-hastings algorithm," *The american statistician*, vol. 49, no. 4, pp. 327–335, 1995.

[108] J. Salvatier, T. V. Wiecki, and C. Fonnesbeck, "Probabilistic programming in python using pymc3," *PeerJ Computer Science*, vol. 2, p. e55, 2016.

[109] M. D. Hoffman and A. Gelman, "The no-u-turn sampler: adaptively setting path lengths in hamiltonian monte carlo." *J. Mach. Learn. Res.*, vol. 15, no. 1, pp. 1593–1623, 2014.

[110] S. le Roux, A. du Plessis, and C. Clarke, "Microct-based bulk density measurement method for soils," *Journal of the South african institution of civil engineering*, vol. 61, no. 1, pp. 2–9, 2019.

[111] S. Bruns, S. L. S. Stipp, and H. O. Sørensen, "Statistical representative elementary volumes of porous media determined using greyscale analysis of 3d tomograms," *Advances in Water Resources*, vol. 107, pp. 32–42, 2017.

[112] J. Bian, J. H. Siewerdsen, X. Han, E. Y. Sidky, J. L. Prince, C. A. Pelizzari, and X. Pan, "Evaluation of sparse-view reconstruction from flat-panel-detector cone-beam ct," *Physics in Medicine & Biology*, vol. 55, no. 22, p. 6575, 2010.

[113] E. Stevens, S. Schloder, E. Bono, D. Schmidt, and M. Chmielus, "Density variation in binder jetting 3D-printed and sintered Ti-6Al-4V," *Additive Manufacturing*, vol. 22, pp. 746–752, 2018, publisher: Elsevier.

[114] L. Fan, S. Chen, and C. Watson, "Annual review solids mixing," *Industrial & Engineering Chemistry*, vol. 62, no. 7, pp. 53–69, 1970.

[115] S. Chou, C. Liao, and S. Hsiau, "An experimental study on the effect of liquid content and viscosity on particle segregation in a rotating drum," *Powder Technology*, vol. 201, no. 3, pp. 266 – 272, 2010. [Online]. Available: http://www.sciencedirect.com/science/article/pii/S0032591010001890

[116] H. Li and J. J. McCarthy, "Phase diagrams for cohesive particle mixing and segregation," *Phys. Rev. E*, vol. 71, p. 021305, Feb 2005. [Online]. Available: https://link.aps.org/doi/10.1103/PhysRevE.71.021305

[117] N. K. Keller, W. Bai, R. O. Fox, and T. J. Heindel, "Quantifying mixing in 3d binary particulate systems," *Chemical Engineering Science*, vol. 93, pp. 412 – 422, 2013. [Online]. Available: http://www.sciencedirect.com/science/article/pii/S0009250913000961

[118] C.-J. Bae, A. Ramachandran, and J. W. Halloran, "Quantifying particle segregation in sequential layers fabricated by additive manufacturing," *Journal of the European Ceramic Society*, vol. 38, no. 11, pp. 4082 – 4088, 2018. [Online]. Available: http://www.sciencedirect.com/science/article/pii/S0955221918300827

[119] S. Shin and L. Fan, "Characterization of solids mixtures by the discrete fourier transform," *Powder Technology*, vol. 19, no. 2, pp. 137–146, 1978.

[120] Y. Gao, F. Muzzio, and M. Ierapetritou, "Characterization of feeder effects on continuous solid mixing using fourier series analysis," *AIChE Journal*, vol. 57, no. 5, pp. 1144–1153, 2011. [Online]. Available: https://aiche.onlinelibrary.wiley.com/doi/abs/10.1002/aic.12348

[121] P. M. C. Lacey, "Developments in the theory of particle mixing," *Journal of applied chemistry*, vol. 4, no. 5, pp. 257–268, 1954.

[122] H. Zhu, Z. Zhou, R. Yang, and A. Yu, "Discrete particle simulation of particulate systems: A review of major applications and findings," *Chemical Engineering Science*, vol. 63, no. 23, pp. 5728 – 5770, 2008. [Online]. Available: http://www.sciencedirect.com/science/article/pii/S0009250908004168

[123] M. Ashton and F. Valentin, "The mixing of powders and particles in industrial mixers," *Trans. Inst. Chem. Eng.*, vol. 44, no. 5, pp. 166–188, 1966.

[124] Y. Wen, M. Liu, B. Liu, and Y. Shao, "Comparative study on the characterization method of particle mixing index using dem method," *Procedia engineering*, vol. 102, pp. 1630–1642, 2015.

[125] M. Combarros, H. Feise, H. Zetzener, and A. Kwade, "Segregation of particulate solids: Experiments and dem simulations," *Particuology*, vol. 12, pp. 25 – 32, 2014, special issue on conveying and handling of particulate solids Challenges of discrete element simulation, application and calibration. [Online]. Available: http://www.sciencedirect.com/science/article/pii/S1674200113001363

[126] W. Godlieb, S. Gorter, N. G. Deen, and J. Kuipers, "Dem and tfm simulations of solids mixing in a gas-solid fluidized bed," in *Seventh International Conference on*

CFD in the Minerals and Process Industries, CSIRO, Melbourne, Australia, 2009, pp. 9–11.

[127] D. McGlinchey, "Quantifying segregation in heaps: an experimental study," *Powder Technology*, vol. 145, no. 2, pp. 106 – 112, 2004. [Online]. Available: http://www.sciencedirect.com/science/article/pii/S0032591004002669

[128] D. K. Rollins, D. L. Faust, and D. L. Jabas, "A superior approach to indices in determining mixture segregation," *Powder technology*, vol. 84, no. 3, pp. 277–282, 1995.

[129] J. T. Gostick, "Versatile and efficient pore network extraction method using marker-based watershed segmentation," *Physical Review E*, vol. 96, no. 2, p. 023307, 2017.

[130] A. Vagnon, J. Rivière, J. Missiaen, D. Bellet, M. Di Michiel, C. Josserond, and D. Bouvard, "3d statistical analysis of a copper powder sintering observed in situ by synchrotron microtomography," *Acta Materialia*, vol. 56, no. 5, pp. 1084–1093, 2008.

[131] Y. Wang, C. L. Lin, and J. D. Miller, "3d image segmentation for analysis of multisize particles in a packed particle bed," vol. 301, pp. 160 – 168. [Online]. Available: http://www.sciencedirect.com/science/article/pii/S0032591016302339

[132] T. Atta-Fosu, W. Guo, D. Jeter, C. M. Mizutani, N. Stopczynski, and R. Sousa-Neves, "3d clumped cell segmentation using curvature based seeded watershed," vol. 2, no. 4, p. 31, publisher: Multidisciplinary Digital Publishing Institute.

[133] N. Voss, C. Yoshioka, M. Radermacher, C. Potter, and B. Carragher, "Dog picker and tiltpicker: Software tools to facilitate particle selection in single particle electron microscopy," *Journal of Structural Biology*, vol. 166, no. 2, pp. 205 – 213, 2009. [Online]. Available: http://www.sciencedirect.com/science/article/pii/S1047847709000197

[134] H. W. Lin, M. Tegmark, and D. Rolnick, "Why does deep and cheap learning work so well?" *Journal of Statistical Physics*, vol. 168, no. 6, pp. 1223–1247, 2017.

[135] C. Olah, N. Cammarata, L. Schubert, G. Goh, M. Petrov, and S. Carter, "Zoom in: An introduction to circuits," *Distill*, 2020, https://distill.pub/2020/circuits/zoom-in.

[136] W. Abdulla, "Mask r-cnn for object detection and instance segmentation on keras and tensorflow," https://github.com/matterport/Mask_RCNN, 2017.

[137] Y. Wu, A. Kirillov, F. Massa, W.-Y. Lo, and R. Girshick, "Detectron2," https://github.com/facebookresearch/detectron2, 2019.

[138] D. Drozdov, M. Kolomeychenko, and Y. Borisov, "Supervisely," https://github.com/supervisely/supervisely, 2020.

[139] T. Akiba, S. Sano, T. Yanase, T. Ohta, and M. Koyama, "Optuna: A next-generation hyperparameter optimization framework," in *Proceedings of the 25rd ACM SIGKDD International Conference on Knowledge Discovery and Data Mining*, 2019.

[140] S. van der Walt, J. L. Schönberger, J. Nunez-Iglesias, F. Boulogne, J. D. Warner, N. Yager, E. Gouillart, T. Yu, and the scikit-image contributors, "scikit-image: image processing in Python," *PeerJ*, vol. 2, p. e453, 6 2014. [Online]. Available: https://doi.org/10.7717/peerj.453

[141] T.-Y. Lin, M. Maire, S. Belongie, J. Hays, P. Perona, D. Ramanan, P. Dollár, and C. L. Zitnick, "Microsoft coco: Common objects in context," in *European conference on computer vision*. Springer, 2014, pp. 740–755.

[142] D. C. Montgomery, *Design and analysis of experiments*. John wiley & sons, 2017.

[143] J. J. Pignatiello Jr and J. S. Ramberg, "Top ten triumphs and tragedies of genichi taguchi," *Quality Engineering*, vol. 4, no. 2, pp. 211–225, 1991.

[144] J. S. Hunter, "Let's all beware the latin square," *Quality Engineering*, vol. 1, no. 4, pp. 453–465, 1989.

[145] A. I. Khuri and S. Mukhopadhyay, "Response surface methodology," *Wiley Interdisciplinary Reviews: Computational Statistics*, vol. 2, no. 2, pp. 128–149, 2010.

[146] C. K. Williams and C. E. Rasmussen, *Gaussian processes for machine learning*. MIT press Cambridge, MA, 2006, vol. 2, no. 3.

[147] T. J. Santner, B. J. Williams, W. I. Notz, and B. J. Williams, *The design and analysis of computer experiments*. Springer, 2003, vol. 1.

[148] A. M. Aboutaleb, L. Bian, A. Elwany, N. Shamsaei, S. M. Thompson, and G. Tapia, "Accelerated process optimization for laser-based additive manufacturing by leveraging similar prior studies," *IISE Transactions*, vol. 49, no. 1, pp. 31–44, 2017, publisher: Taylor & Francis.

[149] S. Mondal, D. Gwynn, A. Ray, and A. Basak, "Investigation of Melt Pool Geometry Control in Additive Manufacturing Using Hybrid Modeling," *Metals*, vol. 10, no. 5, p. 683, May 2020, publisher: MDPI AG. [Online]. Available: http://dx.doi.org/10.3390/met10050683

[150] G. Tapia, A. Elwany, and H. Sang, "Prediction of porosity in metal-based additive manufacturing using spatial gaussian process models," *Additive Manufacturing*, vol. 12, pp. 282–290, 2016.

[151] J. Snoek, H. Larochelle, and R. P. Adams, "Practical bayesian optimization of machine learning algorithms," in *Advances in neural information processing systems*, 2012, pp. 2951–2959.

[152] Y. Xiong, P. L. T. Duong, D. Wang, S.-I. Park, Q. Ge, N. Raghavan, and D. W. Rosen, "Data-driven design space exploration and exploitation for design for additive manufacturing," *Journal of Mechanical Design*, vol. 141, no. 10, 2019, publisher: American Society of Mechanical Engineers Digital Collection.

[153] C. Sharpe, C. C. Seepersad, S. Watts, and D. Tortorelli, "Design of mechanical metamaterials via constrained bayesian optimization," in *International Design Engineering Technical Conferences and Computers and Information in Engineering Conference*, vol. 51753. American Society of Mechanical Engineers, 2018, p. V02AT03A029.

[154] A. M. Aboutaleb, L. Bian, N. Shamsaei, S. M. Thompson, and P. K. Rao, "Multi-objective process optimization of additive manufacturing: A case study on geometry accuracy optimization," in *Annual International Solid Freeform Fabrication Symposium*, 2016.

[155] I. 5017, "Dense shaped refractory products-determination of bulk density, apparent porosity and true porosity," 1998.

[156] H. Janssen, "Monte-Carlo based uncertainty analysis: Sampling efficiency and sampling convergence," *Reliability Engineering & System Safety*, vol. 109, pp. 123 – 132, 2013. [Online]. Available: http://www.sciencedirect.com/science/article/pii/S0951832012001536

[157] M. D. McKay, R. J. Beckman, and W. J. Conover, "A comparison of three methods for selecting values of input variables in the analysis of output from a computer code," *Technometrics*, vol. 42, no. 1, pp. 55–61, 2000.

[158] A. Singhee and R. A. Rutenbar, "Why quasi-monte carlo is better than monte carlo or latin hypercube sampling for statistical circuit analysis," *IEEE Transactions on Computer-Aided Design of Integrated Circuits and Systems*, vol. 29, no. 11, pp. 1763–1776, 2010.

[159] J. L. Deutsch and C. V. Deutsch, "Latin hypercube sampling with multidimensional uniformity," *Journal of Statistical Planning and Inference*, vol. 142, no. 3, pp. 763 – 772, 2012. [Online]. Available: http://www.sciencedirect.com/science/article/pii/S0378375811003776

[160] M. Baudin, M. Christopoulou, M. Baudin, Y. Collette, J.-M. Martinez, A. D. Lee, R. Sjgren, and D. Svensson, "pydoe2," https://github.com/clicumu/pyDOE2, 2018.

[161] D. Duvenaud, "Automatic model construction with gaussian processes," Ph.D. dissertation, University of Cambridge, 2014.

[162] D. R. Jones, M. Schonlau, and W. J. Welch, "Efficient global optimization of expensive black-box functions," *Journal of Global optimization*, vol. 13, no. 4, pp. 455–492, 1998, publisher: Springer.

[163] B. Letham, B. Karrer, G. Ottoni, E. Bakshy *et al.*, "Constrained bayesian optimization with noisy experiments," *Bayesian Analysis*, vol. 14, no. 2, pp. 495–519, 2019.

[164] J. Knowles, "Parego: a hybrid algorithm with on-line landscape approximation for expensive multiobjective optimization problems," *IEEE Transactions on Evolutionary Computation*, vol. 10, no. 1, pp. 50–66, 2006.

[165] J. Knowles, D. Corne, and A. Reynolds, "Noisy multiobjective optimization on a budget of 250 evaluations," in *International Conference on Evolutionary Multi-Criterion Optimization*. Springer, 2009, pp. 36–50.

[166] A. Saltelli, M. Ratto, T. Andres, F. Campolongo, J. Cariboni, D. Gatelli, M. Saisana, and S. Tarantola, *Global sensitivity analysis: the primer*. John Wiley & Sons, 2008.

[167] G. Chandrashekar and F. Sahin, "A survey on feature selection methods," *40th-year commemorative issue*, vol. 40, no. 1, pp. 16–28, Jan. 2014. [Online]. Available: http://www.sciencedirect.com/science/article/pii/S0045790613003066

[168] E. Borgonovo and E. Plischke, "Sensitivity analysis: a review of recent advances," *European Journal of Operational Research*, vol. 248, no. 3, pp. 869–887, 2016.

[169] R. Bellman, "Dynamic programming," *Science*, vol. 153, no. 3731, pp. 34–37, 1966.

[170] G. C. Cawley and N. L. Talbot, "On over-fitting in model selection and subsequent selection bias in performance evaluation," *The Journal of Machine Learning Research*, vol. 11, pp. 2079–2107, 2010.

[171] L. L. Gratiet, S. Marelli, and B. Sudret, "Metamodel-based sensitivity analysis: polynomial chaos expansions and gaussian processes," *arXiv preprint arXiv:1606.04273*, 2016.

[172] P. Jylänki, J. Vanhatalo, and A. Vehtari, "Robust gaussian process regression with a student-t likelihood." *Journal of Machine Learning Research*, vol. 12, no. 11, 2011.

[173] R. Genuer, J.-M. Poggi, and C. Tuleau-Malot, "Variable selection using random forests," *Pattern recognition letters*, vol. 31, no. 14, pp. 2225–2236, 2010.

[174] J. Herman and W. Usher, "Salib: an open-source python library for sensitivity analysis," *Journal of Open Source Software*, vol. 2, no. 9, p. 97, 2017.

[175] S. Tarantola, D. Gatelli, S. Kucherenko, W. Mauntz *et al.*, "Estimating the approximation error when fixing unessential factors in global sensitivity analysis," *Reliability Engineering & System Safety*, vol. 92, no. 7, pp. 957–960, 2007.

[176] B. Shahriari, K. Swersky, Z. Wang, R. P. Adams, and N. De Freitas, "Taking the human out of the loop: A review of bayesian optimization," *Proceedings of the IEEE*, vol. 104, no. 1, pp. 148–175, 2015.

[177] R. B. Gramacy and H. K. H. Lee, "Bayesian treed gaussian process models with an application to computer modeling," *Journal of the American Statistical Association*, vol. 103, no. 483, pp. 1119–1130, 2008.

[178] G. Chastaing, F. Gamboa, and C. Prieur, "Generalized sobol sensitivity indices for dependent variables: numerical methods," *Journal of Statistical Computation and Simulation*, vol. 85, no. 7, pp. 1306–1333, 2015.

[179] G. Li, H. Rabitz, P. E. Yelvington, O. O. Oluwole, F. Bacon, C. E. Kolb, and J. Schoendorf, "Global sensitivity analysis for systems with independent and/or correlated inputs," *The journal of physical chemistry A*, vol. 114, no. 19, pp. 6022–6032, 2010.

[180] E. ASTM, "691-99. standard practice for conducting an interlaboratory study to determine the precision of a test method," *Annu. Book of ASTM Stand*, vol. 14, pp. 203–224, 2003.

[181] K. Kersting, C. Plagemann, P. Pfaff, and W. Burgard, "Most likely heteroscedastic gaussian process regression," in *Proceedings of the 24th international conference on Machine learning*, 2007, pp. 393–400.

[182] B. D. Tracey and D. Wolpert, "Upgrading from Gaussian processes to Studentst processes," in *2018 AIAA Non-Deterministic Approaches Conference*, 2018, p. 1659.

[183] A. Hebbal, L. Brevault, M. Balesdent, E.-G. Talbi, and N. Melab, "Bayesian optimization using deep gaussian processes with applications to aerospace system design," *Optimization and Engineering*, pp. 1–41, 2020.

[184] R. Kumar, C. Carroll, A. Hartikainen, and O. A. Martin, "ArviZ a unified library for exploratory analysis of Bayesian models in Python," *The Journal of Open Source Software*, 2019. [Online]. Available: http://joss.theoj.org/papers/10.21105/joss.01143

[185] A. Vehtari, A. Gelman, D. Simpson, B. Carpenter, P.-C. Bürkner *et al.*, "Rank-normalization, folding, and localization: An improved rhat for assessing convergence of mcmc," *Bayesian Analysis*, 2020.

APPENDICES

Appendix A

Data for Bulk Estimation

A.1 Non-Local Mean Filter Settings

The μCT scans are filtered using a non-local mean filter. The settings are determined through visual inspection.

Table A.1: Unimodal Filter Settings

Parameter	Value
patch size	15
patch distance	25
h	σ_{est}

Table A.2: Bimodal Filter Settings

Parameter	Value
patch size	5
patch distance	10
h	$3\sigma_{\text{est}}$

A.2 Diagnostic Plot Explanation

A.2.1 Trace Plots

Figure A.1, A.3 and A.5 are the trace plot of the inference. Reiterating from Chapter 3, the model fitted is the following:

$$
\begin{aligned}
\{\mu_i \sim Uniform(20.0, 60.0) : i = \{\text{Unimodal}, \text{Bimodal}\}\} \\
\text{Part}_{j(i)} \sim N(0, \sigma_{\text{part}}) \\
\mu = \mu_i + \text{Part}_{j(i)} \\
y_{ijk} \sim N(\mu, \sigma_{\text{gage}}) \\
\\
\sigma_{\text{part}} \sim HalfCauchy(25) \\
\sigma_{\text{gage}} \sim HalfCauchy(25)
\end{aligned}
$$

The sampler is exploring the probability space by sampling different values of the model input parameters $(\mu_i, \sigma_{\text{part}}, \sigma_{\text{gage}})$. The left graph shows the probability density of the sampled values. The right graph shows the sampled with respect to sample number. The left graph is computed by summing up the right graph. When the left graph looks skewed towards zero or the right graph does not resemble a thick caterpillar, this indicates a biased sampling and a lack of convergence.

A.2.2 Predictive Posterior Check Plots

Predictive posterior plot overlays data generated by the model's posterior over the real data. This is useful to check the fitness of the model.

A.2.3 Convergence Metrics Explanation

The following convergence metrics are implemented in Arviz[184] following the work of Vehtari et al.[185].

A.2.4 Split-$\hat{R}$

In the Markov-Chain Monte Carlo (MCMC) sampler, the sampling is done simultaneously in multiple processes (chain). The rank normalized $\hat{R}$ checks for convergence by comparing the variance between chain with the variance within chain. If convergence has been achieved then the variance should be the same ($\hat{R} = 1$)[185]. Vehtari et al. recommends a $\hat{R} < 1.01$ [185].

A.2.5 Effective Sample Size (ESS)

In MCMC sampling, autocorrelation within the chain increases uncertainty on the estimated parameters. ESS measures the number of Indepependent samples. When computing the ESS, the samples are assumed to be generated from a Normal distribution. When this is not true, Vehtari et al. proposes to use ESS_{bulk} instead. Low ESS_{bulk} might indicate issue with trends and locations of the chain. In addition, ESS_{tail} measures sampling efficiency in the distribution's tail. This is useful for casting doubt on the estimated the confidence interval for the parameters when the ESS_{tail} is low. Vehtari et al. recommends a value of at least 400 for all ESS's[185].

A.2.6 Markov-Chain Monte-Carlo Error (MCSE)

MCSE is the uncertainty of the estimated parameters. The lower the number the higher the chances the estimated parameter is close to the true value.

A.3 Chapter 3 Data

Table A.3: Measured Density using ISO 5013

Batch	ID	Operator	Powder	Mean Density	Std Density
3	28	2	Unimodal	55.011208	0.165669
	0	1	Unimodal	53.827055	0.059158
	1	1	Unimodal	55.167928	0.073824
4	2	1	Unimodal	55.14971	0.048116
	25	2	Unimodal	55.674153	0.174335
	26	2	Unimodal	55.031899	0.064891

5	11	1	Unimodal	54.654989	0.483203
	12	1	Unimodal	56.692097	0.054868
	13	1	Unimodal	54.739879	0.238032
	14	1	Unimodal	55.871378	0.139761
6	3	1	Bimodal	58.263677	0.243462
	4	1	Bimodal	56.187039	0.069024
	5	1	Bimodal	56.681804	0.039564
	6	1	Bimodal	55.981498	0.053363
	19	2	Bimodal	55.53081	0.354884
	20	2	Bimodal	55.352084	0.28207
7	7	1	Bimodal	56.906479	0.085766
	8	1	Bimodal	56.612079	0.038528
	9	1	Bimodal	58.41894	0.411705
	10	1	Bimodal	56.302846	0.079516
	16	2	Bimodal	55.704617	0.287154
	21	2	Bimodal	57.190429	0.285024
8	15	2	Bimodal	59.805367	0.18024
	17	2	Bimodal	59.456702	0.182413
	18	2	Bimodal	59.879163	0.31375
	22	2	Bimodal	60.100983	0.33804
9	23	2	Unimodal	55.955599	0.108977
	24	2	Unimodal	55.340042	0.261668
	27	2	Unimodal	56.778332	0.15155
	29	2	Unimodal	54.622332	0.307935

Table A.4: Convergence Statistics : ISO 5013, Refer to section A.2.3 for description

	mean	Std	$\text{hdi}_{3}\%$	$\text{hdi}_{97}\%$	$\overline{\text{mcse}}$	mcse Std	$\overline{\text{ess}}$	ess	ess_{bulk}	ess_{tail}	$\hat{R}$
Unimodal	56.906	0.354	56.253	57.56	0.007	0.005	2813	2813	2793	4714	1
Bimodal	54.833	0.383	54.102	55.54	0.008	0.005	2471	2471	2469	3382	1
σ_{gage}	0.358	0.01	0.34	0.377	0	0	8830	8801	8888	10270	1
σ_{part}	1.391	0.197	1.034	1.755	0.004	0.003	2957	2957	2929	6130	1

Table A.5: Measured Density using ASTM B962

Batch	ID	Operator	Powder	Mean Density	Std Density
1	2	1	Unimodal	53.455628	-

	3	1	Unimodal	54.662471	-
2	0	1	Bimodal	55.568668	-
	1	1	Bimodal	56.773419	-
3	30	2	Unimodal	53.883042	0.18208
	4	1	Unimodal	50.045557	0.090183
	5	1	Unimodal	51.583426	0.184077
4	6	1	Unimodal	53.589074	0.11628
	7	1	Unimodal	52.139234	0.226588
	31	2	Unimodal	52.658198	0.097138
	16	1	Unimodal	51.958652	0.490336
	17	1	Unimodal	50.412136	0.369983
5	18	1	Unimodal	52.480039	0.318092
	19	1	Unimodal	52.885678	0.409901
	33	2	Unimodal	54.054584	0.28498
	8	1	Bimodal	52.493028	0.924092
	9	1	Bimodal	52.619978	0.649974
6	10	1	Bimodal	53.449106	0.279074
	11	1	Bimodal	52.678324	0.388559
	27	2	Bimodal	52.184584	0.675857
	12	1	Bimodal	52.641411	0.59541
	13	1	Bimodal	52.975377	0.294588
7	14	1	Bimodal	53.761767	0.275981
	15	1	Bimodal	53.073547	0.295431
	22	2	Bimodal	52.645685	0.141391
	23	2	Bimodal	53.82251	0.126412
	20	2	Bimodal	55.800858	0.036293
	21	2	Bimodal	56.061248	0.583447
8	24	2	Bimodal	56.669936	0.066575
	25	2	Bimodal	57.62076	0.087891
	26	2	Bimodal	56.443724	0.199621
	28	2	Unimodal	51.585446	0.251235
9	29	2	Unimodal	47.707049	0.27542
	32	2	Unimodal	53.607892	0.657432
	34	2	Unimodal	51.894833	0.319916

Table A.7: Measured Density using ASTM D7263

Batch	ID	Operator	Powder	Mean Density	Std Density

1	2	1	Unimodal	52.792076	-
	3	1	Unimodal	55.23096	-
2	0	1	Bimodal	57.703343	-
	1	1	Bimodal	56.638087	-
4	4	1	Unimodal	51.924197	0.121109
	5	1	Unimodal	55.396163	-
	6	1	Unimodal	53.450062	0.034187
5	29	2	Unimodal	52.739129	1.373794
	14	1	Unimodal	51.741833	0.104926
	15	1	Unimodal	53.341855	0.054066
	16	1	Unimodal	53.664002	0.015327
	17	1	Unimodal	51.544274	0.040061
	26	2	Unimodal	53.341933	0.016439
6	7	1	Bimodal	54.530356	0.081478
	8	1	Bimodal	53.355536	0.054531
	9	1	Bimodal	54.741591	0.079161
	10	1	Bimodal	53.806457	0.124711
	19	2	Bimodal	57.059507	5.033294
7	11	1	Bimodal	54.696219	0.045926
	12	1	Bimodal	54.243095	0.105423
	13	1	Bimodal	54.445849	0.136052
	18	2	Bimodal	57.784923	0.125423
	20	2	Bimodal	56.474143	0.066693
8	21	2	Bimodal	67.380977	6.89794
	22	2	Bimodal	57.727976	1.10421
	23	2	Bimodal	61.740171	3.983855
	24	2	Bimodal	61.106357	3.45957
	25	2	Bimodal	58.120651	0.030914
9	27	2	Unimodal	55.207495	0.085111
	28	2	Unimodal	52.485212	0.035729
	30	2	Unimodal	54.354246	0.018499

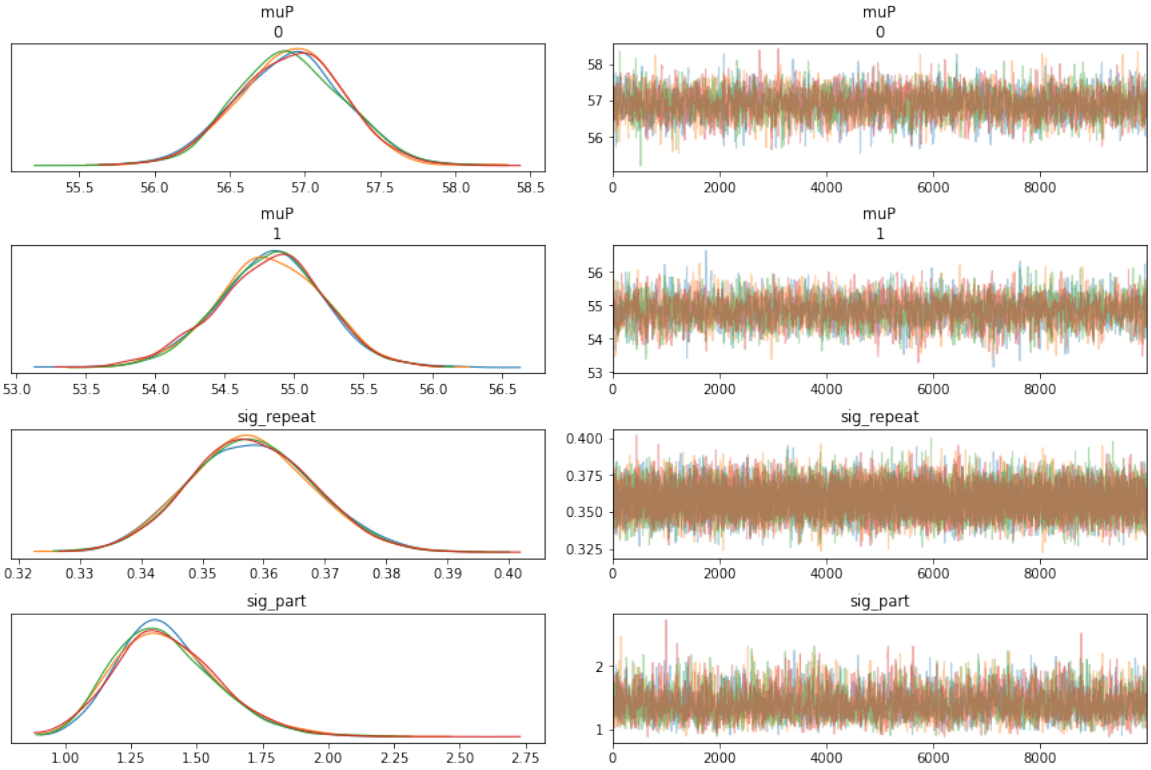

Figure A.1: Bayesian Inference Diagnostic Trace Plot:ISO 5013, Refer to section A.2.1 for description

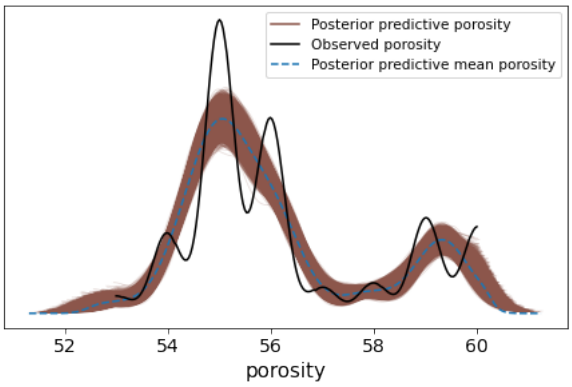

Figure A.2: Predictive Posterior Plot : ISO 5013, Refer to section A.2.2 for description

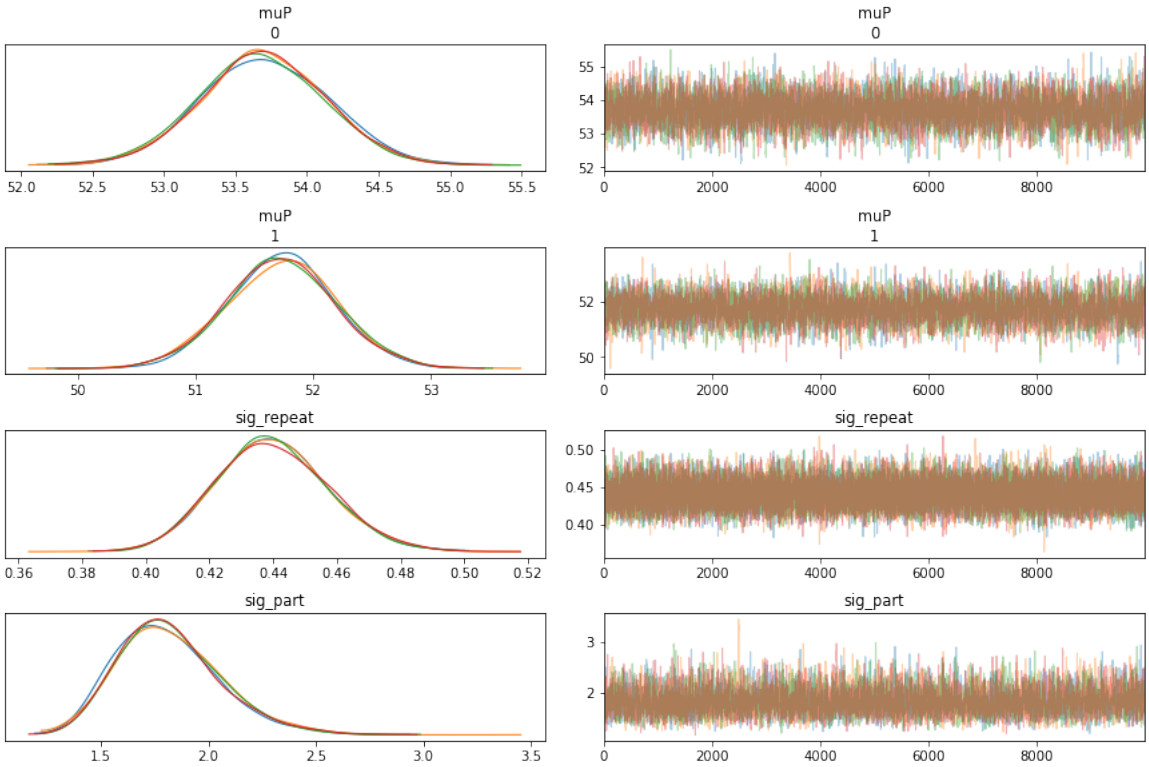

Figure A.3: Bayesian Inference Diagnostic Trace Plot:ASTM B962, Refer to section A.2.1 for description

Table A.6: Convergence Statistics : ASTM B962, Refer to section A.2.3 for description

	mean	Std	$\text{hdi}_3\%$	$\text{hdi}_{97}\%$	$\overline{\text{mcse}}$	mcse Std	$\overline{\text{ess}}$	ess	ess_{bulk}	ess_{tail}	$\hat{R}$
Unimodal	53.696	0.434	52.907	54.537	0.006	0.004	5097	5095	5093	7071	1
Bimodal	51.732	0.455	50.849	52.572	0.006	0.005	4931	4931	4915	7264	1
σ_{gage}	0.44	0.017	0.409	0.473	0	0	16021	15957	16122	17574	1
σ_{part}	1.821	0.238	1.4	2.271	0.004	0.003	4294	4294	4254	8298	1

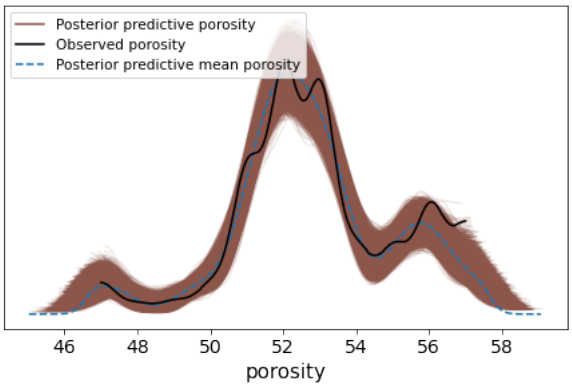

Figure A.4: Predictive Posterior Plot : ASTM B962, Refer to section A.2.2 for description

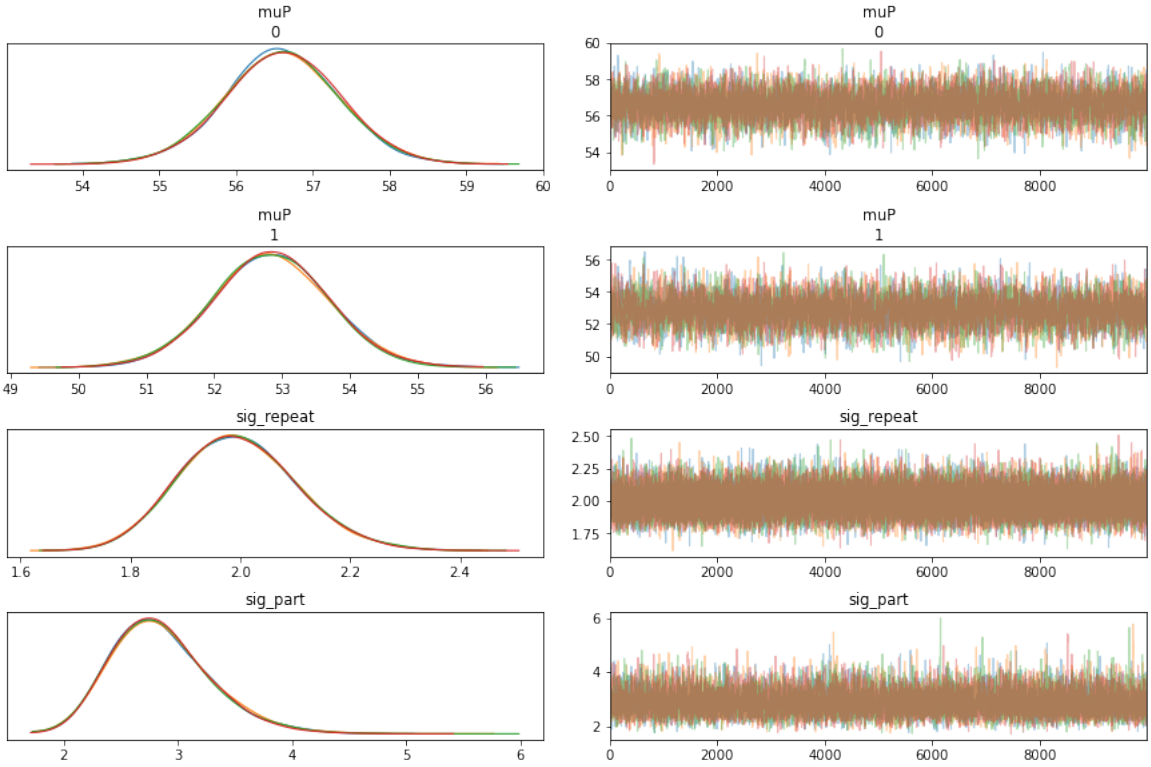

Figure A.5: Bayesian Inference Diagnostic Trace Plot: ASTM D7263, Refer to section A.2.1 for description

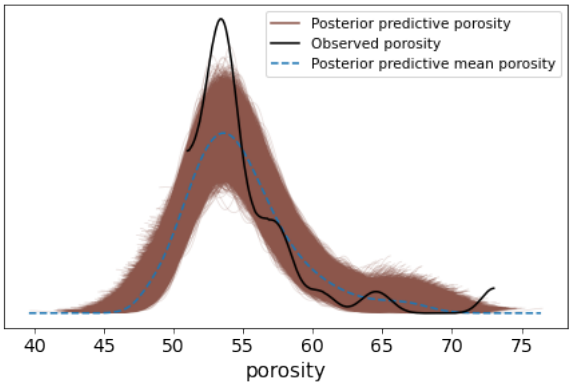

Figure A.6: Predictive Posterior Plot : ASTM D7263, Refer to section A.2.2 for description

Table A.8: Convergence Statistics : ASTM D7263, Refer to section A.2.3 for description

	mean	Std	$\text{hdi}_3\%$	$\text{hdi}_{97}\%$	$\overline{\text{mcse}}$	mcse Std	$\overline{\text{ess}}$	ess	ess_{bulk}	ess_{tail}	$\hat{R}$
Unimodal	56.603	0.738	55.18	57.97	0.011	0.007	4906	4906	4916	8721	1
Bimodal	52.842	0.84	51.275	54.434	0.012	0.009	4766	4766	4758	9310	1
σ_{gage}	1.997	0.106	1.806	2.199	0.001	0	35516	35320	35681	30090	1
σ_{part}	2.862	0.432	2.1	3.675	0.005	0.003	7800	7772	7919	13387	1

Appendix B

Data for Particle detection

B.1 Sampled labeled Data

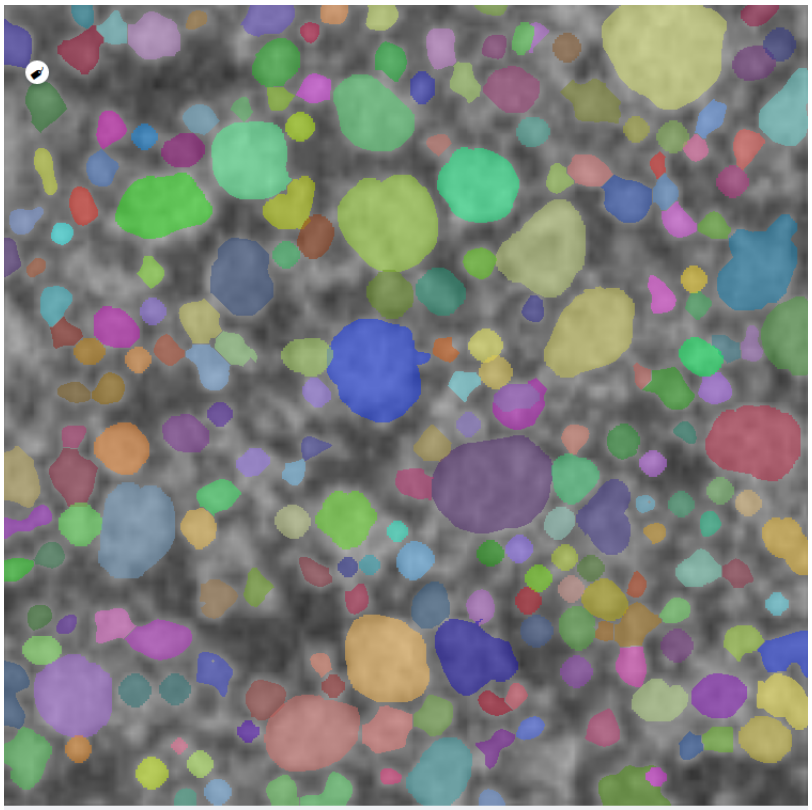

Figure B.1: Sample Labeled Image

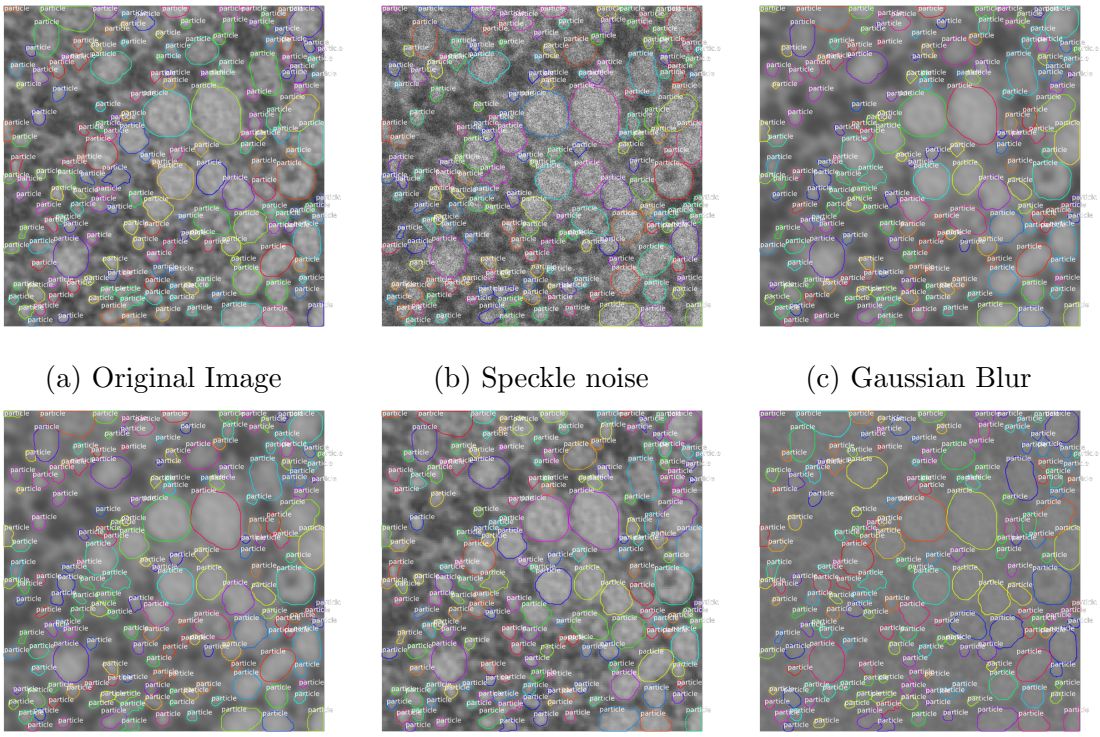

(a) Original Image (b) Speckle noise (c) Gaussian Blur

(d) Gaussian Blur (e) Pixelate (f) Contrast

Figure B.2: Image augmentation example

Appendix C

Data of SS316L Process mapping

C.1 Process Mapping Data

Table C.1: Covariance matrix used in generating the Latin hypercube sample

	1	2	3	4	5	6	7	8	9
Layer thickness (1)	1	0	0	0	0	0	0	0	0
Oscillator (2)	0	1	-0.8	0	0	0	0	0	0
Recoat Speed (3)	0	-0.8	1	0	0	0	0	0	0
Roller Speed (4)	0	0	0	1	-0.8	0	0	0	0
Roller RPM (5)	0	0	0	-0.8	1	0	0	0	0
Drying Time (6)	0	0	0	0	0	1	-0.3	0.4	0
Drying Power (7)	0	0	0	0	0	-0.3	1	0.6	0
Saturation level (8)	0	0	0	0	0	0.4	0.6	1	0.5
binder set time (9)	0	0	0	0	0	0	0	0.5	1

C.2 Sobol Indices Explanation [2, 3]

Given a function a $f : \Omega \to \mathbb{R}, \Omega \subset \mathbb{R}^p$ and input $x = \{x_1, ..., x_p\} \in \Omega$. Assuming the input x are independent and $f(x)$ is square integrable. With $u = \{i_1, i_2, ..., i_k\} \subset \{1, 2, ..., p\}$, let x_u denote the subset of the variable input x ($x_u \subset x$). x is defined within the unit interval

Table C.2: Mean and Standard deviation of Porosity (%)

batch	mean	std
1	38.14	0.90
2	37.91	1.93
3	39.31	2.04
4	41.35	1.86
5	38.11	1.72
6	41.29	1.51
7	44.49	1.21
8	N/A	N/A
9	38.13	0.66
10	39.31	0.92
11	39.30	2.12
12	37.51	0.79

$I^p = [0,1]^p$. I^p is the p-dimensional hypercube,. The analysis of variance decomposition is the following:

$$f(x) = f_0 + \sum_{i=1}^{p} f_i(x_i) + \sum_{i=1}^{p} \sum_{j=i+1}^{p} f_{ij}(x_i, x_j) + ... + f_{1,2,...,p}(x) \tag{C.1}$$

$$= f_0 + \sum_{i}^{p} \sum_{|u|=i} f_u(x_u) \tag{C.2}$$

If x are independent, the following is true:

$$\int_0^1 f_u(x_u) dx_k = 0 \quad k \in u \tag{C.3}$$

Table C.3: Nominal dimension deviation (mm)

batch	x		y		z	
	mean	std	mean	std	mean	std
1	0.72	0.15	0.56	0.11	0.44	0.05
2	2.28	1.74	1.22	0.25	0.96	0.30
3	2.01	2.07	1.09	0.43	0.71	0.36
4	1.09	0.87	0.77	0.15	1.12	0.17
5	0.76	0.25	0.68	0.08	0.62	0.33
6	1.04	0.46	0.66	0.13	0.53	0.09
7	2.35	1.43	1.67	0.77	1.36	0.78
8	12.12	6.77	1.84	0.43	5.18	0.94
9	1.29	0.59	0.97	0.26	0.76	0.18
10	0.76	0.14	0.70	0.10	0.66	0.07
11	1.95	0.34	2.13	0.53	1.18	0.10
12	2.33	0.84	1.86	0.39	0.95	0.39

Therefore the element of eq. C.2 can be expressed in forms of integral as follow:

$$
\begin{aligned}
f_0 &= \int_0^1 f(x)dx \\
f_i(x_i) &= \int_0^1 f(x) \prod_{k\neq i} dx_k - f_0 \\
f_{ij}(x_i, x_j) &= \int_0^1 f(x) \prod_{k\neq i,j} dx_k - f_0 - f_i(x_i) - f_j(x_j) \\
&\vdots \\
f_u(x_u) &= \int_0^1 f(x) \prod_{k\neq v} dx_k - \sum_{v\in p, v\subset u} f_v(x_v)
\end{aligned}
$$

By taking the variance on both side of equation C.2:

$$
\mathrm{Var}(f(x)) = \sum_{i=1}^{p} \mathrm{Var}(f_i(x_i)) + \sum_{i=1}^{p} \sum_{j=i+1}^{p} \mathrm{Var}(f_{ij}(x_i, x_j)) + ... + \mathrm{Var}(f_{1,2,...,p}(x)) \tag{C.4}
$$

Therefore, the first order sobol sensitivity of variable x_u is :

Table C.4: Print duration (min)

batch	duration(min)
1	92
2	101
3	115
4	78
5	74
6	56
7	46
8	94
9	101
10	54
11	108
12	87

Table C.5: Possible future trial, column title shown in table C.1

Run	1	2	3	4	5	6	7	8	9
1	204.18	1860.42	82.54	3.8	164.15	13.59	71.31	86.94	7.85
2	211.98	1847.1	84.39	2.9	165.1	13.29	72.14	87.12	7.83
3	188.47	1877.31	79.98	3.42	162.44	13.68	71.4	87.32	7.84
4	217.12	1847.34	84.3	6	161.2	13.54	71.32	86.83	7.86
5	200.82	1836.94	87.37	4.1	174.99	13.97	70.91	86.49	7.71

$$S_u = \frac{\mathrm{Var}(f_u(x_u))}{\mathrm{Var}(f(x))} \tag{C.5}$$

S_u can be interpreted as the variance contribution of x_u to $f(x)$. The total Sobol index (T_u) is the summation of all variance involving the factor u.

$$T_u = \sum_{k \in u} S_k \tag{C.6}$$

All first order Sobol index add up to 1. In addition, S_u is smaller than T_u.

Table C.6: Possible future trial lower bound prediction

Run	Porosity	Time	X dev	Y dev	Z dev
1	34.15	70.4	6.91	1.03	4.25
2	34.15	66.14	6.25	0.91	3.84
3	34.15	66.32	5.56	0.88	3.44
4	34.23	56.66	4.28	0.71	2.87
5	34.16	66.15	5.7	0.82	3.5